Real-time Monitoring and Intra-procedure Analysis of Thermal Ablation Using Contrast-Enhanced Computed Tomography

By

Po-hung Wu

A dissertation submitted in partial fulfillment of

The requirements for the degree of

Doctor of Philosophy

(Electrical and Computer Engineering)

at the

UNIVERSITY OF WISCONSIN-MADISON

2017

Date of final oral examination: 5/26/2017

The dissertation is approved by the following members of the Final Oral Committee:

Dr. Christopher L. Brace, Associate Professor, Biomedical Engineering

Dr. Tomy Varghese, Professor, Medical Physics

Dr. Walter F. Block, Professor, Biomedical Engineering

Dr. Paul Laeseke, Assistant Professor, Radiology

Dr. Yu Hen Hu, Professor, Electrical and Computer Engineering

To my beloved parents

Acknowledgements

I would like to express my sincere appreciation to my advisor Dr. Christopher L Brace for his full support, helpful advice and encouragement throughout my PhD study and research. I would like to thank him for his expert guidance and invaluable suggestions on experimental design, data processing, conference presentation, scientific paper drafting and dissertation preparation during the past six years. Besides this, Dr. Brace also provided helpful advice when I met some difficulties or frustration during my PhD studies and research. To me, he is not only a research advisor but also a mentor that helped me become a good independent researcher. I will bring what I learned in his lab to the next stage in my academic career.

I would also like to express my appreciation to Dr. Yu Hen Hu, Dr. Tomy Varghese, Dr. Paul Laeseke and Dr. Walter Block for having served as my committee members and their brilliant suggestions and comments on my PhD work. In addition, I would like to express my special thanks to Jim White and Mariajose Bedoya, who are members in our lab. Without their help in data collection, analysis and interpretation, I could not have completed my research.

Contents

List of Figures

List of Tables

Abstract

Thermal ablation is widely used to treat tumors throughout the body. An ablation procedure involves placing a thin applicator percutaneously into the targeted region to destroy malignant tissue by generating cytotoxic temperature changes around the applicator. Imaging feedback is necessary to guide applicator placement to monitor ablation zone growth and to evaluate treatment response. Despite post-ablation imaging is most commonly used in ablation evaluation and has some good performance, the lack of intra-procedural feedback prevents practitioners from correcting treatment parameters or identifying potential complications early. Contrast-Enhanced Computed Tomography (CECT) is widely adopted in post-ablation image to display the ablation zone since iodinated contrast material can brighten normal perfused background to make less perfused ablation zone more distinguishable. With short acquisition time, CECT will be useful in real-time ablation monitoring.

In this study, the feasibility of CECT was examined via image analysis technique. The solution of dose challenge via periodic CECT scan and the technique of automated segmentation of ablation zone was developed. Finally, the model to describe temporally increasing rate along with radius and vertical direction was developed. To better estimate the actual ablation volume, tissue contraction was measured using CT imaging on both RF and microwave ablation. The mechanism of ablation induced tissue shrinkage was studied, and the contraction model dependent on temperature and heating time was developed.

This study will contribute to providing a technique to evaluate and study thermal ablation during procedure. Physicians could utilize this technique to assist them in efficacy evaluation of

thermal ablation, and researchers could use this technique to understand the biomechanisms of thermal ablation, which is beneficial to improve the techniques. The outline of the dissertation is as follows:

Chapter 1 reviews background of thermal ablation, analyzes why and how thermal ablation is used for cancer treatment and then gives a brief introduction of current thermal ablation techniques including RF ablation and microwave ablation. This chapter finally describes why imaging is needed for thermal ablation procedure.

Chapter 2 outlines and briefly introduces common medical imaging modalities used for ablation monitoring and assessment including ultrasound, MRI and CT. This chapter finally describes the challenge of each medical imaging modalities using in real-time, intra-procedural ablation monitoring.

Chapter 3 describes iodinated contrast material behavior during ablation procedure and investigates its influence on visualization of ablation zone. Several image analysis techniques were used in analyzing contrast agent behavior and statistical analysis such as contrast-to- noise ratio was used to quantify the visibility of ablation zone on image.

Chapter 4 describes a method to enhance visualization of ablation zone from serial, low-dose CECT scanning. Several image processing techniques were used in visualization enhancement, and the statistical and post-ablation analysis (eg. similarity measurement, dimension variability analysis, measurement correlation etc.) were used to compare the unprocessed and processed CECT images.

Chapter 5 describes a method to automatically segment ablation volume from both low-dose CT and CECT. Our method includes texture features extraction and unsupervised clustering

techniques, and the statistical analysis and ablation analysis were used to compare the performance of the proposed segmentation method to manual segmentation.

Chapter 6 describes a method to model the temporal dimension growth during ablation procedure. Spherical harmonic, which is widely used in shape description, was used in extracting the growth ratio of ablation dimension. Predicted ablation volume generated from out model ill compare with observed data to examine the validation.

Chapter 7 summaries the contribution of the present works and lists several future studies extended from current research for improving ablation monitoring and modeling temporal growth of ablation volume.

Chapter 1 Introduction of Thermal Ablation and the Role of Imaging

The introduction chapter is divided into three sections. The first section will provide background information of current cancer status around the world, including a particular section for liver cancer due to increasing incidence and high mortality rate. The second part will explain why thermal ablation is used for cancer treatment and review the common types of thermal ablation techniques: RF, microwave and other techniques. The last part will describe the role of imaging in thermal ablation therapy.

1.1 Current Status of Cancer

1.1.1 Global cancer facts

Cancer is one of the leading causes of death worldwide. In most cancers (except leukemia, in which abnormal cells divide in the blood stream and then influence normal blood function), the abnormal cells proliferate uncontrollably and invade or spread to other parts of the body. These growing cells form lumps or masses of tissue called tumors. When tumors grow and diffuse without regulation, the surrounding healthy tissue can be destroyed and lose the ability to function normally. Such local effects have a negative influence on body function, for example inhibiting the digestive or nervous systems. In addition, some cancer cells can separate from the index tumor and diffuse through the blood or lymphatic system to form a new tumor distant from the original tumor. This characteristic generates unpredictability in cancer progression and increases the lethality of the disease.

Currently, cancer is the second-leading cause of death in the U.S., with an estimated 600,920 deaths annually [1]. Worldwide, cancer is also a leading cause of death with approximately 14 million new cases and 8.8 million deaths annually [2]. According to a report from the World Health Organization (WHO), the most common causes of cancer death in 2015 were: lung (1.69 million deaths), liver (788,000 deaths), colorectal (774,000 deaths), stomach

(754,000 deaths) and breast (571,000 deaths). The leading types of cancer are also different between males and females. In 2012, men were most affected by cancers of the lung and trachea (1.24 million), prostate (1.1 million), and colon and rectum (0.75 million) while women were most affected by cancers of the breast (1.7 million), colon and rectum (0.61 million), and lung, bronchus and trachea (0.58 million) [3].

Besides gender difference, there is also geographic variation on number of cancer worldwide. According to the WHO, areas with greater development such as Northern America or Europe have a higher rate of cancer incidence **(Figure 1.1)** [3]. However, the number of new cancers has also increased rapidly in less developed countries. Based on these statistics, the number of new cancer cases and cancer deaths in less developed countries accounted for 57% of cancer cases and 65% of cancer deaths worldwide [3], which indicated that the cancer burden has already shifted to those less developed countries. The leading types of cancer were slightly different with respect to the economic development of countries. Although breast cancer was the most common type of cancer for females in both developed and developing countries (793,700 for developed countries and 882,900 for developing countries), the most common type of cancers for males in developed and developing countries were prostate and lung, respectively. In developed countries, colorectal cancers were the second and third leading cause of cancer deaths for males and females, respectively. In contrast, liver and stomach were ranked in the top three common types of cancers for male, and cervix uteri was ranked in third leading cause of cancer deaths for female in developing countries. It is generally considered that age of the population, the usage of tobacco and viral infections are the major reasons for the observed geographic differences.

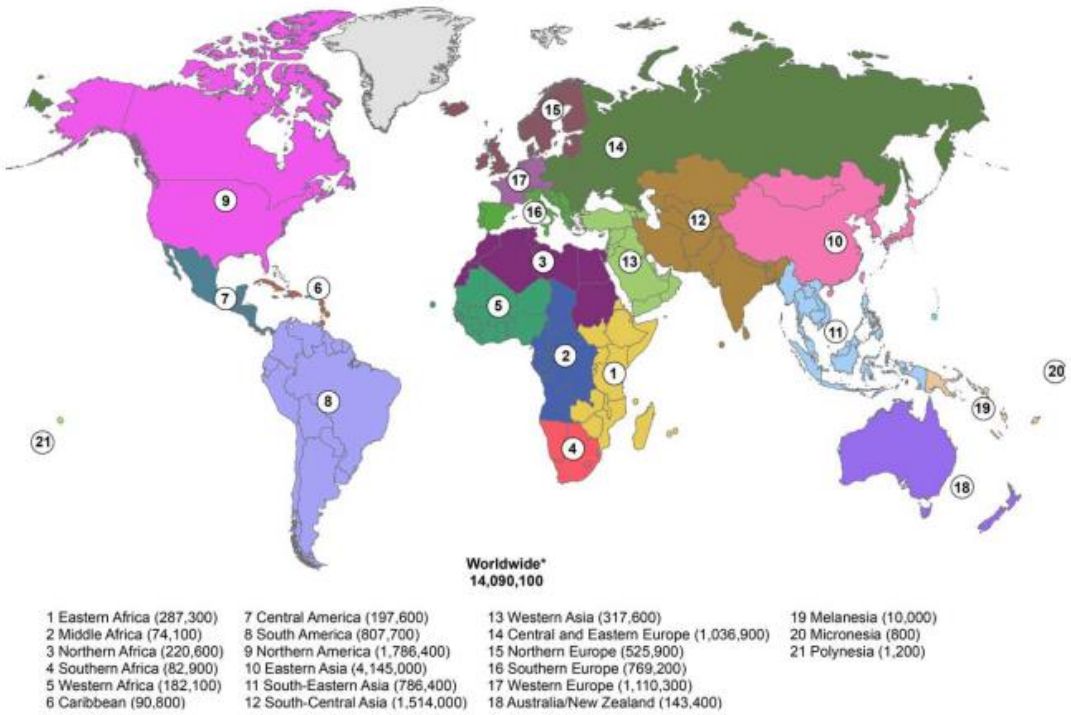

Figure 1.1 Estimated number of New Cancer Cases in 21 World Areas [3]

There are many possible causes of cancers, and it is hard to determine which one is most significant. Currently, most researchers consider that the occurrence of cancers are highly related to environmental factors and lifestyle or behavior including four common causes: tobacco, obesity, infection and radiation [4].

Tobacco smoking is highly related to many kinds of cancers especially lung cancer (accounting for 80% of new cases) since it has about 50 known carcinogens such as nitrosamines and polycyclic aromatic hydrocarbons [5], [6]. As a result, the risk of dying from lung cancer is much higher for smokers than non-smokers [7]; Obesity is now believed to be a major factor increasing the risk of many cancers. Excess fat in the human body will have negative impacts on immune system function and levels of specific hormones that can increase the risk of getting cancer. Infectious diseases account for 18% of cancer death around the world [8]. Oncoviruses, which mean the

viruses causing cancer, induce little or even no disease after infection and then eventually develop to cancer without proper treatment. For example, 1 in 200 people infected with hepatitis B and 1 in 45 people infected with hepatitis C develop liver cancer each year. Excessive radiation exposure can damage DNA and induce irreversible changes in cell proliferation. Currently, up to 10% of invasive cancer are related to radiation exposure [8].

1.1.2 Liver cancer

Among all kinds of cancer, liver cancer is the second leading killer worldwide, and is one of the few cancers that are demonstrating an increase in incidence. In general, liver cancer is more common in males than in females, and in less developed countries than in more developed countries. Liver cancer rates are highest in East and South Asia and Northern and Western Africa. In those areas, males have a liver cancer rate two to three times greater than females **(Figure 1.2)** [3]**.** Among 782,500 new liver cancer cases and 745,500 deaths worldwide, China accounted for almost 50% of total cases and deaths [3].

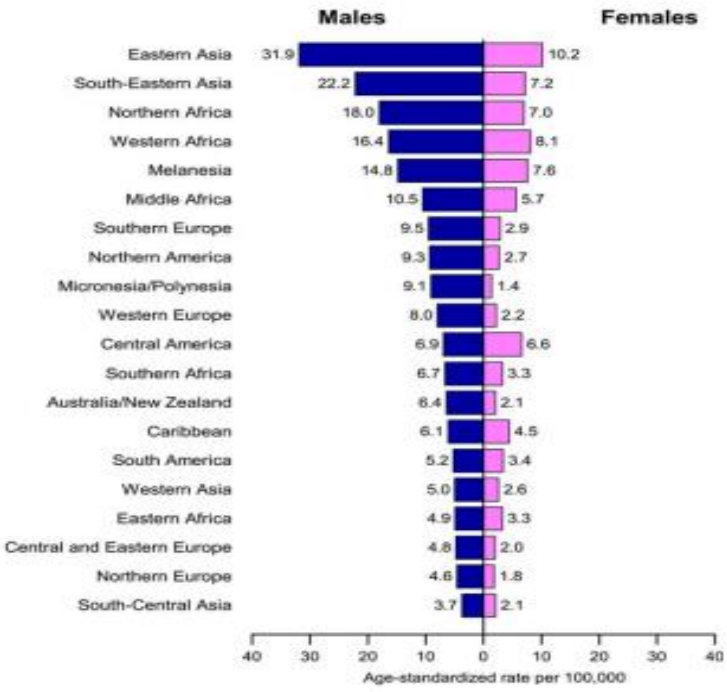

Figure 1.2 Liver Cancer Incidence Rate by Sex and World Area [3]

The most primary liver cancer occurring worldwide is hepatocellular carcinoma (HCC), which accounts for 70% to 90% of liver cancer cases [9]. While the incidence of HCC is generally higher in less developed areas, especially in parts of Asia and sub-Sharan Africa due to higher infection of chronic hepatitis B virus (HBV), the incidence rate is increasing in more developed areas [10]. For example, the age-adjusted incidence rate of liver cancer increased three times between 1975 and 2011 in the United State due to the increasing rate of the chronic hepatitis C virus (HCV) infection, which was possibly due to injected drug abuse in the 1960s and 1970s, and increasing rates of obesity and diabetes [11], [12]. Currently, hepatocellular carcinoma causes 662,000 deaths around the world – half of them in China. In the United States, experts estimate that about 40,710 new cases of liver cancer will be diagnosed in 2017 – three-fourth of them will be hepatocellular carcinoma [13]. From the statistics above, hepatocellular carcinoma will become more and more common even if we have significant progress on medicines and therapies.

The major causes of HCC are infection of viral hepatitis, cirrhosis and metabolic toxins [14]. Viral hepatitis such as hepatitis B or C is the most significant factor contributing to HCC. However, the mechanism of causing HCC by viral hepatitis infection are not completely known. Both HBV and HCV infection may cause liver inflammation and fibrosis and eventually lead to cirrhosis, which are generally considered as the early sign of HCC [15]–[17]. In some cases, patients with HBV infection could even directly induce HCC without cirrhosis [18]. Individuals infected with HBV or HCV have a 15-20x greater risk of developing HCC compared to non-infected individuals [12], [19]. Currently, HBV and HCV account for 32% of infected-related liver cancer cases in less developed areas, and 19% in more developed areas [3].

Even if not induced by viral infection, cirrhosis itself is an important factor contributing to HCC. The development of cirrhosis will increase the proliferation of fibrous tissue and destroy the mechanism of hepatocyte proliferation, providing a good environment to develop cancerous tissue [20]–[22]. Several studies have indicated that the annual incidence rates of HCC in patients with cirrhosis is still 2-6%, even after excluding chronic HBV or HCV [22]–[24]. Several research groups around the world also demonstrated that the HCC incidence rate for individuals with both alcoholism and cirrhosis was higher than those with alcoholism only [25]–[31].

Some specific metabolic toxins may also mutate the gene or damage healthy liver cells, which increase the risk of HCC incidence. For example, aflatoxin B_1 (AFB_1), which is produced by infested grain or fermented soy beans when stored in high moisture conditions, is classified as a carcinogen by the International Agency for research on Cancer [32]. AFB_1 can cause mutations at serine 249 in the tumor suppressor p53, and then increase the probability of suffering from HCC [19], [33]

Besides HCC, liver tumors may also arise as metastasis or secondary liver cancer [34], [35]. In general, the rich blood supply from both portal and arterial circulation along with fenestrations in the hepatic sinusoidal epithelium may help increase the development of metastatic nodules in the liver [36]. Up 70% of patients with colorectal cancer eventually develop liver metastasis while few cases are caused by breast and lung cancer [37]–[39].

Liver cancer is one of the most lethal cancers worldwide. The average 5-year survival rate is about 18% including all stages. However, patients who are diagnosed within the early stage (less than three tumors, smaller than 3 cm, and preserved liver function) have an average 5-year survival rate of 72% [13]. When cancer cells spread to surrounding tissue or organs, the average survival rate is decreasing to 11%. When the cancer cells have already spread to distant part of human body,

the average 5-year survival rate is only 3%. Therefore, our objective is to screen and identify liver cancers in at-risk populations early, then treat those tumors as soon as possible, to achieve the highest possible efficacy of therapy in each patient.

1.2 Thermal ablation

Traditionally, radiation therapy, surgery, and chemotherapy are the three primary treatments for focal tumors. However, all these treatments have significant shortcomings in the setting of primary liver cancer. Surgery is highly restricted by a patient's physical condition. Patients with liver cirrhosis may have portal hypertension and poor clotting function, which may lead to intraoperative bleeding during surgery [40]–[42]. As a result, only a small percentage of patients (~25%) are eligible for surgery. Chemotherapy efficacy is poor against HCC, and is limited to end-stage disease [43], [44]. Radiation therapy may cause long-term damage in normal liver due to high rate of mitosis happening during hepatocyte regeneration. Because of these major disadvantages, alternative therapies such as thermal ablation are emerging as viable treatment options for liver cancer.

Thermal ablation is most commonly performed using a needlelike device inserted into the targeted region. Once the device is placed, energy (e.g., radiofrequency electrical current or microwaves) is delivered directly to the surrounding tissue. The energy will induce tissue heating sufficient to generate cytotoxic temperature changes [45]–[51]. Compared to traditional cancer treatments, thermal ablation is less invasive with lower procedural cost. Morbidity and mortality for thermal ablation is reduced compared to surgery [52]–[54].

1.2.1 Radiofrequency (RF) ablation

RF ablation is typically adopted as a treatment for cancer when surgery is not possible [45], [51], [55]–[57]. In RF ablation, one or more thin, needle-like electrodes are inserted into the target

region(s). An alternating voltage potential applied to the electrode allows current to flow through the body and return through a dispersive reference electrode ("ground pad") placed on the patient's skin. Ions in solution with tissue water serve as the charge carriers. The ions in the tissue will oscillate in response to the applied alternating current and then produce resistive heating to destroy targeted tissues **(Figure 1.3)** [57].

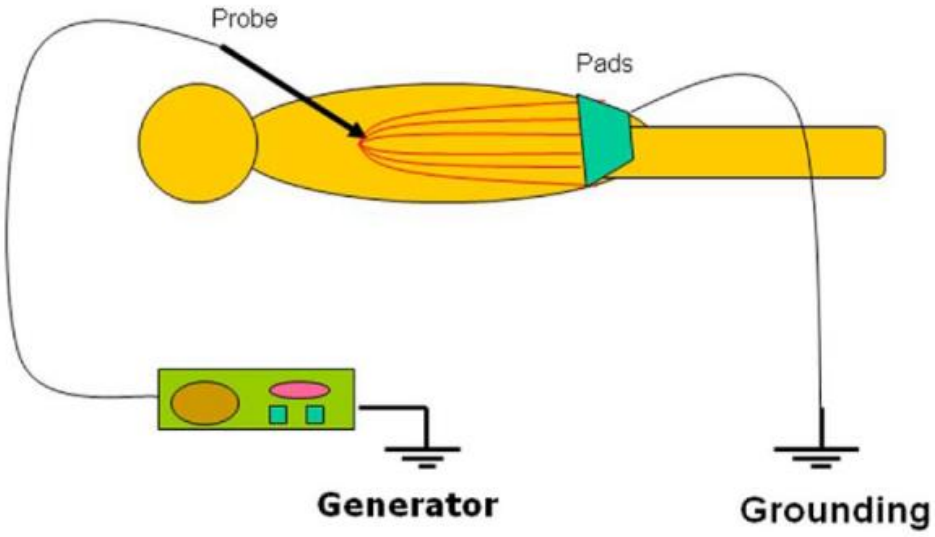

Figure 1.3 The "closed-electrical circuit" for RF ablation [57]

During RF ablation, tissue temperature will increase along with time. Irreversible damage leading to cellular necrosis can occur when temperatures of 42^{o}C to 45^{o}C are maintained for at least 10 minutes [58]. When temperatures exceed 46^{o}C, the time to necrosis decreases to several minutes [59]. When temperatures exceed 60^{o}C, proteins in the tissue are coagulated and the plasma membrane melts so that the cells is destroyed almost instantaneously [60]. Therefore, the goal of RF ablation procedures is to elevate tissue temperatures to at least 60^{o}C.

Despite reported success in treating small tumors, there are two major disadvantages for RF ablation that limit its broader utility for focal tumor ablation [45], [55], [60]. First, ablative

temperatures near 100^{o}C cause dehydration, water vaporization and tissue charring. These effects will progressively increase tissue impedance, which hinders further electrical current delivery **(Figure 1.4)** [51]**.** RF ablation systems work around this problem by either pulsing power to avoid temperatures more than 100°C, or using reduced power and slower heating to delay the onset of water vaporization. The slower heat generation leads to the second major issue for RF ablation: "heat-sink effects". Tissue perfusion and vascular blood flow both tend to disperse thermal energy from the ablation zone. Such blood flow effects decrease ablation zone size and can protect tumor cells adjacent to vascular structures, which both reduce the efficacy of RF ablation.

Several technological enhancements attempt to address these problems [55], [60], [61]. For example, the internal cooling mechanism of some electrodes will limit the temperature of tissue immediately adjacent to the electrode, which will decrease tissue impedance so that the energy will be easier to deposit in the targeted region [62]. Another method is to use expandable, multi-tined, or clustered electrodes which could increase the surface area of electrode to increase power delivery and offset heat-sink effects [63]. Some research groups also try to inject saline to reduce the tissue impedance during RF ablation [64]. However, none of these solutions has been sufficient to prevent local recurrence after RF ablation of tumors larger than about 2-3 cm diameter.

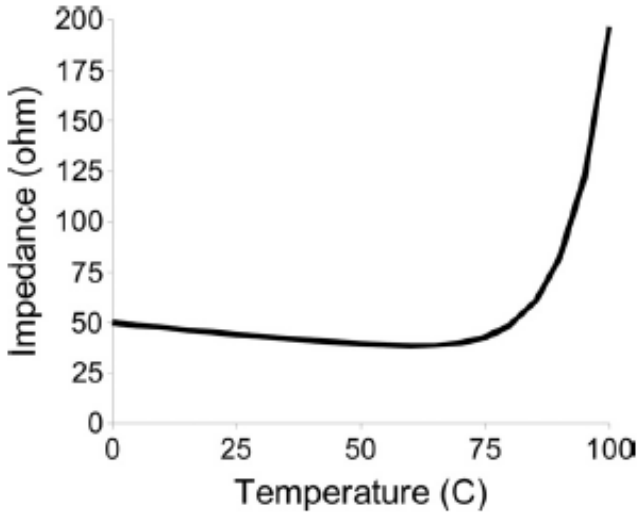

Figure 1.4 Increasing of impedance during RF ablation [51]

1.2.2 Microwave (MW) ablation

Microwave ablation performs a similar function to RF ablation – both techniques attempt to deliver energy into targeted tissue to induce tissue heating and then destroy it. However, the mechanism of heat generation is different. While RF ablation delivers electrical current through tissue, MW ablation "radiates" high frequency electromagnetic energy (typically in the range of 900 MHz and 2.5GHz) through the target tissue via an interstitial antenna. This radiated, high-frequency electromagnetic field (EM) forces polar molecules in tissue (primarily water) to realign with the oscillating EM field, which increases the kinetic energy and, hence, temperature of the target tissue **(Figure 1.5)** [46], [51], [65], [66].

MW ablation has several advantages over RF ablation. First, microwave energy can penetrate through all biological materials, including those with low electrical conductivity and high impedance, such as lung, bone and charred or desiccated tissues [61], [65], [67]. Therefore, the microwave energy can be applied continuously at a high power, which can provide much higher temperatures, faster heating, larger ablation volumes and shorter treatments compared to RF ablation **(Figure 1.6) [51]**. Moreover, the faster heating offered by microwaves can help overcome the "heat-sink" effects of local blood flow [65]. Second, microwave ablation generates heating in a volume around the antenna, which means that multiple antennas can be used simultaneously to treat large tumors, or in separate locations to treat multiple tumors [51]. Finally, microwave ablation does not need ground pads to create a closed-electrical circuit, which is beneficial to eliminate the associated skin burns and procedural complexities during RF ablation [66].

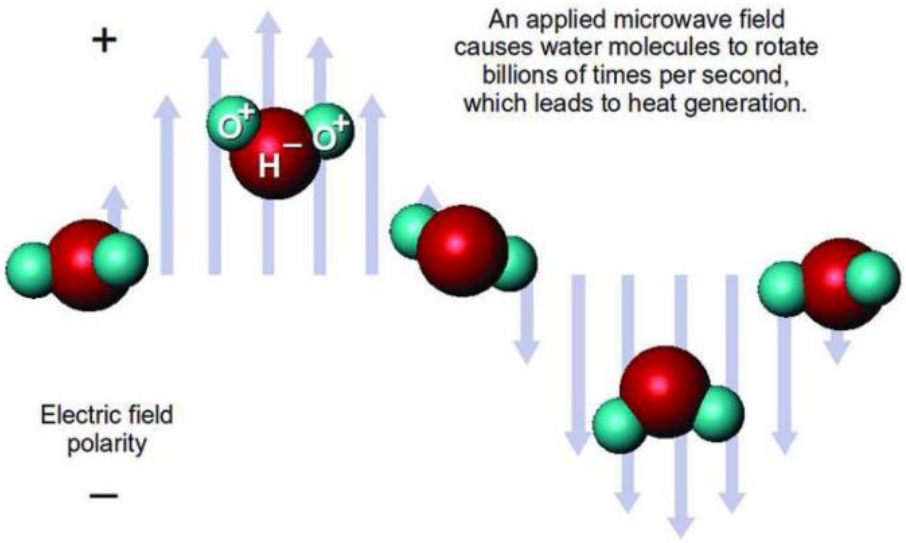

Figure 1.5 The physics of microwave heating [65]

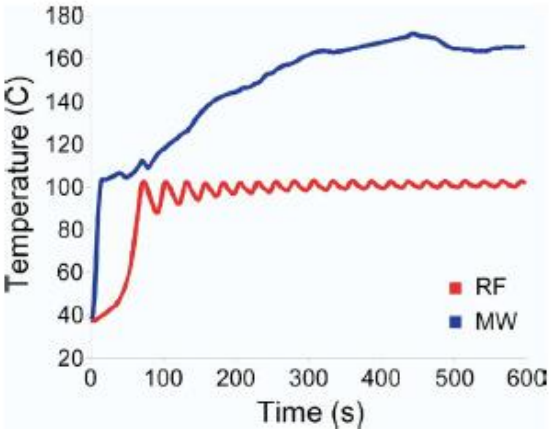

Figure 1.6 Temperature curves of RF ablation and Microwave ablation [51]

Despite technical advantages for treating tumors in the liver, kidney and lung, MW ablation still has some problems which need to be solved. The major disadvantage of MW ablation is the difficulty in generating and efficiently delivering the microwave power [65]. Microwave energy must be carried in coaxial cables, which have a larger diameter and are prone to heating compared to the thin wires used in RF ablation devices. A certain portion of the microwave energy will be absorbed by the cables. Therefore, improvements in cable or applicator design are necessary to improve the efficiency of power delivery. Another drawback is that excessive energy delivery may

cause an overheating problem along the proximal shaft of the antenna [51], [66]. Although several groups have alleviated this problem by cooling the antenna [50], [65], the increased complexity and coaxial space required for antenna cooling systems creates a technical burden to new device designs and adapting microwave technology for new clinical approaches.

1.2.3 Other thermal ablation techniques

Beside RF and MW ablation, there are several thermal ablation techniques in development or common use as outlined below.

Cryoablation

While RF and MW ablation attempt to destroy targeted tissue by cytotoxic hyperthermic temperatures induced by electrical current or EM fields, cryoablation achieves cell necrosis through hypothermic temperatures. In cryoablation, liquefied gas such as nitrogen expands at the end of cryoprobe tip and then creates heat-sink to reduce tissue temperature as low as -160^{o}C (the Joule-Thomson effect) **(Figure 1.7)** [47]. This extremely low tissue temperature causes intracellular ice formation near the cryoprobe, which mechanically expands the cell membrane beyond repair and kills the cells. For the cells more peripheral to the cryoprobe, the temperature decreases slower and then cause extracellular ice formation, leading to a change of osmolality within the extracellular space that can have a lethal effect on cells [61], [66], [68].

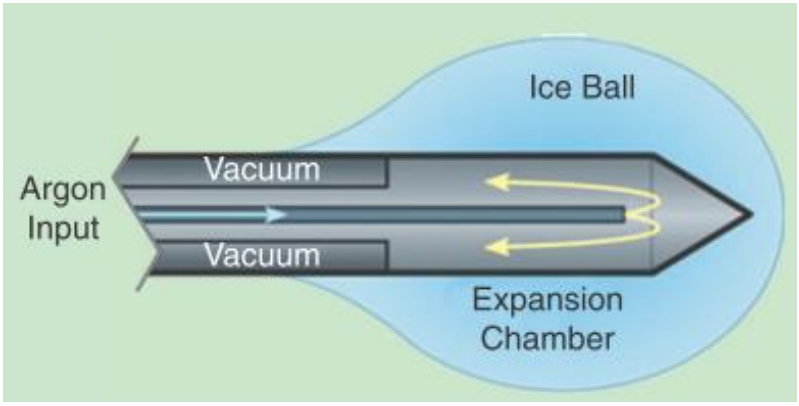

Figure 1.7 Mechanism of cryoablation [47]

Cryoablation has some advantages over heat-based ablation [47], [69], [70]. First, multiple probes (up to 25) can be used treat tumors larger than 3-5 cm in size or sculpt the ablation zone to the exact shape of the tumor. The ice ball is highly visible on medical imaging modalities to allow for real-time ablation monitoring. This is a perceived advantage for many practitioners of cryoablation. However, cryoablation relies exclusively on thermal diffusion, which makes the transfer of heat more dependent on local tissue properties and then reduces the size of ablations a given device can create in low-thermal conductivity tissues such as cirrhotic liver, lung and bone. As a result, multiple freeze-thaw cycles are necessary to increase ablation size and cell killing efficiency during cryoablation, leading to prolonged treatments of 30-60 minutes. Cryoablation is also more expensive than other ablation techniques due to the use of multiples probes and compressed, liquefied gas.

High-Intensity Focused Ultrasound (HIFU)

Ultrasound is widely used in medical imaging for diagnosis. The frequency range of diagnostic ultrasound is from 1-20 MHz. However, the frequency range and the energy level of HIFU are higher than diagnostic ultrasound. Typically, the HIFU transducer will produce an ultrasound beam with high energy in the frequency range of 0.8-3.5 MHz and focus it on the targeted region, causing rapid heating within the tissue, or by inducing cavitation that can mechanically disrupt the tissue **(Figure 1.8)** [47], [71]–[74].

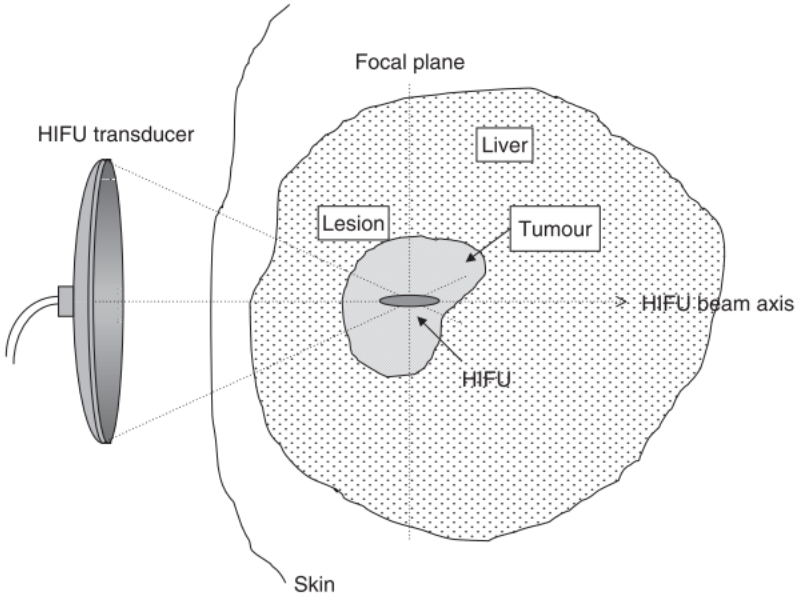

Figure 1.8 Diagrammatic illustrator of HIFU [71]

The major advantage of HIFU is the ability to ablate tissue noninvasively because the ultrasound beam can penetrate through different tissue layers between the transducer and target region [47], [75]. Another advantage is that the tissue surrounding the targeted region has less risk of thermal damage since the acoustic beam will only converge inside the targeted region. However, the resulting ablation zone is quite small (similar to a grain of rice) since energy was lost when penetrating many tissue layers [75]. Moreover, scattering and reflection from tissue interfaces can cause additional damage to non-targeted tissue [76]. Finally, and perhaps most significantly, the ability to delivery HIFU is limited to tissues and anatomic windows which are amenable to ultrasound wave propagation; HIFU is not a good therapy for tumors of the lung or in locations where access is hindered by bone or breathing motion [77].

Laser ablation

Lasers are widely used in medical applications on delicate regions and organs such as eye or skin. However, the use of lasers in tumor ablation has been limited to the past two decades. In laser ablation, laser light energy with 600 to 1,000 nm wavelength is emitted from laser source including pumped neodymium-doped yttrium garnet and semiconductor diodes and then passed to tissue through fiber-optical applicators. Tissue heating is induced around the applicator much like RF or MW ablation [47], [66], [75].

Compared to RF and MW ablation, the most important advantage of laser ablation is the compatibility with MRI since the applicator is fabricated from glass optical fiber [78], [79]. Therefore, the intra-procedural information of temperature and thermal dose can be accurately measured. Moreover, laser light is a precise energy, which could be used to treat tissues in thermally sensitive regions such as the brain [47]. However, the light scattering and rapid absorption by most biological tissue limits the penetration of light energy and the size of ablation zones [80]. In addition, laser light cannot penetrate through charred or desiccated tissue so, like RF ablation, heating efficiency decreases along with treatment time [81], [82].

1.3 Imaging for ablation

Compared to traditional resection surgery, “minimal invasiveness” is the most important feature of thermal ablation. Therefore, reliable medical imaging techniques are necessary for thermal ablation from the beginning to the end of the procedure. Physicians need to extract crucial information from medical imaging to plan and monitor the treatment, and to evaluate the treatment efficacy.

1.3.1 Diagnostic imaging

Diagnostic imaging is a crucial tool for physicians not only to assess the progress of cancer but also to acquire geographical information for planning any treatment. In thermal ablation,

diagnostic imaging is also necessary for physicians before the procedure to identify tumor location and characteristics such as type and diameter. Tumor location information can assist physicians in determining the location of applicator insertion and sometimes becomes an important factor in ablation device selection. The information of type and diameter can help physicians to determine the parameters (eg. power, treatment time) of thermal ablation since different settings will significantly influence the shape and size of ablation zone, which are highly related to the overall treatment efficacy.

To select the appropriate medical imaging modalities in diagnosis before treatment, lesion visibility is a key factor. All the medical imaging modalities can provide adequate lesion conspicuity due to the progress of imaging techniques [52], [83], [84]. Thus, the choice of imaging modalities highly depends on the performance of tumor visualization and the task of usage. For example, ultrasound imaging (US) or computed tomography (CT) may be chosen as diagnostic imaging when intra-procedural monitoring is required during treatment. Currently, ultrasound imaging (US) is the most popular imaging modality in liver cancer screening due to low cost and almost instantaneous image acquisition. However, the visualization of many lesions is poor and imaging windows can be obscured by overlying bone or gas-containing structures. Magnetic resonance imaging (MRI) is another choice since it can provide volumetric visualization of tumors and lesions. Contrast agents can be used to discriminate malignant or benign tumor. However, the monetary cost of MRI is high and scanning times are much longer compared to ultrasound imaging. Compared to previous imaging modalities, computed tomography (CT) is a balanced choice since it can provide good spatial resolution with shorter acquisition time and cost compared to MRI. In addition, there are CT-compatible contrast agents that could also help in differentiating HCC from normal liver or benign tumors. However, the issue of excessive radiation dose in CT is an important

factor to consider for younger patients, and for repetitive imaging associated with oncologic monitoring. Moreover, iodinated contrast-agent, which is widely used to enhance intensity contrast between abnormal and normal region in CT imaging, may damage patient's renal function and induce severe allergies to specific patients.

1.3.2 Guidance imaging

When the location of tumors is known, it is necessary to insert the applicator into the tumor before the treatment begins. Therefore, guidance imaging is required at this stage to ensure the applicator is in the right location inside the tumor. Errors in applicator placement may lead to insufficient coverage by the ablation zone or even additional thermal damage in surrounding healthy tissue.

Since most applicators are relatively visible under all of the medical imaging modalities described previously, the selection of imaging modality is determined by personal preference and research interest as well. Ultrasound imaging is commonly chosen since it can provide real-time visualization of applicator insertion and placement relative to the target lesion [52]. Recently, real-time CT fluoroscopy is preferred by many US institutions since it can provide volumetric visualization of the applicator relative to the target lesion **(Figure 1.9)**. [52]

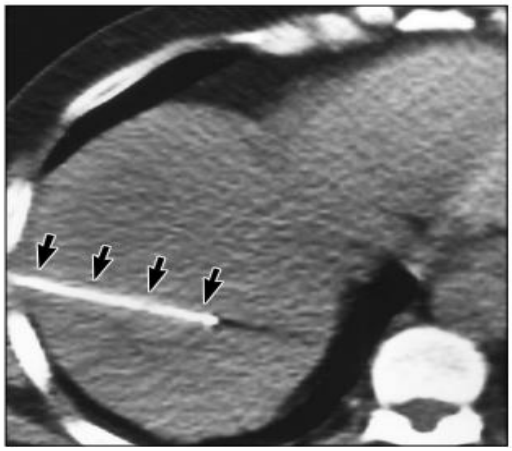

Figure 1.9 CT fluoroscopy image for guidance imaging. The arrow indicates the RF electrode centered in Tumor [52]

1.3.3 Monitoring imaging

There are many factors that significantly influence ablation zone shape and size that can affect whether the ablation zone covers the target lesion. For example, the malfunction of applicators during a procedure leads to inadequate treatment. Unusually high or low blood flow in the tissue can lead to ablation zones that are smaller or larger than anticipated. Occasionally applicators can shift in tissue due to breathing motion, external forces on the applicator or feeding cables, or gantry/bed movement. To assess the evolving treatment effect and discover and correct abnormal situations, intra-procedural monitoring imaging is beneficial.

Typically, ultrasound imaging is used in real-time ablation monitoring [52], [85], [86]. However, visualization of the ablation zones may be compromised by bubbles created during the ablation, which scatter and attenuate the ultrasound signal. In addition, ultrasound imaging includes typically only a single focal plane, limiting the ability to assess the entire ablation zone relative to surrounding anatomic structures over time. MRI imaging offers some intriguing possibilities for real-time thermal ablation monitoring. Several groups have attempted to utilize MRI imaging to estimate the temperature during ablation procedures, which is highly related to ablation zone size and shape [87]–[90]. However, few ablation technologies without metal applicators can allow quality MRI imaging with the applicator in place. CT could also be used in real-time ablation monitoring [91], but dose accumulated during repetitive CT scanning is a major drawback and low-dose scanning may not yield sufficient image quality for accurate assessment of the ablation zone.

1.3.4 Post-ablation imaging

Post-ablation imaging, whether immediately post-procedure or during extended follow-up, plays an important role in the evaluation of treatments. Post-ablation imaging is required to assess the ablative margin (a margin of seemingly normal tissue around the target lesion), which should be at least 5-10 mm to prevent tumor recurrence [92]. Follow-up imaging is required as well to assess the tumor recurrence.

Since post-ablation imaging needs detailed geographical information of the ablation zone, CT and MRI are the main imaging modality for post-ablation imaging. Contrast-enhancement is used in both kind of imaging to differentiate the tumor and ablation zone from normal tissue. In clinics, physicians attempt to evaluate the treatment by just compare the pre-and post-ablation imaging. However, post-ablation imaging sometimes misleads the assessment of ablation zone coverage when using heat-based ablation. Thermal damage generates same water expansion or even dehydration on both tissue and tumor. The intensity of both will be very similar, causing difficulty on discriminating tumor and ablation zone.

Chapter 2 Medical Imaging Modalities used for ablation

As mentioned in the previous chapter, the successful treatment of thermal ablation relies on accurate and efficient imaging techniques. With the progress of science and technology, there are lots of mature medical imaging modalities as well as novel medical imaging techniques. Each kind of medical imaging modality has its own advantages and disadvantages for thermal ablation monitoring. By making the best of their merits, the user can acquire various information about ablation zones from these imaging modalities. This chapter will briefly introduce the physics background of three most commonly used medical imaging modalities: ultrasound imaging (US), computed tomography (CT) and magnetic resonant imaging (MRI) and focused on how researchers and physicians utilized them in ablation monitoring and evaluation. Other novel medical imaging modalities will be shortly introduced as well. At the end of this chapter, we will discuss the limitation of those imaging modalities in real-time ablation monitoring.

2.1 Ultrasound imaging (US)

Ultrasound was first used in 1912, to help search for the sunken Titanic. During WWI and WWII, ultrasound was used in SONAR (Sound Navigation and Raging) systems to detect underwater enemy submarines. The mechanism of SONAR is quite similar to current diagnostic ultrasound imaging, which was to transmit an ultrasound wave into water and receive and analyze the echo. Ultrasound was first used in disease diagnosis by Karl Dussik, the neurologist and psychiatrist at University of Vienna, to locate brain tumors. Nowadays, ultrasound imaging has become one of most common medical imaging modalities and has developed many novel techniques to improve the image quality and acquisition time and acquire new information such as tissue stiffness or temperature by calculating according to received ultrasound signal.

The essential principle of ultrasound imaging is to utilize pulse-echo to implement the display of objects [93], [94]. In general, the transducer emits a pulse of sound waves with the frequency

between 1 to 20 MHz to target region. Since the tissues inside the target region have different characteristics with respect to the ultrasound wave, reflection when the wave penetrates through tissue layers generates echo signals **(Figure 2.1)**. These echoes return back to the transducer with varying phase, direction and amplitude. The envelope of the echo is detected for amplitude estimation and then the whole signal is logarithmically compressed to adapt for human vision. In ultrasound imaging, there are three basic modes: A- mode, B-mode and M-mode. For diagnostic ultrasound imaging, B-mode, which is also called Brightness-mode is most common. B-mode can reconstruct 2D image by emitting and receiving the ultrasound waves from location-switched ultrasonic element in transducer, which gathers echo information along a second dimension.

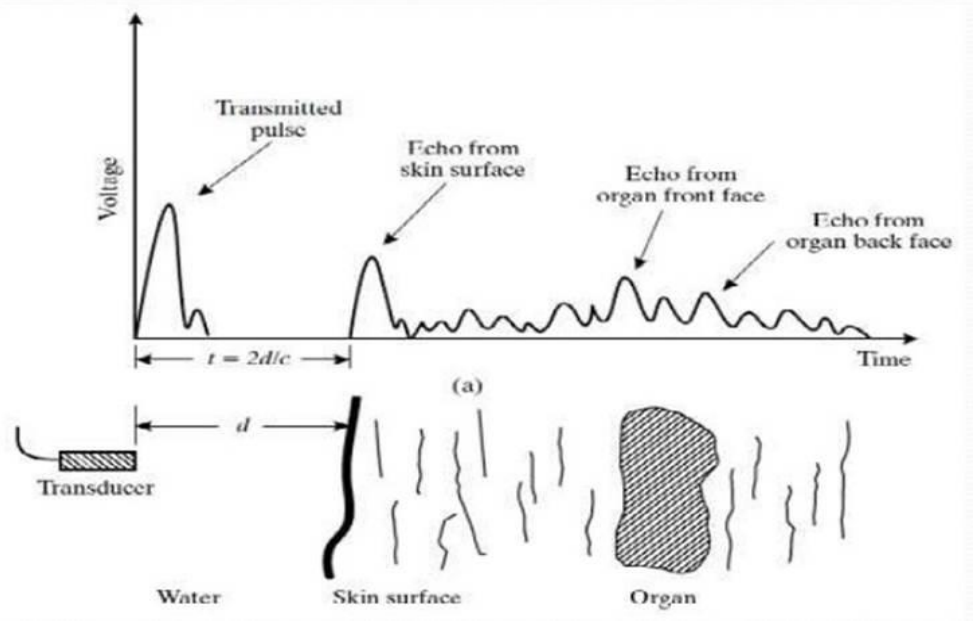

Figure 2.1 the mechanism of ultrasound imaging. The interface of skin and organ reflected ultrasound wave with higher intensity due to large difference of tissue characteristics. [95]

The reason that ultrasound image could describe different types of tissues is that different tissues have different density and homogeneity, which influence acoustic impedance,

$$Z = \rho_0 c = \sqrt{\frac{\rho_0}{\kappa}} \tag{2.1}$$

Where ρ_0 is undistributed mass density of tissue, c is the sound speed, which is varied in different medium and κ is the compressibility of medium. Based on the acoustic impedances of the different medium at the both side of interface, we could estimate the reflection coefficient and transmission coefficient,

$$R = \frac{Z_2 cos\theta_i - Z_1 cos\theta_t}{Z_2 cos\theta_i + Z_1 cos\theta_t} \tag{2.2}$$

$$T = \frac{2Z_2 cos\theta_i}{Z_2 cos\theta_i + Z_1 cos\theta_t} \tag{2.3}$$

Where Z_1 and Z_2 is acoustic impedance of the medium at both side of interface, θ_i is incidence angle of ultrasound wave and θ_t is transmission angle. Both of these angles follow Snell's law. The amplitude of echo is highly relevant to reflection and transmission coefficient. Therefore, the B-mode ultrasound image could be considered as a map of acoustic impedance.

Tissue after ablation change characteristics such as density and the amount of water content. Ablation may also generate charred or desiccated regions. All the behaviors above may change acoustic impedance and should be clearly seen on B-mode ultrasound image in theory. While the visualization a cryoablation iceball boundary is excellent, the display of hyperthermic ablation zones is not as clear. Heating tissue will generate gas, microbubbles and necrosis on targeted tissue, which will generate acoustic shadowing on B-mode ultrasound imaging. The hyperechoic area caused by ablation might sometime disappear within 30 min while the escape of gas.

Several research groups have attempted to develop novel techniques to improve visualization and extract further information from ultrasound imaging. Color Doppler imaging could estimate blood flow by measuring the phase change of received signal since the variation of blood flow causes frequency shift of received signal based on Doppler effects [96], [97]. Due to less blood perfusion in ablated tissue, Doppler imaging could enhance the visualization of ablation zone by

displaying the lower perfusion region [98]–[101]. Shear wave elastography is an alternative method to detect ablation zone by investigating the stiffness of tissue. Ablated tissue will become stiffer due to protein denaturation and tissue desiccation caused by heating [102]–[108]. A shear wave is generated inside the human body and penetrates the target tissue horizontally. The propagation speed of shear wave varies depend on the tissue stiffness. Thus, the stiffness of region will be acquired by estimating the shear wave velocity **(Figure 2.2)** [109]**.**

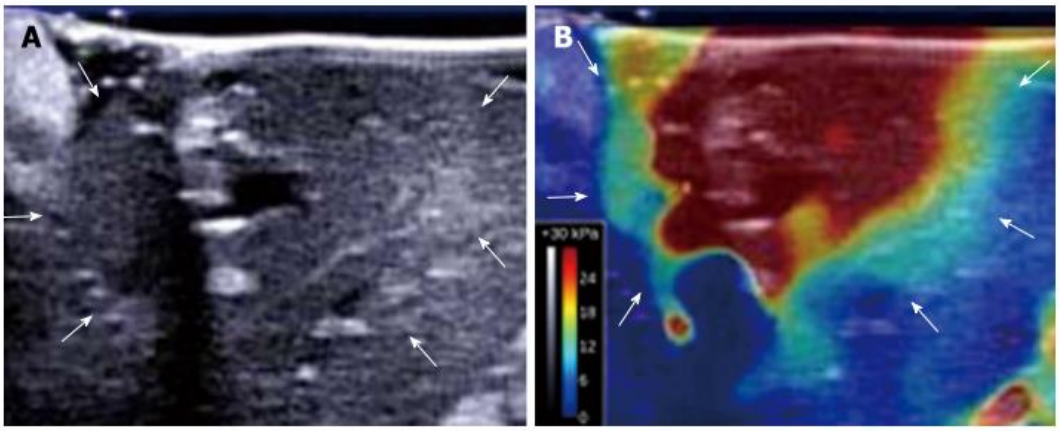

Figure 2.2 - Thermal lesion on the liver display by ultrasound imaging(a)B-mode US and (b) shear wave elastography. The shear wave elastography image clearly display the ablated tissue.[104]

Recently, ultrasound Nakagami imaging techniques has been applied on monitoring and evaluating the efficacy of several heat-based ablation techniques [110]–[114]. Nakagami image is a map composited with Nakagami parameter, which could indicate the concentration and distribution of scatterers [115], [116]. Since heat-based ablation will generate gas bubbles inside ablation zone. These bubbles will contribute to changing the distribution of backscattered signal and then increasing the Nakagami parameter [110]. Thus, the ablation lesions will be the region with high intensity on Nakagami images. Another recent novel techniques is to estimate temperature from received ultrasound signal since the parameters of reflected signal are

temperature-dependent [117], [118]. Once the temperature is estimated, the ablation lesion could be delineated by following the boundary of 60^{o}C near the applicator.

Besides the above methods which trying to extract additional physical and physiological information from received ultrasound signal, contrast agent injection before or immediately after ablation is a direct method to increase the contrast between normal and ablated tissue [119]–[123]. In contrast-enhanced ultrasound imaging, a gas-filled microbubble solution is used since microbubbles have high ability to reflect ultrasound waves. Therefore, the received signal has higher amplitude if the region retains more of the contrast agent. After ablation, the ablation zone has less perfusion, leading to less enhancement compared to normal tissue. Therefore, the contrast between normal and ablated tissue increase, which makes ablation zone more distinguishable **(Figure 2.3).**

Figure 2.3 Liver RF ablation on ultrasound imaging (a) B-mode US (b) CEUS. The ablated lesion become clearer 180s after contrast agent injection compared to traditional US. [123]

2.2 Computed Tomography (CT)

CT was invented in 1972 by Godfrey Hounsfield, who was the engineer in EMI Laboratories, and Allan Cormack, who was the physicist at Tufts University. In 1974, Hounsfield developed the first CT scanner, which could only be used for head imaging. In 1974, the first whole body scanner became available. At the time, it took several hours to acquire the raw data of a slice and days to reconstruct a single slice image. Nowadays, the acquisition time of an entire CT volume is just between 10 to 20 seconds, and the image quality and resolution have realized significant improvements, leading CT to become one of most common medical imaging modalities worldwide.

The basic principle of CT imaging is to measure the attenuation of X-ray energy to generate an image [124]. The energy of X-ray decreases by scattering and absorption from tissues when passing through an object in the body. The relationship between the initial energy of an X-ray beam and the energy of the X-ray received by a detector is,

$$I = I_0 e^{[\sum_i (-\mu_i x_i)]} \tag{2.4}$$

Where I_0 and I are the energy of initial X-ray and the X-ray passed through the object. μ_i is linear coefficient of material i inside the object and the x_i is the length X-ray traveled in material i. The linear attenuation coefficient describes the fraction of a beam of X-ray absorbed or scattered per unit thickness of material, which is highly relevant to material density and or effective atom number.

The pairs of X-ray tube and detectors, which are used in emitting and receiving multiple X-ray beams, rotate with respect to center and collect the distribution of energy attenuation at each increment of rotation angle **(Figure 2.4).** Therefore, the projection image data with dimension of location of detector and rotation angle could be acquired. The image slice is then reconstructed by

Filtered Backprojection (FBP) algorithm. In mathematics, the projection data is transformed to Fourier space by the following formula,

$$\tilde{R}(k,\theta) = \int_{-\infty}^{+\infty} R(\rho,\theta) e^{-i2\pi k\rho} d\rho \tag{2.5}$$

Where $R(\rho,\theta)$ is the measured projection data at detector location ρ and rotation angle θ. The transformed data is then filtered by a ramp filter on frequency domain (k) only and convert back to polar domain,

$$F(z,\theta) = \int_{-\infty}^{+\infty} \tilde{R}(k,\theta)|k| e^{i2\pi kz} dk \tag{2.6}$$

Finally, the filtered is then backprojected to spatial domain to acquire image,

$$f(x,y) = \int_0^{\pi} F(z = xcos\theta + ysin\theta, \theta) d\theta \tag{2.7}$$

In fact, the whole processed could be converted as convolution in spatial domain

$$f(x,y) = -\frac{1}{2\pi^2\rho^2} * R(\rho,\theta) \tag{2.8}$$

Where $-\frac{1}{2\pi^2\rho^2}$ is the frequency ramp filter in spatial domain. If we express the formula in integral convolution format, the formula is,

$$f(x,y) = -\frac{1}{2\pi^2} \int_0^{\pi} \int_{-\infty}^{+\infty} \frac{R(\rho,\theta)}{(\rho - xcos\theta - ysin\theta)^2} d\theta d\rho \tag{2.9}$$

Which is just a 2D inverse Radon transform [125], [126]. In practice, the measured projection data will filtered by shift-invariant Ramp filtering to eliminate the artifact made by superimposing the projection data from each rotation angle at same pixel, which is almost same procedure as the mathematic proof.

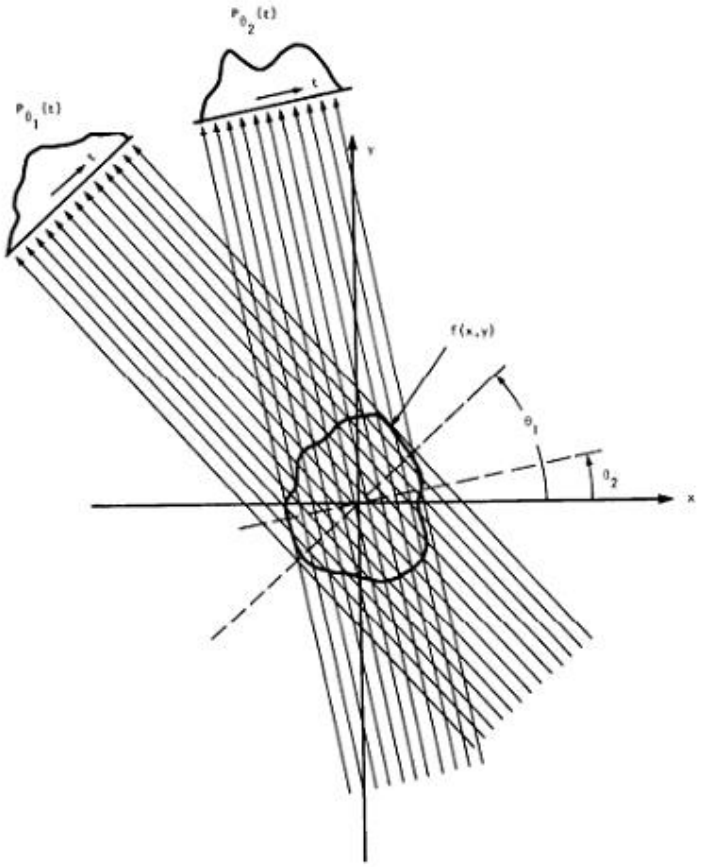

Figure 2.4 the schematic of CT scanning process. [124]

In CT imaging, the ablation zone is the area with low intensity due to thermal expansion of water, coagulative necrosis, tissue desiccation with water vaporization and bubbles, and hemorrhagic products that decrease perfusion of the treated region [127]–[129]. However, the contrast between the ablated lesion and normal tissue is poor at the ablation periphery [85], [130], [131]. To enhance visualization of the ablation zone, iodinated contrast agent is injected intravenously to enhance the background liver parenchyma [85], [132], [133]. Iodinated material does not readily penetrate into the coagulated ablation zone, resulting in differential enhancement compared to perfused background tissue and a more distinguishable ablation zone **(Figure 2.5)**.

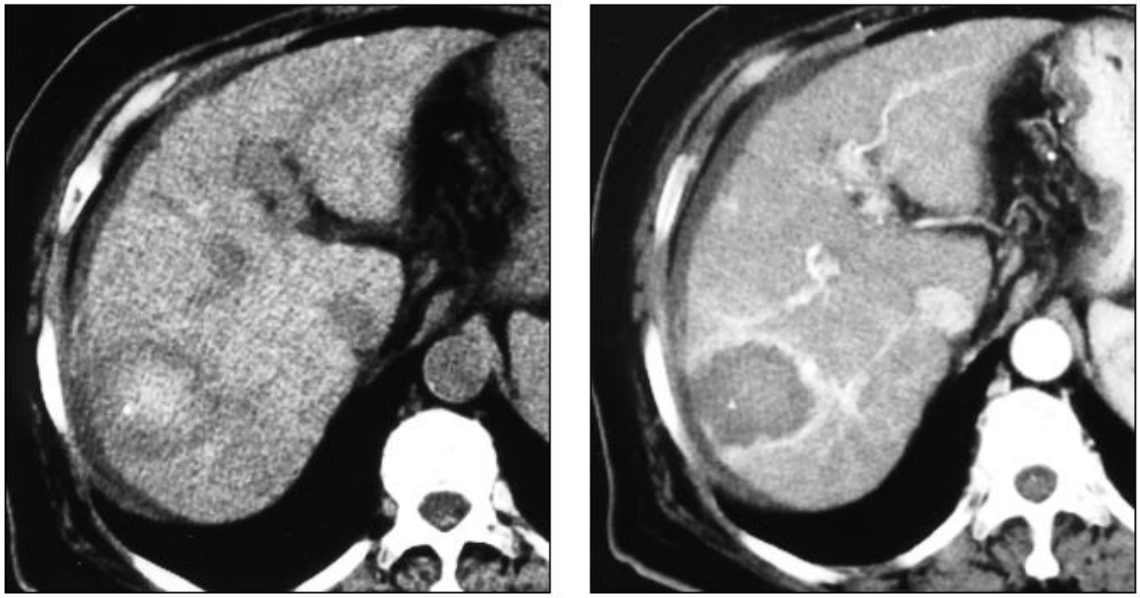

Figure 2.5 CT Post-ablation imaging (left) unenhanced CT and (right) Contrast-enhanced CT. The ablation zone become more visible due to parenchymal enhancement [127].

Recently, functional CT or perfusion CT techniques have emerged for ablation efficacy assessment [134]–[137]. The principle of perfusion CT is similar to CECT except the bolus of contrast agent is injected before scanning, and temporal variations in attenuation are recorded to estimate perfusion parameters such as blood flow rate. Based on the estimated perfusion parameters, physicians can discriminate successful treatment regions and residual tumor. Besides perfusion CT, dual-energy CT (DECT) is an alternative method to accentuate differential contrast enhancement [138]–[140]. DECT acquires CT scans with different photon energies (usually one is high voltage and one is low-voltage). Each material in the imaging volume has a unique attenuation spectrum relative to the input energy. Therefore, by acquiring data and multiple energies, the materials can be decomposed from the imaging volume. For example, a map of iodine can be generated and used to indicate residual tumor since the distribution of iodinated material is highly related to blood perfusion.

Even without using contrast agent to enhance the visualization of ablation zone, the temperature of tissue during ablation could now be estimated from traditional CT scanning. Several research groups generated mapping between CT attenuation and temperature by experiments and linear regression [141]–[144]. Since temperature of ablation tissue was high during the procedure, CT temperature mapping could be used to detect ablation zone by temperature thresholding. To date this type of imaging has not been widely utilized due to the inherent noise in CT relative to changes induced by the ablation itself.

2.3 Magnetic resonance imaging (MRI)

The history of developing MRI imaging is quite similar to CT imaging development [145]. In 1973, Paul Lauterbur, the chemist and the pioneer of nuclear magnetic resonance, invented the first NMR image, which reconstructed by the emitted radio wave from atomic nuclei exposed to an extremely strong magnetic field. Five years later, Raymond Damadian, who was the first researcher discovered the difference of hydrogen signal between cancerous and healthy tissues by NMR machine, established the first MRI scanner based the result from NMR imaging and used it to scan healthy human body. Nowadays, the acquisition time of MRI imaging has been improved compared to the first MRI scanner, and the function of MRI become more various. For example, MRI could be used to estimate blood perfusion and tissue temperature, which may be highly relevant to certain disease or the efficacy of treatment. Thus, MRI become more and more common and powerful and is widely used in lots area in medicine.

The basic principle of MRI imaging is to record signal release from relaxation of the nuclear spin of water proton in a static, strong magnetic field and then reconstruct these information as an image [145]. In MRI imaging, a static external magnetic field is applied on object. The randomly oriented protons in water nuclei are aligned and spin with Larmor frequency,

$$\omega_0 = \gamma B_0 \tag{2.10}$$

Where B_0 is external magnetic field and γ is gyromagnetic ratio. When alignment finishes, an additional radiofrequency (RF) energy applied to the object excites the proton from its resting state. After removal of this additional RF pulse energy, the excited protons tend to realign with B_0 following longitudinal magnetization recovery and transverse magnetization decay **(Figure 2.6)**. The longitudinal relaxation time (T_1) and transverse relaxation time (T_2), which control the duration of relaxation process, fit in the following formula,

$$M_z(t) = M_z(0)(1 - e^{-\frac{t}{T_1}}) \tag{2.11}$$

$$M_{xy}(t) = M_{xy}(0)(e^{-\frac{t}{T_2}}) \tag{2.12}$$

Where $M_z(0)$ and $M_{xy}(0)$ are initial magnetization in longitudinal and transverse direction. During the relaxation, the protons emit RF signal with intensity,

$$I = M(0)(1 - e^{-\frac{T_R}{T_1}})\ (e^{-\frac{T_E}{T_2}}) \tag{2.13}$$

Where T_R is the repetition time of RF pulse energy and T_E is the time between the delivery of RF pulse signal and receive the echo. By converting the frequency information in the emitted RF signal from each location in the image plane to corresponding intensity level via Fourier transform, the MRI image is reconstructed and form as gray-scale image matrix.

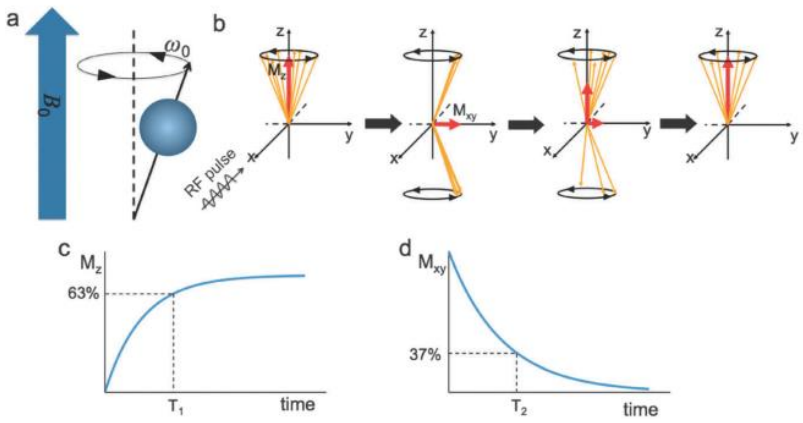

Figure 2.6 Principle of MRI (a)the protons was aligned by external magnetic field. (b) the process of relaxation (c) & (d) the temporal variation of longitudinal and transverse magnetization . The longitudinal relaxation time (T_1) is defined the time when recovering 63% of initial longitudinal magnetization, and the transverse relaxation time (T_2) is defined as the time when recovering 37% of initial transverse magnetization [146].

Based on the formula (2.13), there are two common MRI imaging sequences. T1-weighted imaging reconstructs image with shorter T_E and T_R time. Hence, the materials with short T_1 such as fat will have high signal intensity and then become bright in T1-weighted imaging. T2-weighted imaging reconstructs image with longer T_E and T_R time. Therefore, material with short T_2 time will lose most of signal and then become dark in T2-weighted imaging. **(Figure 2.7)**

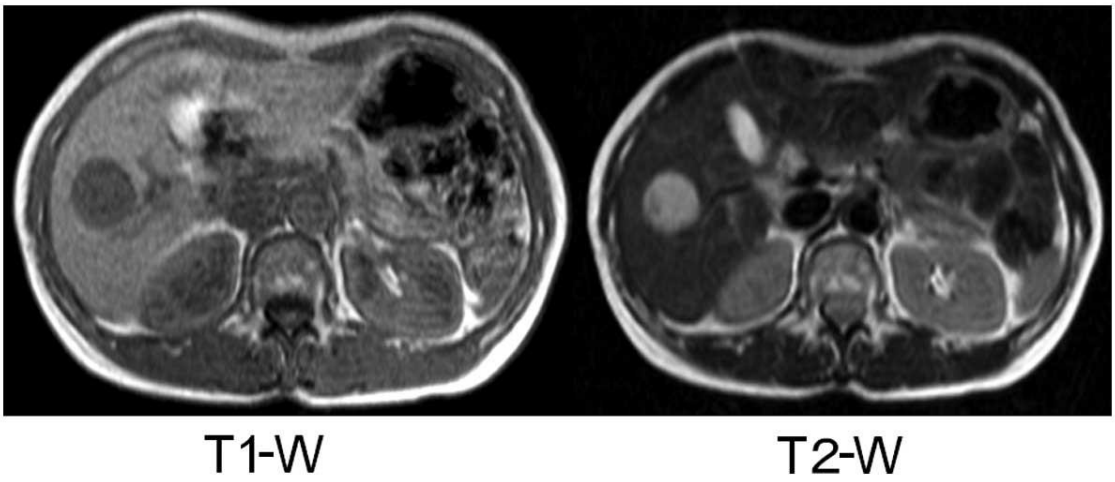

Figure 2.7Abdominal MRI-image (left)Abdominal T1-weighted image (right) Abdominal T2-weighted image. The region with HCC display hypointensity in T1-weighted image and hyperintensity in T2-weighted image.[147]

Thermal ablation will cause dehydration and produce coagulation necrosis in the targeted tissue. Therefore, the ablation zone is displayed as a low-intensity area in T2-weighted imaging and a high-intensity area in T1-weighted imaging since losing water content will increase brightness in T1-weighted imaging and decrease brightness in T2-weighted imaging [148]. However, the periphery of the ablation zone in both T1-weighted and T2-weighted imaging have ambiguous signal due to the irregular evolution of inflammation and necrosis. Hence, contrast-enhanced MRI, which usually uses Gadolinium-based contrast agent, is used to enhance the contrast between the treated region and normal parenchyma [127], [149], [150]. Gadolinium shortens T1 relaxation time in tissue with adequate perfusion. Hence, the less perfused ablation zone becomes more distinguishable due to enhancement of normally perfused background tissue [151].

Besides contrast-enhanced MRI imaging, MR thermometry is an alternative method to monitor and assess ablation since tissue temperature is directly related cellular death. Since all MRI parameters such as T1 and T2 are temperature-sensitive, tissue temperature can be estimated with appropriate sequences and temperature references. Among the various MR thermometry techniques, proton resonant frequency shift (PRF) thermometry has attracted the most attention in monitoring and assessment of thermal ablation [79], [152], [153]. The key factor of PRF thermometry is hydrogen bonds [154], [155]. Hydrogen bonds normally existing between water molecules to keep the distance between electrons and protons lead to an increase in the resonant frequency of that tissue. When temperature increases, hydrogen bonds will stretch, bend and break, which makes the electrons shield the protons from the external magnetic

field, resulting in a decrease of resonant frequency. According to this relationship, the tissue temperature could be estimate by the following formula,

$$\Delta T = \frac{\varphi - \varphi_0}{\alpha \gamma B_0 T_E} \quad (2.14)$$

Where B_0 is external static magnetic field and T_E is echo time. α is PRF coefficient and φ is imaging phase. PRF themometry could quickly estimated the temperature so that could be used in real-time ablation moniroting [87], [89], [156], [157].

2.4 Other Imaging modalities

Besides US, CT and MRI, there are several advanced imaging modalities arising in ablation monitoring and assessment.

Positron emission tomography (PET)

Position emission tomography is a function imaging modality which could measures physiological properties such as blood flow and metabolism. The mechanism of PET is a little similar to CT except the photons are emitted by the tracer inside the object [158]. Tracers such as oxygen-15, fluorine-18 and carbon-11 were injected intravaneously into the targeted region. The tracer will emit a positron which colliding with an electron in the tissue and then result in photons emission. These emitted photons are detected by a detector, converted into electrical signal and then formed image **(Figure 2.8)**. Usually, PET is accompanied with the aid of X-ray CT due to low spatial resolution and less anatomical information.

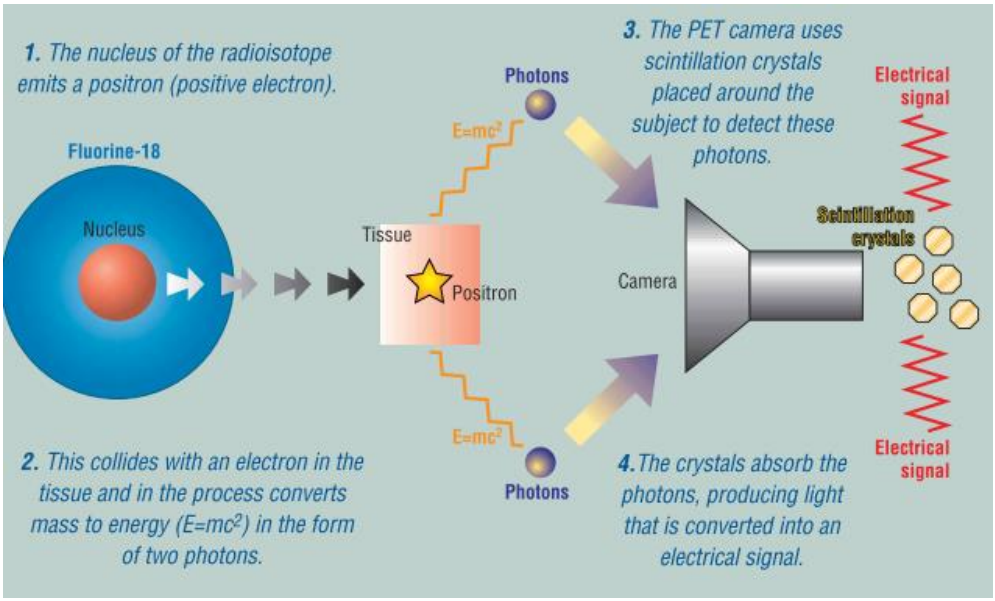

Figure 2.8 illustrator of PET imaging [159]

Currently, several research groups attempt to use fluorine-18 PET in evaluating efficacy after ablating a tumor [160]–[165]. Fluorine-18 will be trapped inside tumor, which will appear high-intensity region in PET image. After thermal ablation, cell destruction and tissue vaporization might release fluorine-18 into veins or surrounding tissue. Therefore, the concertation of fluorine-18 in the ablated tumor region decreases, which causes significant intensity decreases on the same region in PET images **(Figure 2.9).** Despite several encouraging results, PET is not widely used for ablation monitoring due to tracer availability and radioactivity, system cost and availability for procedures, and generally acceptable results with other imaging methods.

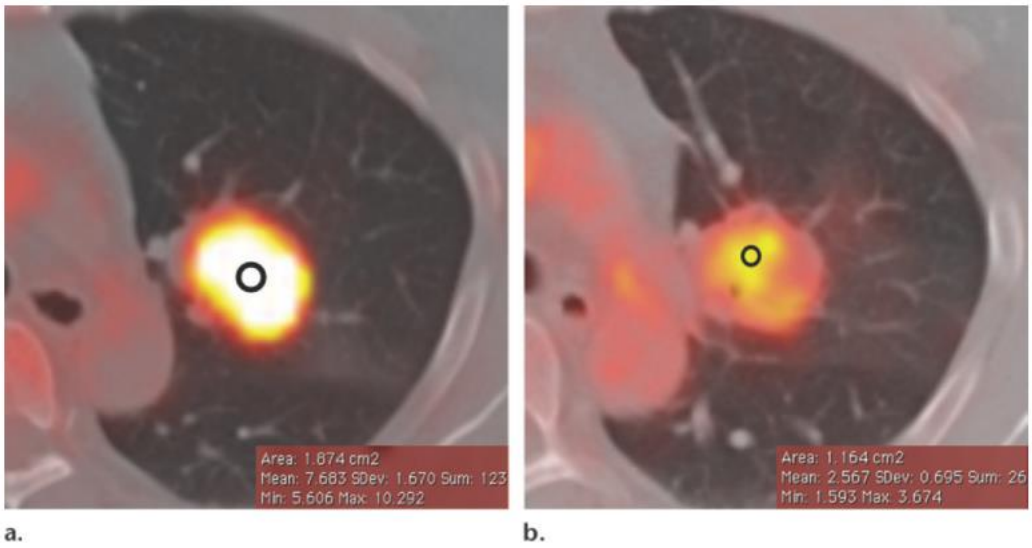

Figure 2.9 Fused PET/CT images of a left suprahilar non–small cell lung carcinoma (a) before ablation. (b) after ablation. [160]

Optical coherence tomography (OCT)

Optical coherence tomography is a novel medical imaging modality. The basic idea of OCT is to produce images by detecting a scattered light wave at different locations inside an object [166], [167]. In OCT, a low time-coherence light is used. The depth-OCT scan is first performed as a reference signal, and the lateral OCT scans are then performed by moving the sample or by scanning the probe beam illuminating the sample. The difference between the reference signal and measured scattered signal is estimated and then used to reconstruct images **(Figure 2.10).** Due to using infrared or visible wavelength light, OCT has a high resolution in the range of micrometers.

Since tissue density and characteristics will be changed after thermal ablation, the scattering parameter will change as well and allow contrast between ablated and normal tissue. Currently, few research groups attempt to use OCT in monitoring and assessing ablation on delicate tissues

since the ablation zone will be much smaller at that region and high-resolution is required to avoid additional damage on surrounding tissue [168], [169].

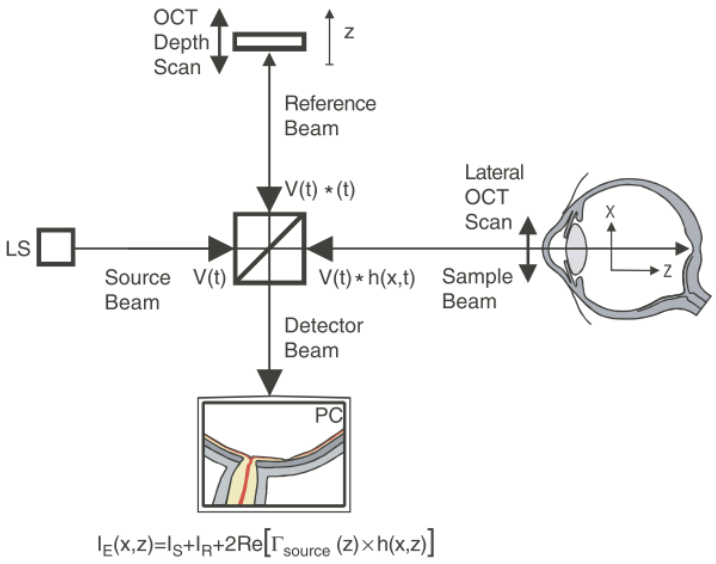

Figure 2.10 the scheme of OCT imaging [167]

2.5 Limitations for ablation monitoring

Current methods for monitoring ablation are focused on immediate post-ablation imaging. The characteristic of tissue will be changed after thermal ablation, resulting in appearance change in post-ablation image. Thus, physicians could monitor and evaluate treatment efficacy by comparing pre-ablation image and immediately post-ablation image. However, there are two challenges which are tough to resolve for monitoring ablation via post-ablation image analysis. First, visualization and recognition of either the tumor or ablation zone is difficult in images acquired immediately post-ablation. Thermal damage will result in water expansion or even dehydration which is same on both tissues and tumors. As a result, the ablated tumor looks like ablated normal liver, making them often indistinguishable on imaging. This can make assessing treatment margin a challenge

and may then increase the probability of tumor recurrence. In addition, it is difficult to correct for treatment errors such as overtreatment (which can cause serious complications) or device failures when relying exclusively on imaging acquired after the ablation procedures **(Figure 2.11)**. Such errors could unnecessarily damage normal tissue or leave residual untreated tumor. Therefore, more effective imaging techniques for monitoring treatment progress, especially for real-time monitoring, are needed for safer, more effective thermal ablation.

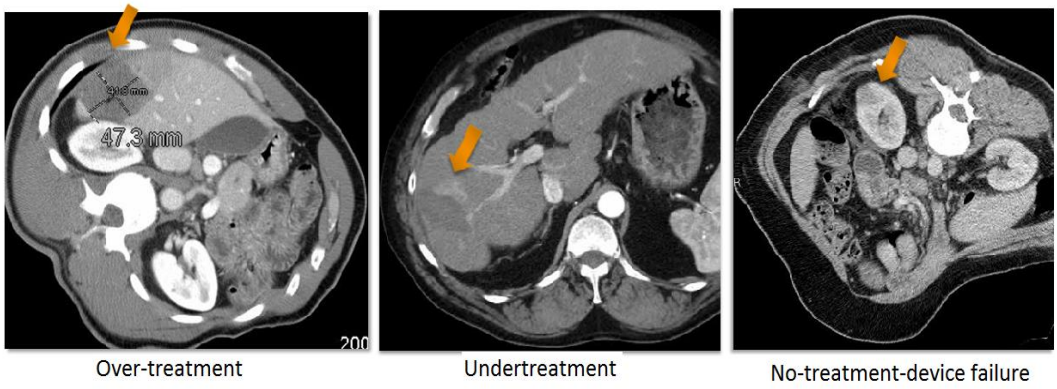

Figure 2.11Examples for poor effects of the treatment undiscovered from the post-ablation image but in follow-up scan. (Left) The body wall was burned due to over treatment, which made substantial pain to patient and prolonged recovery. (middle) The residual tumor (bright region pointed by arrow) discovered in follow-up scan, which will be difficult to re-treat (Right) the small, less ablated region since device was off from targeted region during procedure.

Ultrasound imaging is an appropriate medical imaging modality for real-time ablation monitoring. Conventional B-mode has good image quality with excellent temporal resolution. However, delineating ablation lesions is difficult in about 70% of cases since bubbles produced during high-temperature ablation create scattering artifacts and signal dropout that hinders identification of the ablation boundary [85] **(Figure 2.12).** The other novel techniques have shown promise in improving delineation of the ablation zone, but may still be limited by ablation-induced bubbles and can only be applied in organs with strong ultrasound propagation.

MRI or MR thermometry is alternative methods for real time monitoring with good spatial resolution. However, coarse temporal resolution, a lack of MRI-compatible ablation devices, and high cost of imaging suite time are the main obstacles to wide usage. PET and OCT have good properties to be used in ablation treatment assessment. However, these techniques still require comparison to the pre-ablation image. The unknown appearance of ablation zones make them difficult or intractable for real-time monitoring.

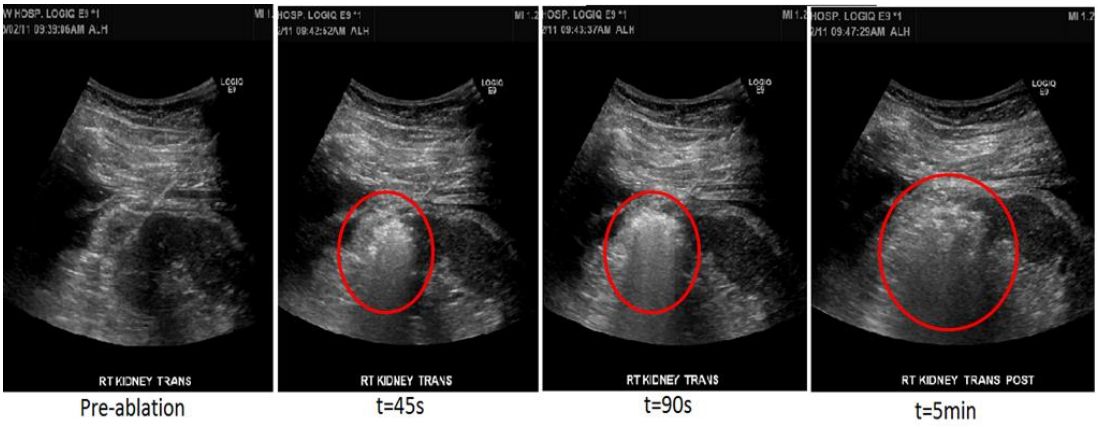

Figure 2.12 Examples for bubble artifact on conventional B-mode ultrasound image made by thermal ablation. The region in red circle was the ablation zone with bubble artifact.

CT is an attractive imaging modality for post-ablation assessment due to several advantages. Firstly, volumetric imaging in CT can provide 3D information to help radiologists evaluate the treatment without blind spots and to have advanced analysis such as ablation volume rendering. Secondly, CT data acquisition time takes only a few seconds on modern multi-slice scanners, which is faster than other volumetric imaging modalities (eg. MRI) and is sufficient to capture ablation growth (which typically takes 5-10 min). Therefore, CT has high time resolution and few artifacts from patient motion. Thirdly, iodinated contrast agents used in CECT enhance normal perfused tissue. The ablated tissue, which has no perfusion and low enhancement, is then easily distinguished from the enhanced background liver.

While CECT has many merits, there are two major drawbacks that have kept it out of the realm of real-time monitoring techniques. First of all, repetitive scanning facilitates the accumulation of radiation dose, which may increase long-term health risks in younger patients [170]. Moreover, repetitive contrast-enhanced imaging (and associated repeat doses of iodinated contrast material) could also increase kidney strain, which would be problematic for patients with poor renal function [171], [172]. Therefore, there is still a need for solving these problems to make CECT feasible in real-time ablation monitoring. With these facts in mind, the objective of this thesis is to outline my efforts to develop a real-time (or rapid) serial CECT imaging technique to monitor the growth of thermal ablations intra-procedurally.

Chapter 3 Feasibility of Contrast-Enhanced Computed Tomography in Real-time Ablation Monitoring

(Work was published as: Wu P, Brace CL. "Analysis of iodinated contrast delivered during thermal ablation: is material trapped in the ablation zone?" *Phys Med Biol*. 2016;61(16):6041-6054)

3.1 Introduction

CECT is widely adopted in post-ablation imaging to display the ablation zone. Iodinated contrast material is delivered before CECT scanning, and the perfused region is highlighted by penetration and increased X-ray attenuation provided by the contrast agent. Therefore, the unperfused ablation zone is distinguishable from normal tissue [173]. However, it is unclear whether iodine delivered during ablation might be retained in the ablation zone – trapped by thermal coagulation.

Early hyperthermia will cause increased perfusion and potentially greater delivery of iodinated material to the target region [174]–[176]. When temperatures elevate beyond 60 $^{\circ}$C, the treated tissue will begin coagulating and perfusion decreases rapidly [68]. If sufficient contrast material is trapped inside the coagulation region, it may reduce contrast with the adjacent perfused tissue and reduce visibility of the ablation zone. On the contrary, when temperatures approach 100 $^{\circ}$C, the treated tissue begins dehydrating. The contrast agent may be transferred into the ablation periphery with the water and have no or even positive effect on the contrast with surrounding tissue. Since contrast between the ablation zone and normal parenchyma is a crucial factor in visualization, this study aimed to determine whether iodinated contrast material delivered concurrently with thermal ablation is trapped in the ablation zone, and evaluate whether such trapping might preclude the use of CECT to monitor thermal ablation growth in real-time.

Despite no previous studies on the influence of contrast delivery during ablation in CECT, Hijnen et al has discussed the trapping of contrast during high-intensity focused ultrasound ablation (HIFU) in MRI [73]. They injected Gd-based contrast agent (Gd-CAs) shortly before HIFU started and measured the amount of Gd-CA by R1-mapping. Their results showed that the Gd-CA was trapped in coagulated region and cleared slowly 14 days after treatment. However,

their study focused on the retentive time of trapped Gd-CA, but did not mention about the influence on display of ablation zone. Since the major goal of study is entirely different, they injected contrast agent only once before treatment while our study will more focus on continuously contrast delivery during ablation.

This study aimed to measure not only attenuation but also visibility and sharpness of the ablation zone among groups with and without contrast agent delivery, and with or without perfusion. The temporal attenuation change was measured as well to observe the contrast agent reaction during ablation. The results of our study contributed to a better understanding on the contrast agent during ablation and examine the influence on visualization of ablation zone.

3.2 Materials and methods

3.2.1 *In-vivo* ablation procedure

Microwave ablations were created in the livers of four swine using a 2.45 GHz microwave generator (Certus 140 ; NeuWave Medical Inc., Madison, WI) and triaxial antenna (LK 15; NeuWave Medical Inc., Madison, WI). The antenna was placed transverse to the CT scanner imaging plane. Generator output was 100 W for 5 min. Three contrast material delivery protocols were evaluated sequentially in each animal: (A) no contrast material (control), (B) ablation with iodinated material delivered by blood perfusion, and (C) ablation in an unperfused, iodine-laden liver. In Group B, a 40 ml bolus of iodinated contrast (300 mg/ml iohexol; GE Healthcare, Waukesha, WI) was injected 1 min before ablation and then contrast was infused continuously at 0.3 ml/s to maintain a similar level of enhancement in the perfused liver during the procedure. In Group C, a 50 ml bolus was injected concurrently with the euthanasia solution, and then contrast was infused at 2 ml/s until cessation of heart rhythm to saturate the liver before perfusion ceased.

One or two samples of each protocol were collected in each animal, for a total of five samples per group.

3.2.2 CT image processing

Pre- and post-ablation CT volumes were acquired before and after ablation by using a thin-slice protocol (0.625 mm thickness, 120 kVp, 250 mA; GE 750 HDCT). Intra-ablation CT volumes were acquired at 15 s intervals during each ablation by using a low-dose protocol (0.625 mm thickness, 80 kVp, 80 mA; GE 750 HDCT). The scanning range of all CT volumes extended to at least 3 cm beyond the tip of the antenna. Breath holds were used to reduce motion artifacts.

CT data pre-processing was performed in two steps: co-registration of time series, and metal artifact reduction. CT volumes were co-registered according to the location and the angle of the antenna using rigid transformation [177]. All CT volumes were registered to the first volume in the time series. Metal artifacts were reduced slice-by-slice by forward projecting each image, replacing the metal attenuation data in the sinogram using sparse interpolation, then back projecting the result [178]–[180] **(Figure 3.1).**

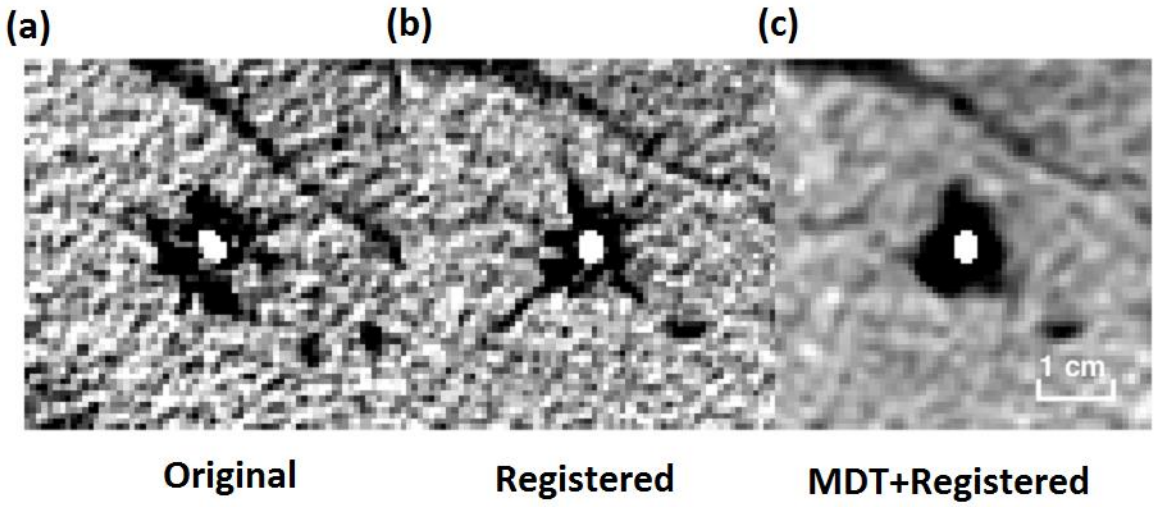

Figure 3.1 The example result for registration and MDT : (a) Original CT image, (b) registered image, (c) MDT for registered image. All figures are equal scale.

A volumetric region of interest (64x64x11 pixels ROI) was manually selected over the central ablation in each CECT volume. Any background air pixels were filled with the mean attenuation of liver to eliminate their statistical influence on post-processing. Each slice was then down-sampled by 4x using neighborhood averaging. Each downsampled, cropped volume was then projected into the axial plane using average intensity projection (AIP) to create a two-dimensional cross-section of the ablation zone in Hounsfield units (HU) noted as the "2D attenuation map" **(Figure 3.2)**. To more generally evaluate attenuation changes over time, each down-sampled slice was converted into a one-dimensional dataset by using a polar transformation with averaging over the angular domain. The resulting profile was noted as the "1D attenuation profile" **(Figure 3.3).**

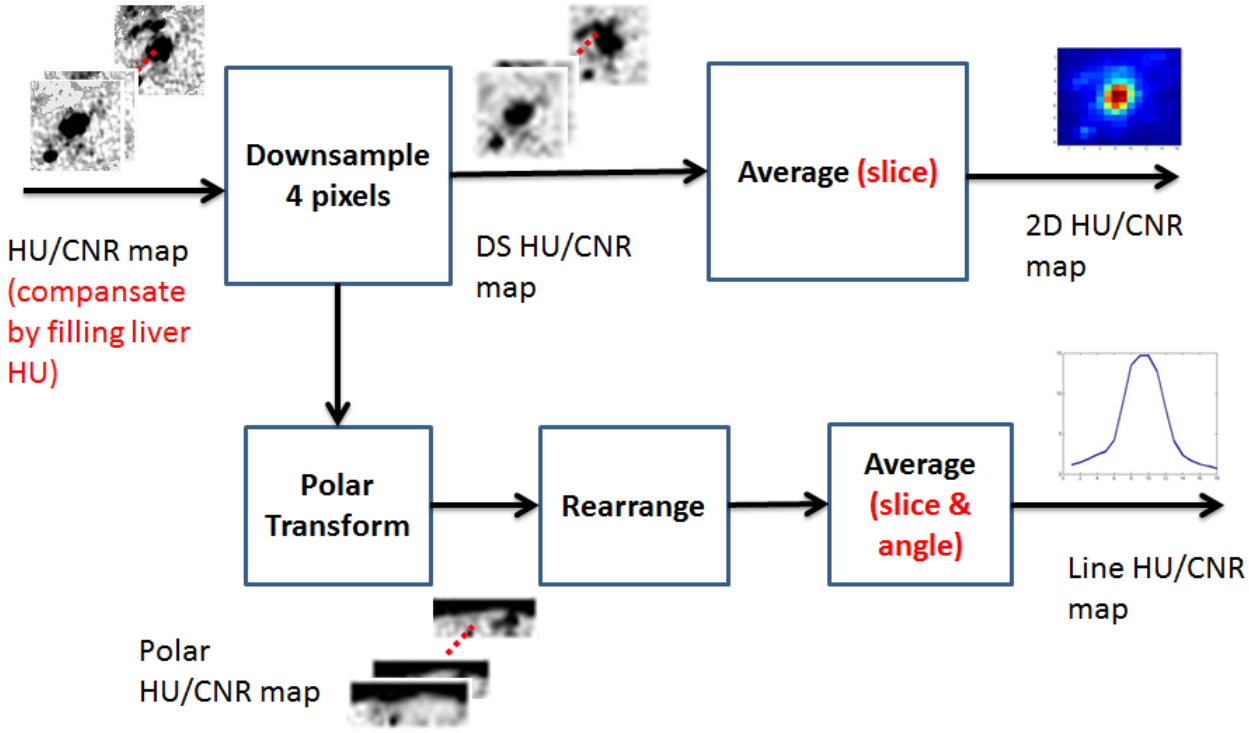

Figure 3.2Analysis flow chart to produce the average intensity projection (AIP, upper track) and 1D angle-averaged attenuation map (lower track) for each CT volume.

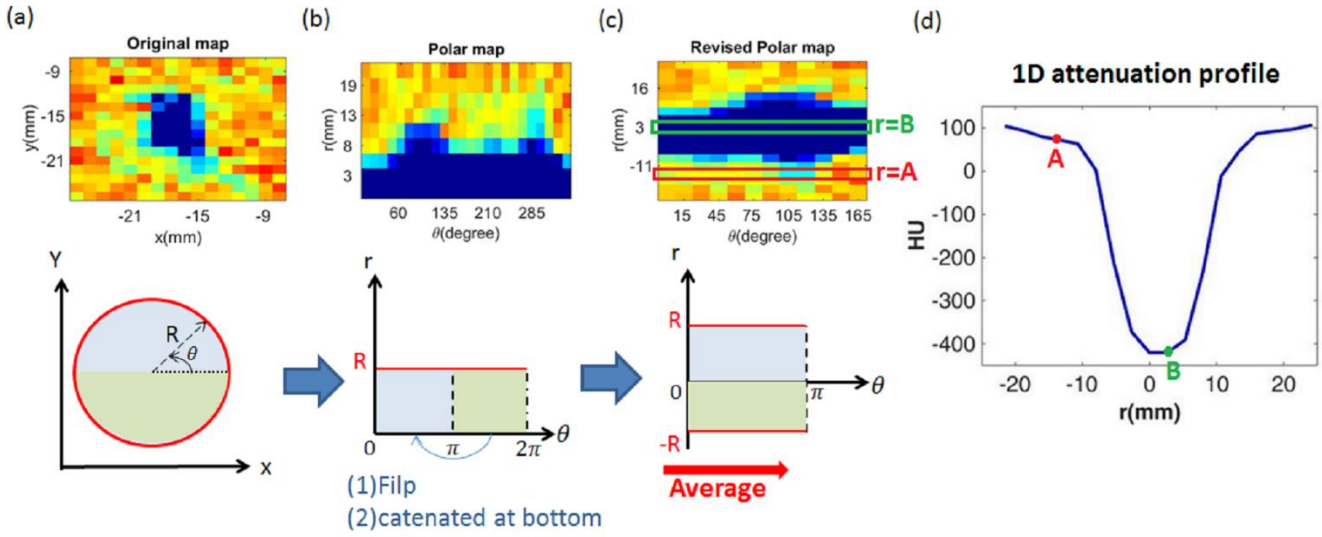

Figure 3.3 Data projection into a polar coordinate system. The upper part of (a) to (c) display the example result at each stage. The original data (a) were first cast into polar coordinates (b). Attenuation was then reformed in "diameter to angle" map (c). All the pixels at each diametric position, like the regions at r =A and r =B in the map, were averaged over the angular domain to produce the 1-D attenuation profile (d).

3.2.3 Post-ablation analysis

Contrast material kinetics were analyzed through changes in the 2D and 1D attenuation maps. Pre-ablation ablation maps were subtracted from post-ablation maps for Group A, B and C. In addition, ablation zone visibility was quantified as the contrast-to-noise ratio (CNR):

$$CNR = \frac{\mu_{liver} - \mu_{abl}}{\sigma_{background}} \tag{3.1}$$

where μ_{abl} is the pixel intensity in the downsampled, cropped slice in each group, μ_{liver} is the mean attenuation of the background liver, and $\sigma_{background}$ is the image noise calculated as the standard deviation of attenuation in the background air.

Each ablation diameter was measured at gross pathology after sectioning the ablation zone along the antenna tract. Three distinct regions were selected for analysis: (1) central ablation zone: pixels less than 5mm from ablation center, (2) peripheral ablation zone: pixels between the central ablation zone and ablation boundary, and (3) background: pixels outside the estimated ablation zone. The mean attenuation and CNR of each region was computed for each sample. The mean and standard error was used to analyze the general effect from ablation and contrast delivery on each region. The unpaired two-sample *t*-test was used to examine statistical significance of attenuation change between pre- and post-ablation data.

3.2.4 Ablation Zone Sharpness Analysis

A post-ablation image with good ablation zone sharpness has two characteristics: (1) a high ablation zone shape similarity between radiological and pathological data, and (2) a high level of attenuation contrast across the ablation boundary [181], [182]. To compare the shape between

radiological and pathological image, the radiological ablation zone was manually segmented slice by slice in each sample. The equivalent circular diameter of each segmentation, which is widely used in morphometric analysis [183], [184], was calculated by the following formula,

$$D = \sqrt{\frac{4A}{\pi}} \tag{3.2}$$

where *A* is the area of the segmentation. The maximal equivalent diameter in each sample was subtracted from the corresponding pathological diameter to represent shape similarity.

The radial attenuation gradient across the post-ablation boundary was also calculated to indicate edge sharpness [185], [186]. The radial gradient was calculated from the horizontal and vertical derivative in pixel attenuation values by the following formula:

$$D_r(i,j) = \left(\frac{x}{r}\right) D_x(i,j) + \left(\frac{y}{r}\right) D_y(i,j) \tag{3.3}$$

where D_x and D_y was approximated by the central difference of statistics along with horizontal and vertical direction:

$$D_x(i,j) \approx \frac{1}{2}\big(f(i+1,j) - f(i-1,j)\big) \tag{3.4}$$

$$D_y(i,j) \approx \frac{1}{2}\big(f(i,j+1) - f(i,j-1)\big) \tag{3.5}$$

and *r* is the distance from (*i*,*j*) to image center. The result was rescaled to actual distance in millimeters so that the boundary gradient is in units of HU/mm. The mean boundary gradient was then compared to background liver by unpaired two-sample t-test, with higher values indicating greater boundary clarity.

3.2.5 Temporal Analysis

To analyze the attenuation variation over time in each group, 1D cross section attenuation profiles were evaluated at each time point. Profiles on specific locations belonging to the central ablation zone (radial distance=3 mm, 5 mm), peripheral ablation zone (radial distance=8 mm, 11 mm; 13 mm and 16 mm for group C) and background (radial distance=13 mm and 16 mm for group A & B, 19 mm and 21 mm) were averaged across samples to elucidate attenuation variation during the entire procedure.

3.3 Results

3.3.1 Post-ablation Analysis

In Group A, attenuation in the central ablation zone decreased from 54.3±8.9 HU (pre-ablation, mean ± standard error of mean) to 3.3±27.2 HU (P = .100). Visual inspection of the CT images showed marked water vaporization in the central zone **(Figure 3.4)**. A smaller change in attenuation was noted in the peripheral ablation zone (54.7±4.9 HU pre compared to 40.3±3.5 HU post; P = .045). The attenuation of background liver was relatively unchanged **(Table 3.1)**. Due to the subtle changes at the ablation periphery, the ablation zone was not highly visible in Group A. The mean CNR over the entire ablation was 1.57±0.73, but this was heavily influenced by large attenuation changes in the central zone (3.73±2.17; **Table 3.2**).

By contrast, attenuation increased from 51.9±4.3 HU pre to 86.6±5.4 HU (P < .001) post in Group B, suggesting that iodinated contrast was drawn into and trapped inside the ablation zone. The background liver attenuation increased even more (50.8±2.8 HU to 115.5±4.5 HU; P<0.0001). Ablations were much more visible in Group B compared to Group A, with an overall CNR of

2.04±0.84 and peripheral CNR of 1.87±0.80 **(Table 3.2).** Similarly, the ablation zone attenuation was 64.5±21.6 HU higher in Group B compared to Group A, again implying that contrast material was trapped during Group B ablations **(Figure 3.5).** The attenuation difference between these two groups was higher near the center than the periphery since the central attenuation decreased more after ablations in Group A **(Table 3.1).**

Group C ablation zones were larger than in Groups A or B. Diameters measured at gross pathology in Groups A, B and C were 23.9±1.2 mm, 22.3±1.8 mm, and 39.3±1.7 mm, respectively **(Table 3.3).** Attenuation decreased in the contrast-laden Group C livers during ablation (140.2±9.9 HU pre compare to 50.4±17.4 HU post; *P* = .002). Anecdotally, substantially greater water vapor was also noted in Group C ablations **(Figure 3.4)**. The greater vapor generation and water expansion also resulted in highest visibility among all groups. However, gas in the central zone provided more to visibility than water expansion in the periphery (overall CNR=3.28±0.88, central CNR=13.19±4.49, peripheral CNR=2.63±0.67).

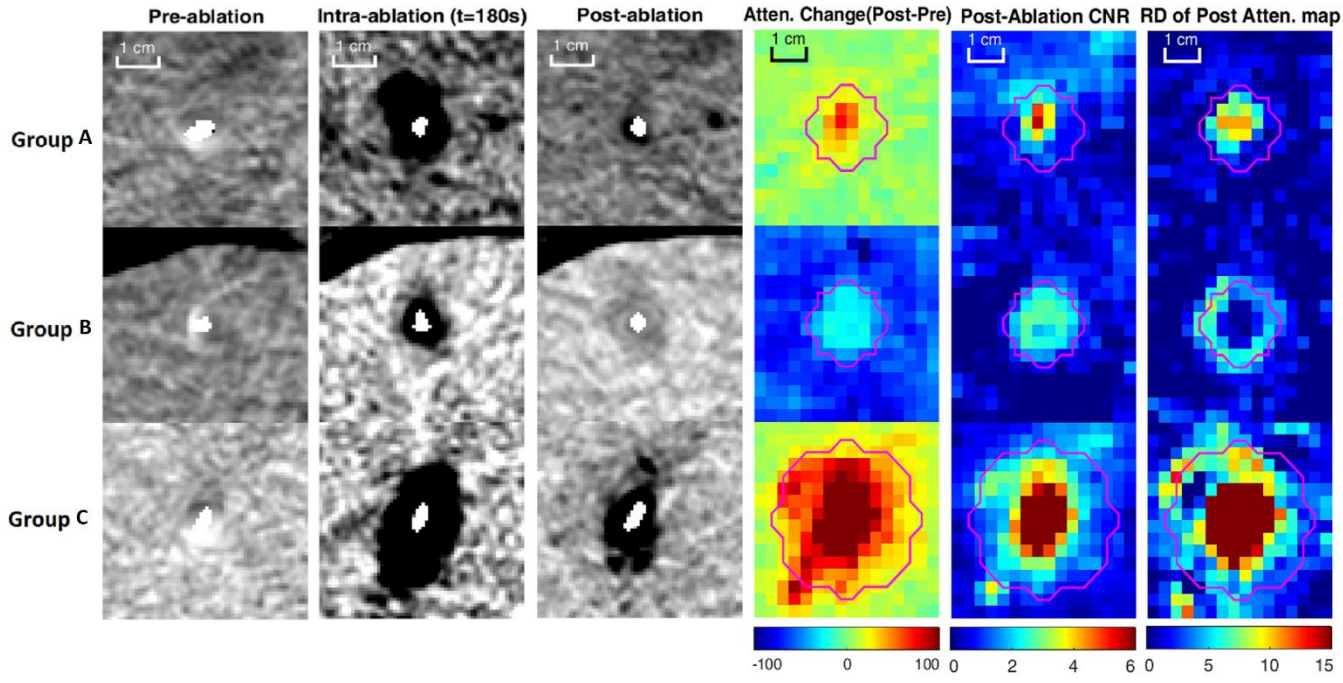

Figure 3.4Example results of pre, intra and post ablation and the mean statistics for each group. Pink line is "observed ablation boundary". The increasing attenuation inside the ablation zone of group B indicated the trapping of iodine material. The high post CNR region correlated well with the observed boundary, and the boundary was salient due to high spatial attenuation contrast to normal liver. Without blood perfusion in group C, the ablation zone was large with more gas region, making contribution to high post CNR and post-attenuation gradient magnitude inside ablation zone. However, no iodine material was trapped inside the region, causing similar attenuation decreased as group A.

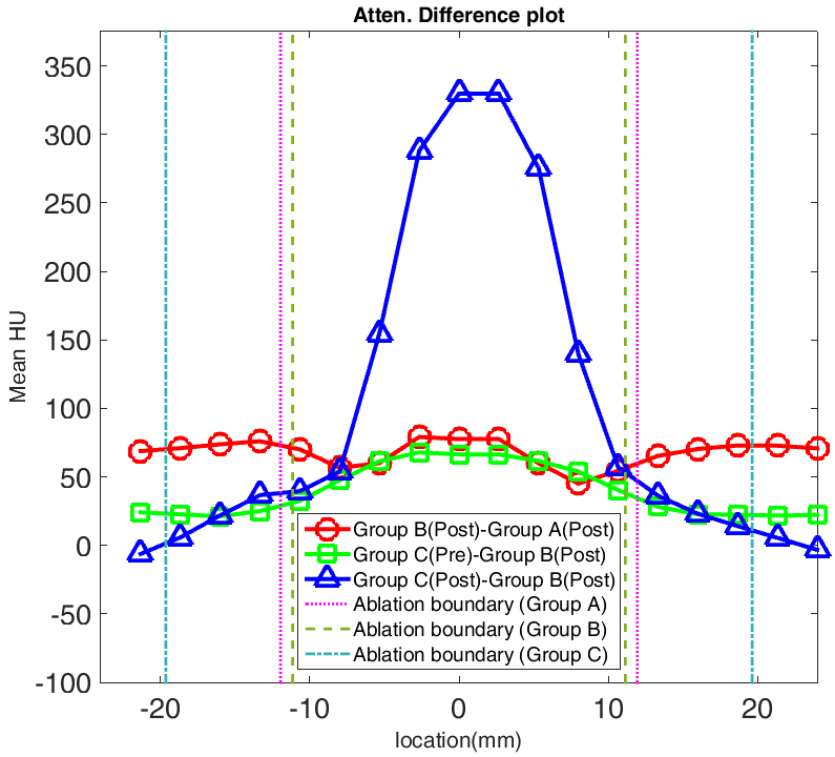

Figure 3.5 Comparison of attenuation profile changes. Positive values for Group B – Group A indicate contrast was trapped inside of the ablation zone. However, the positive difference between Group C pre-ablation (enhanced normal liver) and Group B post-ablation demonstrates that the ablation zone is still hypodense compare to background liver.

Table 3.1 Mean attenuation of central, peripheral, entire ablation zone and background for pre-ablation, post-ablation and difference (Post-Pre). Data provided as mean±standard error. Cen.=Central, Peri.=Peripheral, B.G=Background

	Group A			*Group B*			*Group C*		
	Pre	*Post*	*Diff.*	*Pre*	*Post*	*Diff.*	*Pre*	*Post*	*Diff.*
Cen.	*54.3±8.9*	*3.3±27.2*	*-51.0±26.0*	*53.7±4.7*	*78.4±7.9*	*24.7±8.7*	*143.5±14.3*	*-200.8±80.9*	*-344.2±82.0*

Peri.	*54.7±4.9*	*40.3±3.6*	*-14.3±5.0*	*51.4±4.2*	*89.7±5.2*	*38.3±5.2*	*139.9±9.7*	*74.4±14.2*	*-65.5±10.8*
Entire	*54.7±5.5*	*34.6±7.3*	*-20.1±7.7*	*51.9±4.3*	*86.6±5.4*	*34.7±6.0*	*140.2±9.9*	*57.4±17.4*	*-82.9±14.6*
B.G	*50.5±2.4*	*46.1±2.9*	*-4.4±2.5*	*50.8±2.8*	*115.5±4.5*	*64.7±3.9*	*140.0±10.2*	*122.1±9.9*	*-17.9±2.3*

Table 3.2 Mean CNR of central, peripheral, entire ablation zone and background for pre-ablation, post-ablation. Data provided as mean±standard error.

	Group A		*Group B*		*Group C*	
Region	*Pre*	*Post*	*Pre*	*Post*	*Pre*	*Post*
Central	*0.14±0.78*	*3.73±2.17*	*0.12±0.30*	*2.54±1.04*	*-0.05±0.15*	*13.19±4.49*
Peripheral	*0.15±0.41*	*1.16±0.43*	*0.33±0.27*	*1.87±0.80*	*0.15±0.07*	*2.63±0.67*
Entire	*0.14±0.48*	*1.57±0.73*	*0.28±0.27*	*2.04±0.84*	*0.13±0.06*	*3.28±0.88*
Background	*0.44±0.10*	*0.78±0.33*	*0.41±0.18*	*0.21±0.27*	*0.22±0.15*	*0.92±0.36*

Table 3.3 Mean equivalent diameter and diameter difference of pathological and radiological ablation zone and P-value (in mm) . Data provided as mean±standard error.

Group	*Pathological*	*Radiological*	*Difference*	*P-value*
Group A	*23.9±1.2*	*18.6±0.5*	*-5.3±1.3*	*P<0.01**
Group B	*22.3±1.8*	*22.6±1.1*	*0.3±0.9*	*P=0.89*
Group C	*39.3±1.7*	*32.9±2.1*	*-6.4±2.8*	*P=0.03**

*:Statistical significance

3.3.2 Ablation Zone Sharpness Analysis

In Group A, the post-ablation boundary gradient was small, suggesting that the ablation boundary was barely distinguishable from background liver (0.7±0.4 HU/mm; **Table 3.4**). Due to low contrast between the ablation boundary and background liver, the ablation zone was underestimated on CT (radiological diameter = 18.6 ± 0.5 mm, pathological diameter = 23.9±1.2 mm, $P < .01$; **Table 3.3**).

In comparison with Group A, the post boundary radial derivative in Group B was large enough to distinguish the boundary from the background liver (6.3 ± 1.1 HU/mm, P = 0.001). The mean ablation diameter measured on CT was no different than the diameter measured at pathology (22.6 ± 1.1 mm and 22.3 ± 1.8 mm, respectively; P = .89), suggesting that even though contrast was being trapped in the ablation, the ablation zone could be precisely visualized.

In Group C, the post boundary radial derivative was higher than Group A, but the boundary was still ambiguous with a lower gradient than in Group B (3.9 ± 1.1 HU/mm; P = .46). As a result, the Group C ablation diameters were underestimated compared to diameters measured at pathology (32.9 ± 2.1 mm and 39.3 ± 1.7 mm, respectively; P = .03).

Table 3.4 Mean radial derivative on of ablation boundary (in HU\mm) and P-value. Data provided as mean±standard error of mean

Group	*R.D of Post-attenuation*	*P-value(R.D)*
Group A	*0.7±0.4*	*P=0.56*
Group B	*6.3±1.1*	*P=0.001**
Group C	*3.9±1.1*	*P=0.46*

*:Statistical significance

3.3.3 Temporal analysis

Group A ablation zone attenuation decreased monotonically over time. Attenuation dropped faster and to lower levels near the antenna compared to peripheral locations. Once microwave power was turned off and the ablation process completed, much of the lost attenuation recovered, presumably due to water vapor condensation and temperature declines **(Figure 3.6 and Table 3.5).** Attenuation scarcely changed outside of the ablation region.

Attenuation in Group B also decreased in most regions, but the rate of change slowed after 60-120 s, eventually flattening out at -361 ± 16 HU, -171 ± 13 HU and 22 ± 6 HU at 3mm, 5mm and 8mm from the antenna **(Figure 3.6)**. Attenuation recovered once the ablation ceased, but the final attenuation was greater than the initial value due to trapped contrast material **(Table 3.5)**. At locations outside ablation zone, the attenuation increased with a fixed rate due to continuous contrast infusion, but decreased after the infusion ceased as contrast was filtered from the blood **(Table 3.5).**

The attenuation of Group C ablations also decreased rapidly. The post-ablation attenuation was far beneath the pre-attenuation value due to greater water vapor expansion and a lack of perfusion to mitigate heat transfer. Like Groups A and B, attenuation also recovered once the microwave power was turned off and gas dissipated **(Table 3.5).**

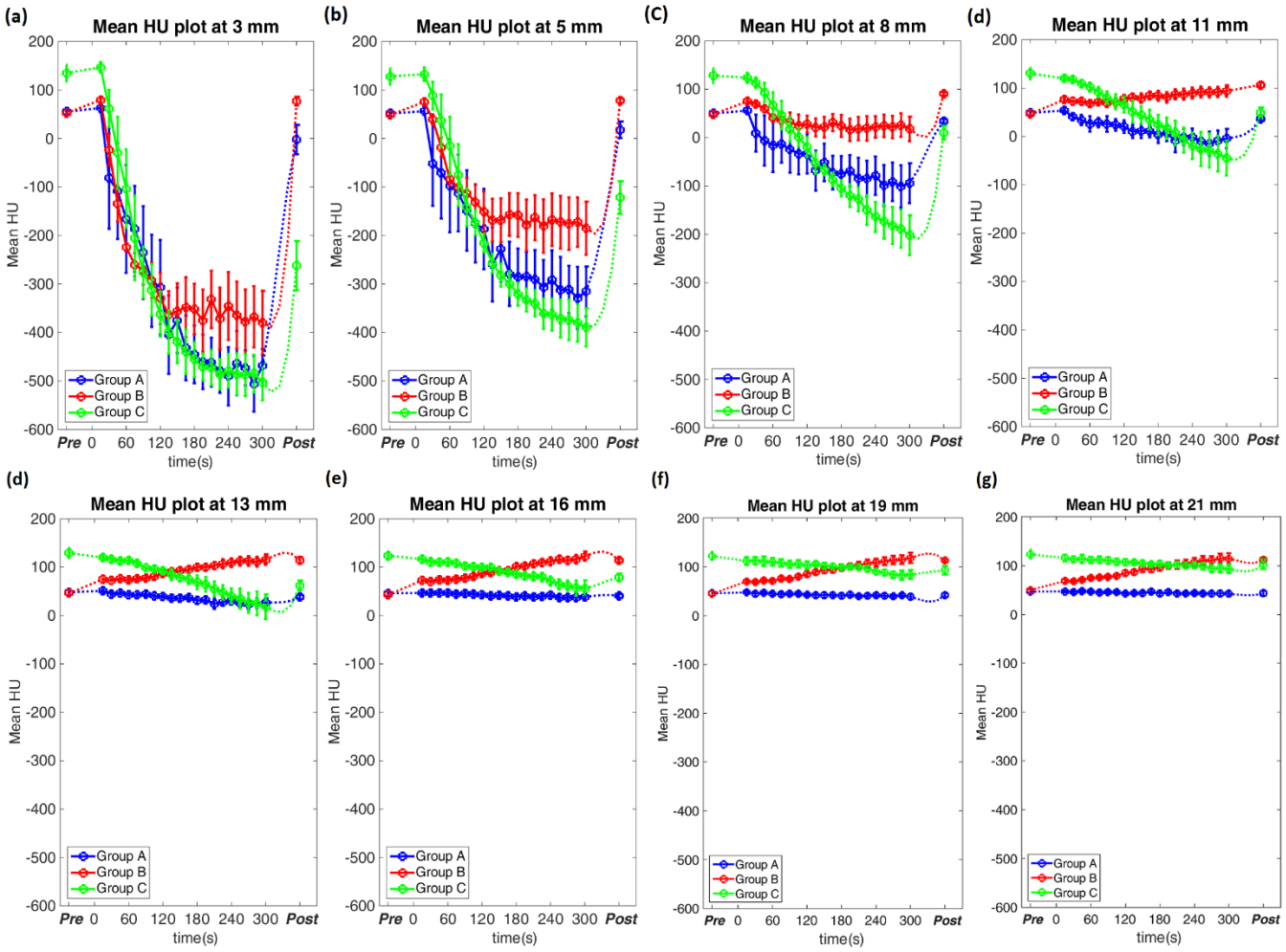

Figure 3.6 Temporal attenuation at different location in each groups. The data was shown as mean attenuation with error bars representing the standard error of mean. While the attenuation decreased over time inside ablation zone in Group A and C, the attenuation in Group B began to slow the decreasing trend at 60 seconds and keep at a certain level at 120 seconds. This suggested that the contrast agent was brought into the region at 60 seconds and trapped after 120 seconds.

Table 3.5 Mean attenuation on specific locations at different stages during ablation procedure. Data provided as mean±standard error of mean. Beg.=Beginning, A.R=After Recovery

	Group A							
Stage	*3mm*	*5mm*	*8mm*	*11mm*	*13mm*	*16mm*	*19mm*	*21mm*
Pre	*54.9±6.9*	*51.5±5.1*	*49.8±4.7*	*48.9±4.3*	*48.0±3.6*	*46.0±3.5*	*45.3±4.3*	*46.5±4.3*
Beg,	*62.9±8.9*	*56.1±7.3*	*55.7±5.4*	*53.5±3.1*	*51.2±2.7*	*46.8±3.7*	*47.9±3.1*	*47.1±1.9*
End	*-468.0±34.0*	*-315.4±51.4*	*-94.2±41.2*	*-4.4±19.9*	*26.8±9.2*	*38.9±4.6*	*38.7±5.5*	*42.4±4.7*

A.R	*-2.2±30.3*	*18.0±17.0*	*33.8±5.0*	*36.3±3.9*	*38.4±4.5*	*40.6±4.3*	*41.8±4.0*	*43.3±4.9*
				Group B				
Stage	*3mm*	*5mm*	*8mm*	*11mm*	*13mm*	*16mm*	*19mm*	*21mm*
Pre	*52.4±5.4*	*48.2±4.0*	*48.4±2.9*	*46.7±3.2*	*46.2±4.1*	*40.1±6.6*	*44.5±6.3*	*49.9±3.5*
Beg,	*79.3±3.3*	*75.5±5.2*	*74.7±3.0*	*75.9±3.3*	*75.6±2.0*	*72.6±2.2*	*70.0±2.9*	*68.5±3.6*
End	*-468.0±34.0*	*-172.3±50.9*	*18.0±25.3*	*94.0±12.0*	*115.9±10.9*	*122.9±9.7*	*118.6±10.8*	*114.5±11.2*
A.R	*76.9±9.1*	*78.0±4.9*	*90.5±4.0*	*106.4±5.6*	*114.3±6.2*	*114.3±4.1*	*112.8±2.5*	*112.1±4.5*
				Group C				
Stage	*3mm*	*5mm*	*8mm*	*11mm*	*13mm*	*16mm*	*19mm*	*21mm*
Pre	*135.0±17.2*	*127.9±17.1*	*128.5±15.7*	*130.3±12.2*	*129.8±11.2*	*124.2±9.3*	*122.2±8.7*	*123.4±9.4*
Beg,	*146.7±10.9*	*132.5±14.1*	*123.5±10.6*	*120.2±5.3*	*119.7±4.8*	*116.6±7.9*	*111.9±8.1*	*115.8±7.0*
End	*-502.5±37.2*	*-389.3±39.2*	*-202.0±41.3*	*-44.5±36.4*	*18.3±25.8*	*56.6±16.4*	*84.3±9.5*	*93.2±9.2*
A.R	*-262.1±50.6*	*-122.0±33.7*	*10.3±13.8*	*49.7±10.2*	*62.5±10.4*	*79.3±7.4*	*92.7±8.8*	*103.1±10.1*

3.4 Discussion

In this study, comparison of attenuation values inside and outside of ablations created with three difference protocols suggests that iodinated contrast material is trapped in the growing zone of thermal coagulation. However, the even greater increasing attenuation of normally perfused liver allows for sufficient attenuation contrast to appreciate the growing ablation and indicate the correct ablation boundary. The very hypodense zone of water vaporization in the central ablation zone also provides a mechanism to monitor ablation zone growth. Therefore, this study demonstrated the feasibility of using iodinated contrast material with temporal CT scanning in real time ablation monitoring.

In the temporal analysis, the rate of attenuation change inside of Group B ablations slowed about 60 seconds into the treatment, and became extremely low after 120 seconds. We hypothesize that this may be due to the presence of iodine in the ablation zone. Pixel intensity is related to a linear combination of attenuation coefficients and densities of the constituent materials [187]. Prior to contrast injection, attenuation was primarily determined by the underlying water, tissue proteins, and lipids. Over the first 60 s of ablation, iodinated contrast was added to the tissue to increase attenuation. As a region coagulated, blood flow ceased and iodine was retained. As heating continued, water was vaporized and the effective attenuation decreased. Once the water vaporization process quenched, the attenuation remained increased compared to Group A due to the continued presence of iodine. Hence, iodine seemed to increase the floor level of attenuation for Group B. Once microwave power was turned off, water vapor condensed and contributed to the sudden increase in attenuation noted in each group, with greater attenuation in Group B due to the presence of iodine. In Group C, the attenuation continuously decreased during ablation, which was opposite to the trend of Group B. This may be due to greater gas generation in the unperfused liver. Blood perfusion introduces a "heat-sink" effect that mitigates heat and mass transfer so greater vaporization would be expected in tissue lacking blood flow [188], [189]. However, this hypothesis would need additional controlled experimentation for confirmation.

Some limitations in the study design exist. First, we used attenuation as an indirect indicator of iodine during ablation. The actual concentration of iodine in the ablated tissue was not measured directly. However, the resulting differences in attenuation provide strong evidence for trapped iodine and keep the analysis focused on the most clinically important metrics of ablation zone visualization. Our imaging-based technique also allowed us to analyze changes temporally, which would not be as feasible with a more direct chemical analysis. Secondly, we investigated the

contrast agent behavior on normal porcine liver. Blood flow is known to be different in pathologic liver and tumor and therefore the changes in attenuation we observed may be different in human liver or tumor [190]. However, changing the tissue type is not likely to alter the primary conclusions of the study.

In conclusion, iodinated contrast delivery during thermal ablation was analyzed by CECT. The results showed that ablating with concurrent contrast delivery could cause some of the contrast material to be trapped in the ablation zone. However, the actual ablation zone was still highly visible on CT. Future studies will emphasize quantifying the amount of trapped iodine and analyzing the imaging technique in human patient populations.

Chapter 4 Ablation Zone Visualization Enhancement by intra-procedural, low-dose Periodic CECT

(Work was published as: Wu P-H, Borden Z, Brace CL. "Ablation zone visualization enhancement by periodic contrast-enhanced computed tomography during microwave ablation" *Medical Physics* 2017;in press)

4.1 Introduction

In chapter 3, we examined the influence of IV contrast material injections on ablation zone visibility. That study only focused on the feasibility of using serial CECT in real-time ablation monitoring from a physiological viewpoint. The contrast study did not address the major obstacle to using serial CT scans: increased radiation and iodinated contrast dosage. The radiation dose accumulated during repetitive CECT scan may have long-term damage on normal parenchyma and induce secondary cancer. High doses of contrast agent used to enhance the contrast between ablation zone and normal parenchyma may result in malfunction of the kidney. While the radiation dose can be decreased by adjusting X-ray tube voltage and current in the CT data acquisition protocol, the number of x-ray photons arriving at the detector may be insufficient to overcome system noise [180], [191]. The resulting noisy images would not be of diagnostic quality. Thus, a balance must be struck between the dose required for sufficient image quality along with post-processing techniques to boost image quality, and reduced dose to minimize radiation exposure during each of the serial CT scans.

Besides low-dose CT noise, high density materials in the ablation applicator (e.g. copper and zirconia) may result in dramatically increased attenuation (called “beam-hardening artifact”) or scattering photons (called “scattered artifact”) and produce the characteristic metal streak artifact (dark and high streak on FBP reconstructed image)[180]. Metal artifact may be more severe in low-dose CT scan due to easily attenuation in low energy x-ray photons, which will obscure the ablation zone. The objective of this aim will study the method to reduce artifacts and enhance ablation zone visualization using in temporal serial, low-dose CT scans, and evaluate the performance compared with pathological ablation zone.

In recent studies, Highly Constrained Backprojection (HYPR) was widely used in improving signal fidelity and reducing image noise during MRI and CT [192], [193]. The summation of time series signals or images will reduce noise and improve the signal strength. In the previous published paper, Brace et al revealed that the time-correlated, enhanced normal parenchyma was enhanced by HYPR. The time-variant, unenhanced ablation zone was, therefore, distinguished from the bright normal liver tissue [194]. Despite the statistics (e.g. signal-to-noise ratio (SNR) and contrast-to-noise ratio) in their study indicating that the image quality and ablation zone visibility after 2 min with HYPR processing, they did not consider the influence on HYPR results from breathing motion within scans. Any movements happening within scans will result in errors in the summation process and generate a mismatch between the displayed ablation zone on image and the real ablation zone. This mistake may cause inaccuracy on ablation zone estimation and lead to misevaluation of treatment. In addition, they did not compare similarity between the radiological and pathological ablation zone to prove the feasibility of visualizing the true ablation zone through HYPR-processed serial CECT imaging.

In this study, we performed the HYPR processing with registration and metal artifact reduction. The analysis of image quality and the visibility and the comparison between HYPR radiological ablation zone and pathological ablation was performed as well to evaluate the feasibility of HYPR.

4.2 Methods

4.2.1 *In-vivo* Ablation Procedure

A total of six microwave ablations were performed in the livers of four female domestic swine (Agricultural Research Station, Arlington, WI) with a median weight of 65 kg (range, 50–70 kg), with a mean of two ablations per animal. The animal was sedated with 7 mg/kg of intramuscular

tiletamine hydrochloride and zolazepam hydrochloride (Telazol; Wyeth, Fort Dodge, IA) and 2.2 mg/kg of xylazine hydrochloride (Xyla-Ject; Phoenix Pharmaceutical, St Joseph, MO). Endotracheal intubation was facilitated by means of 0.05 mg/kg atropine (Phoenix Pharmaceutical), and then anesthesia was induced and maintained the effect with 2% inhaled isoflurane (Halocarbon Laboratories, River Edge, NJ). Once anesthetized, the animal was placed supine on the CT scanner bed (General Electric 750 HD, Waukesha, WI). The liver was surgically exposed before ablation, and up to three triaxial antennas (LK 15; NeuWave Medical Inc., Madison, WI) were visually placed into separate lobes. A 2-3 mm barbed metal hook was placed into the surface of the liver near each antenna to serve as a fiducial marker for co-registration between radiological imaging and gross pathology data. An initial 40ml of iodinated contrast agent (300mg/ml iohexol, GE Healthcare, Waukesha, WI) was injected approximately 1 min before microwave power delivery at 5ml/s. To maintain contrast enhancement during serial CT, 10ml of contrast agent was delivered 1min before each scan at 3ml/s. The ablation was then created by 2.45GHz MW generator (Certus 140 ; NeuWave Medical Inc., Madison, WI) with continuously 100W delivering through each antenna for 10min. The swine were euthanized after ablation and their livers were removed. Each ablation was sliced along the antenna axis to display the largest ablation zone and then photographed for gross pathology to provide a “ground truth” pathological assessment.

4.2.2 Image Processing

Serial abdominal CECT (80 kVp, 100 mAs, 512x512, 1:0.984 helical pitch, 1.25mm slice thickness) was performed at 1 min intervals (total 10 scans) during the ablation. Accumulated radiation dose ($CTDI_{vol}$) was computed for each scan. The initial CT volume was rotated according to the insertion angle of the applicator to ensure slices were perpendicular to applicator.

Subsequent volumes were then co-registered to the first volume by aligning applicators under rigid assumptions.[177] Metal artifacts in each volume were reduced slice by slice by forward projecting each image, replacing the metal attenuation data in the sinogram using sparse interpolation, and then back projecting the result [178]–[180]. HYPR processing was then applied slice by slice according to procedures outlined previously[193]. A brief summary of the steps is provided here. First, a composite image is formed:

$$I_H(x,y,z;t_N) = I_c(x,y,z;t_N) \cdot \frac{I(x,y,z;t_N) * F(x,y)}{I_c(x,y,z;t_N) * F(x,y)} \tag{4.1}$$

where $I(x,y,z;t_N)$ is the slice at the latest time t_N and $I_c(x,y,z;t_N)$ is the composited slice, which is the temporal average of previous and current slices,

$$I_c(x,y,z;t_N) = \frac{1}{N}\sum_{i=1}^{N} I(x,y,z;t_i) \tag{4.2}$$

$F(x,y)$ is a 2D 10x10 pixel uniform square low pass filter (LPF) which was applied on every slice. The symbol "$*$" means 2D convolution. N is total time frames for serial CECT, which was 10 in this study. The final output slice $I_H(x,y,z;t_N)$ was calculated through multiplying the composited slice by the weighting slice to effectively enhance changes introduced in the latest slice **(Figure. 4.1).** All CECT volumes were processed using MATLAB 2015a on Intel Core i7 2.80GHz processor and 8GB memory.

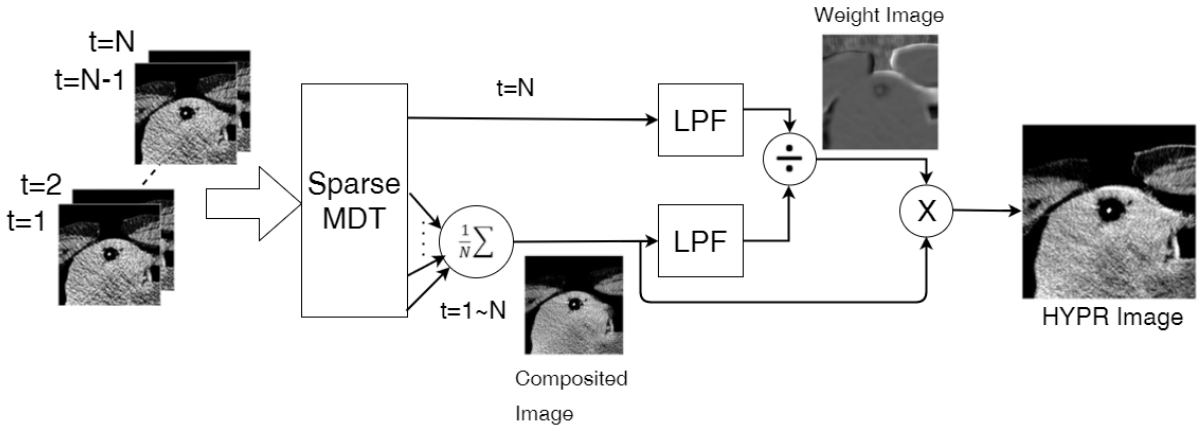

Figure 4.1 Flow diagram of HYPR algorithm (MDT=Metal Artifact Reduction, LPF=Low pass filter)

4.2.3 Statistical Analysis

Six concentric regions of interest (ROIs) with approximately 3 mm thickness were selected around the applicator from six slices in the central ablation at each time point **(Figure 4.2)**. The signal to noise ratio (SNR) and contrast to noise ratio (CNR) of each ROI, which quantified the image quality and visibility of ablation zone, respectively, were calculated:

$$SNR = \frac{\mu_{abl}}{\sigma_{background}} \tag{4.3}$$

$$CNR = \frac{\mu_{liver} - \mu_{abl}}{\sigma_{background}} \tag{4.4}$$

where μ_{abl} is the weighted average attenuation with respect to each ROI inside ablation zone by the following formula,

$$\mu_{abl} = \frac{\sum_{i=1}^{6} A_i \mu_i}{\sum_{i=1}^{6} A_i} \tag{4.5}$$

A_i is the area of i-th ring ROI, μ_i is the average attenuation of i-th ring ROI, μ_{liver} is the mean attenuation of the background liver extracted from predefine ROI, which was 15x15 pixel square and manually located on the liver region without overlapping ablation zone, air or other organs (eg. gallbladder), on each selected slice at each time point. $\sigma_{background}$ is the image noise calculated as the standard deviation of attenuation in the background air. Mean and standard error of SNR and CNR were calculated across six separate samples to represent the general temporal variation during the ablation procedure. At each time frame, SNR and CNR in unprocessed and HYPR processed data were compared by two-sample t-tests.

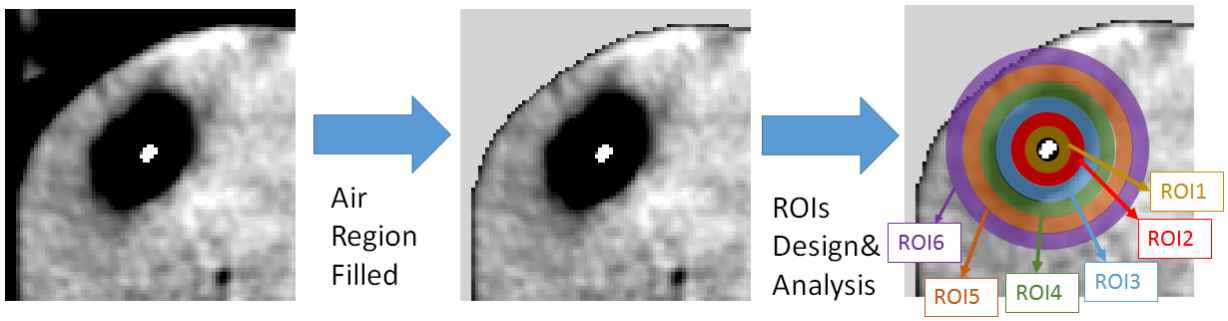

Figure 4.2 Flow chart of pre-processing and design of predefined ROI of ablation zone, which fully covered of the real ablation zone (black and grey region around the applicator)

4.2.4 Ablation zone Analysis

Unprocessed and HYPR processed CT ablation data were created by virtually slicing the volume along the antenna.[195] In brief, the initial virtual slicing plane was generated by the vector which acquired from rotating the normal vector of xz-plane according to the angles of applicator. This initial plane was then rotated along the applicator and shift along with the direction of normal vector, if needed, to acquire the largest ablation zone in CT volume **(Figure 4.3).**

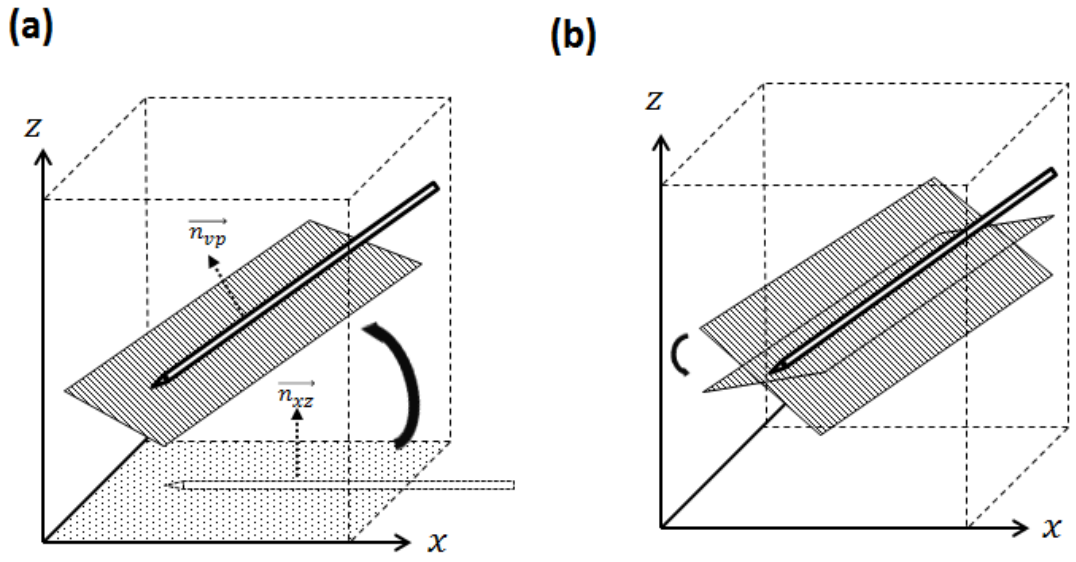

Figure 4.3 The schematic of virtual slicing (a) the generation of normal vector of initial virtual slicing plane. (b) the initial virtual slicing plane was then rotated to acquire the largest

ablation zone in the volume. ($\overrightarrow{n_{xy}}$: the normal vector of xz-plane; $\overrightarrow{n_{vp}}$: the normal vector of initial virtual slicing plane)

Gross pathology was co-registered and rescaled to the radiological virtual slice from the last time point according to the location and length of the antenna and a metallic fiducial visible on each sample image. Three independent observers (3-5 years research experience in thermal ablation each) manually segmented the ablation zone on the raw and HYPR processed virtual slices and gross pathology by delineating along the sharp transition of color or attenuation using ImageJ (National Institutes of Health). All six ablation zones on both radiological and pathological images were measured by each observer. Dice's coefficient was used to quantify similarity between CT images and gross pathology, and to examine similarity between observers [196]

$$DICE = \frac{2J}{1+J} \tag{4.6}$$

where J is a Jaccard index. For radiological-pathological comparison,

$$J_{path-rad} = \frac{A_{path} \cap A_{rad}}{A_{path} \cup A_{rad}} \tag{4.7}$$

where A_{path} and A_{rad} were the pathological and radiological ablation segmentation masks, for a given observer. Similarity between radiology and pathology were then evaluated from the mean and standard deviation of the Dice coefficients from all observers. To evaluate intra-observer agreement,

$$J_{intra} = \frac{A_1 \cap A_2 \cap A_3}{A_1 \cup A_2 \cup A_3} \tag{4.8}$$

where A_n was the segmentation mask generated by the n-th observer for radiological images. Agreement between observers was characterized by the mean and standard deviation of this Dice coefficient. A paired-sample *t*-test was performed using each set of Dice coefficients to compare

radiological-pathological agreement and intra-observer variability between unprocessed and HYPR-processed CT data.

Long and short ablation dimensions were delineated by straight lines passing through the ablation center. The correlation between measurements made at CT and gross pathology were quantified by Pearson's coefficient. The intra-observer agreement of measurements for gross pathology, original CT and HYPR images was quantified by averaging relative standard deviation (RSD), which is the ratio of standard deviation to the mean, among all samples. The mean and standard deviation of RSD were used to analyze the reliability of measurement. The paired-sample T-test of RSD between radiological images and gross pathology was used to analyze the reproducibility of measurement, which was highly related to the visibility of ablation zone displayed on original CT and HYPR images. The absolute difference (A.D.) and relative difference (R.D.) of measurements between radiological and pathological images were used to quantify the shape difference of ablation zone by the following formula:

$$A.D. = \left|M_{rad} - M_{path}\right| \tag{4.9}$$

$$R.D. = \frac{A.D.}{M_{path}} \tag{4.10}$$

Where M_{path} and M_{rad} are the pathological and radiological measurements.

4.3 Results

4.3.1 Radiation Dose and Processing Time

$CTDI_{vol}$ was a maximum of 1.49 mGy for each intraprocedural scan. Total radiation dose per procedure was under 14.9 mGy, which is comparable to a typical contrast-enhanced abdominal

exam. Average time to process a CECT volume, including image registration and HYPR processing, was 9.2 s (registration: 7.5 s; HYPR: 1.7 s).

4.3.2 Statistical analysis

The image quality of HYPR-processed ablation zones increased significantly after two time frames and remained about two times greater than unprocessed data **(Figure 4.4(a))**. Differences in SNR were statistically significant between groups. Ablation zones were about twice as visible, as measured by CNR, in HYPR processed images compared to unprocessed imaging after about four minutes of ablation **(Figure 4.4(b))**.

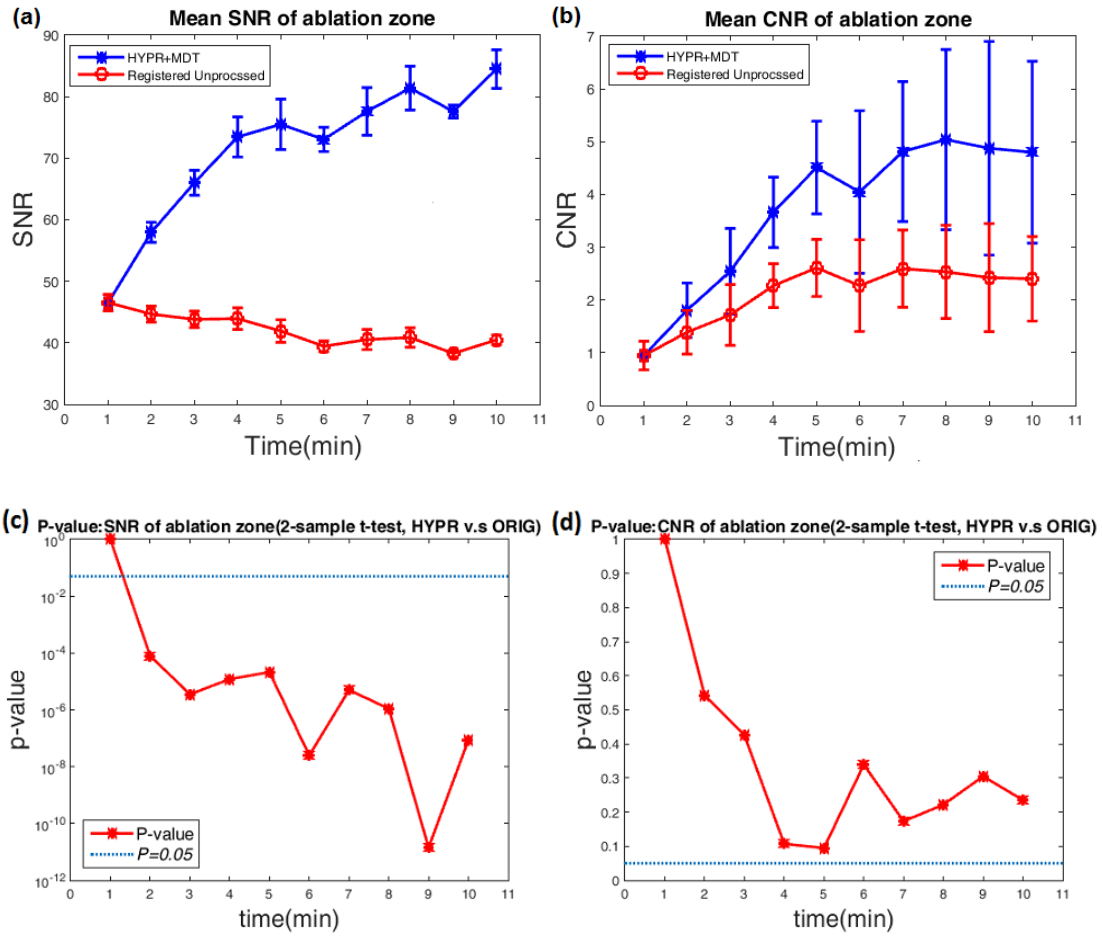

Figure 4.4 Statistical analysis of HYPR. Mean temporal (a) SNR and (b) CNR and the temporal P-value for (c) SNR (in log_{10}-scale) and (d) CNR. Plots for mean measurement showed as "Mean±Standard error".

4.3.3 Ablation Zone Similarity analysis

In CT images from the final time frame, attenuation near the ablation border was decreased by thermal expansion of tissue water [85], [197]. However, increased noise in unprocessed low-dose images made the ablation boundary more ambiguous **(Figure 4.5)**. Compared to unprocessed images, HYPR-processed images preserved the central vapor region and enhanced visualization of the coagulation region near the border, making the ablation boundary more visible **(Figure 4.5)**. Ablation zones segmented from HYPR-processed images were more similar to gross pathology compared those segmented from unprocessed CT images (path-rad similarity: HYPR = 0.81 ± 0.03, Unprocessed = 0.72 ± 0.05; P = 0.06; **Table 4.1**). In addition, there was greater consistency of segmentation among observers from HYPR-processed images compared to unprocessed images (intra-observer similarity: HYPR = 0.79 ± 0.06, Unprocessed = 0.70 ± 0.16; P = 0.17; **Table 4.1**).

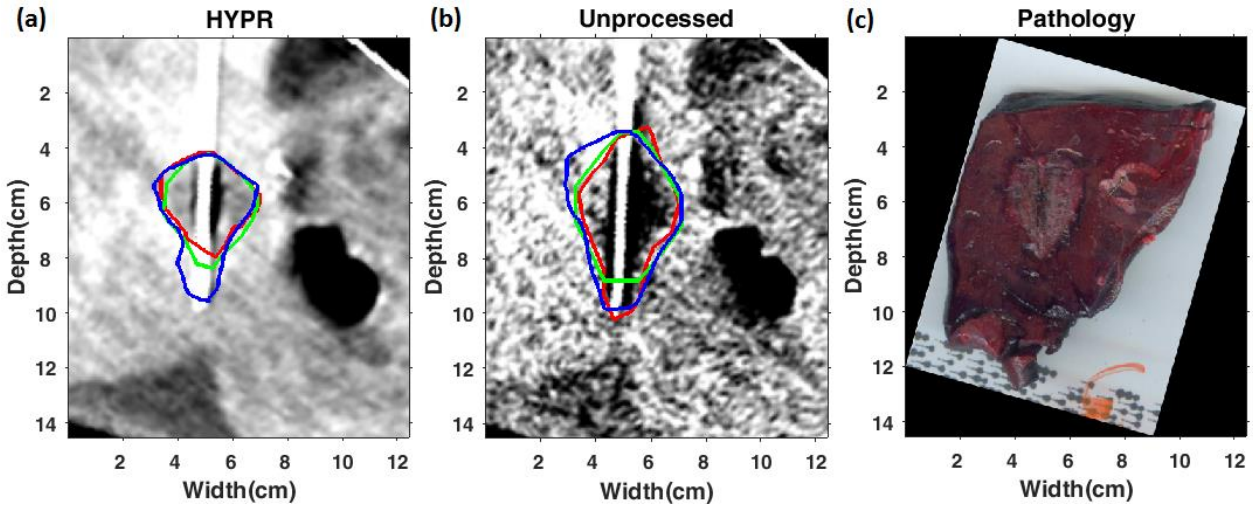

Figure 4.5 Example result of manual segmentation on HYPR and unprocessed data. (a) HYPR with high similarity of segmentation between observers. (b) unprocessed data with ambiguous

ablation zone segmentation, (c)gross pathology.

Table 4.1 Similarity of ablation zone between radiological and pathological image. Data provided as mean±standard deviation.

	Path. v.s Rad.			*Intra-observer*		
	Mean DICE coefficient	*Minimum DICE coefficient*	*Maximum DICE coefficient*	*Mean DICE coefficient*	*Minimum DICE coefficient*	*Maximum DICE coefficient*
Unprocessed	0.72±0.05	0.53	0.86	0.70±0.16	0.41	0.82
HYPR	0.81±0.03	0.73	0.89	0.79±0.06	0.73	0.88

4.3.4 Measurement Variability Analysis

The mean relative pathological-radiological difference in areas which were segmented by multiple observers from HYPR-processed images was significantly lower than unprocessed images (HYPR=13.1 ± 5.6%, unprocessed=37.5 ± 6.0%; P = 0.003; **Table 4.2**). A similar trend was noted in diameter measurements, though with a smaller pathological-radiological difference in the long axis (long axis: HYPR = 9.7 ± 4.2%, unprocessed=17.7 ± 2.8%; P = 0.10; short axis: HYPR = 15.2 ± 2.8 %, unprocessed = 28.9 ± 5.4%; P = 0.05; **Table 4.2**). These results suggest that HYPR-processed images provided more reliable detection of the ablation zone dimensions than unprocessed images.

Table 4.2 Measurement of difference between radiological and pathological image. Data provided as mean±standard deviation. Unproc.= Unprocessed.

		Absolute Difference (cm or cm^2)			*Relative Difference (%)*		
		Mean	*Maximum*	*Minimum*	*Mean*	*Maximum*	*Minimum*
Unproc	Area	6.09±1.44	17.30	0.15	67.0±24.3	167.8	0.9
	LA	1.18±0.31	3.11	0.05	23.5±7.4	84.8	0.7
	SA	1.07±0.25	2.18	0.16	44.0±18.7	131.3	5.8
HYPR	Area	1.84±0.61	4.75	0.02	16.7±11.3	69.6	0.2
	LA	0.64±0.22	1.72	<0.01	11.1±6.6	40.4	$<10^{-3}$
	SA	0.50±0.14	1.02	0	18.1±3.8	39.6	0

4.3.5 Dimension and Area Correlation Analysis

Ablation zones segmented from both HYPR-processed and unprocessed images were highly correlated to gross pathology **(Table 4.3)**. HYPR provided a greater correlation between imaging and pathology in terms of ablation area **(Figure 4.6(a)).** The correlation of short axis length on both images relative to pathology was also high **(Figure 4.6(c))**, but the correlation coefficient of the long axis length was higher on HYPR images than unprocessed images **(Figure 4.6(b))**. This suggests that ablation length was the major difference between unprocessed images and gross pathology.

In looking at agreement between observers, RSDs of all measurements from HYPR images were closer to those of gross pathology compared to unprocessed images **(Table 4.4)**. In essence, the human error in measurement for HYPR images was similar to that of the

ground truth: gross pathology. Greater error was noted when segmenting unprocessed images.

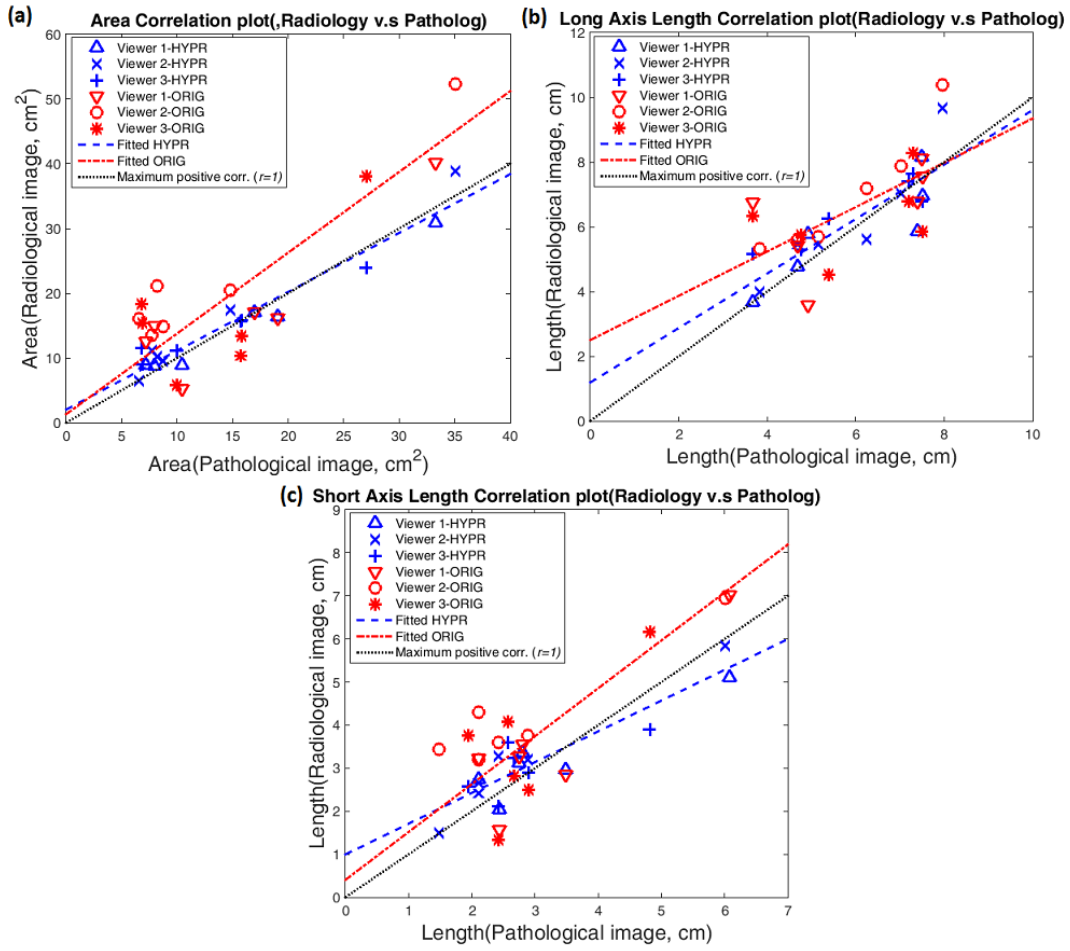

Figure 4.6 Path-rad correlation of (a) area, (b) long axis and (c) short axis for HYPR and unprocessed data. Fit and correlation metrics are noted in Table 4.3.

Table 4.3 Pathological- radiological correlation coefficients of before and after HYPR. LA=Long Axis, SA=Short Axis.

	Unprocessed			*HYPR*		
	Area	*LA*	*SA*	*Area*	*LA*	*SA*
Coefficient	0.94	0.73	0.95	0.99	0.90	0.92
R^2	0.89	0.53	0.91	0.99	0.82	0.85
P	0.005	0.101	0.003	$< 10^{-4}$	0.013	0.009

Table 4.4 Measurement of relative standard deviation. Data provided as mean±standard deviation. Unproc.= Unprocessed, LA=Long Axis, SA=Short Axis.

	Path	*Rad-HYPR*	*Rad-Unproc.*	*P-value (Rad-HYPR v.s Path)*	*P-value (Rad-Unproc. v.s Path)*
Area	0.17±0.10	0.18±0.08	0.27±0.17	0.78	0.21
LA	0.04±0.03	0.10±0.08	0.12±0.06	0.08	0.04
SA	0.13±0.09	0.10±0.06	0.20±0.18	0.32	0.22

4.4 Discussion

In this study, we investigated the feasibility of using serial low-dose CECT with HYPR processing to monitor growing microwave ablations. Analysis of image quality metrics SNR and CNR indicated that HYPR processing improves image quality and enhances visualization of the ablation zone **(Figure 4.4)**. Correlation analysis suggested that the dimension and shape of ablation zones extracted from the final CECT-HYPR images were highly correlated with gross pathology, and CECT-HYPR data provided greater ablation clarity compared to unprocessed images **(Figure 4.6; Table 4.3)**. The time of whole processing with a single volume, including image registration and HYPR processing, was only 9.2 s and less than the minimal time interval of CECT scan (15 s), which ensured the processing can be completed before the next scanning. Therefore, this study demonstrated the feasibility of using low-dose CECT to perform real-time ablation monitoring.

HYPR processing involves two important parts to improve image quality and enhance visualization of the ablation zone: (1) compositing and (2) weighting. The composited slice, which is average of images at previous time frames, can reduce random noise[193]. In addition, averaging images at previous time frames can also accumulate the enhancing effects from continuous contrast agent delivery on normal liver[194]. Therefore, contrast between the ablation zone and background increases, making the ablation zone more visible with each new set of CT images. The weighting

slice, which is the ratio between the filtered current and composited slices, augments changes that have occurred in the current time frame. Multiplying the composited and weighting slices together preserves current geometric information including the shape of ablation zone at current time frame, which could make enhanced image truly display current ablation zone. Hence, the whole HYPR procedure could enhance and truly visualize current ablation zone.

Ablation areas measured from unprocessed CECT images tended to overestimate areas from gross pathology **(Figure 4.6)**, which supports prior studies.[188], [198] Hyperthermia induced in the ablation periphery can cause water expansion, and gas produced in the central ablation region will expand into the periphery. Both effects would be expected to lower x-ray attenuation slightly, though potentially not enough to be discernable depending on local image noise. Compared to unprocessed data, the linear regression of CECT-HYPR has less overestimation of the area measured at gross pathology, demonstrating the ability of HYPR to compensate for increased image noise. The fitted line also demonstrated that the CECT-HYPR area matched well with gross pathology when ablation dimension was less than $25cm^2$, which includes most ablations produced with less than 100 W [199]. Imaging performed during ablation at higher powers and longer treatment times may not provide the same correlation to gross pathology. The 5 mm error in HYPR-processed diameter measurements is within the desired ablation safety margin, which is 5 to 10 mm circumferentially depending on tumor type [92]. In addition, HYPR-processed images led to greater agreement (ie, less variability) between observers than unprocessed images.

Similarity metrics and correlation between pathological and radiological images indicated that the ablation zone visualized from HYPR-processed images is more similar to gross pathology than prior studies **(Figure 4.6; Table 4.1, 4.2 and 4.3)**. For example, DeWall *et al.* analyzed images obtained with shear wave velocity (SWV) during microwave ablation in *ex vivo* bovine liver.[102]

Mean Dice's coefficients between images and gross pathology ranged from 0.74-0.77, with Pearson coefficients of 0.54-0.80. These values are all lower than our investigation from CECT-HYPR images **(Table 4.1 and 4.3)**. Considering the single image plane limit in ultrasound imaging, these results suggested that HYPR processing on CECT volume could be more helpful to visualize the complete ablation volume.

Several weaknesses and limitations in data processing and analysis exist. First, rigid assumptions were used for registration based on the assumption that breathing only causes applicator to shift and rotate during ablation. Abdominal structures or the applicator may elastically deform during breathing; however, preliminary analysis of the applicator suggested minimal deformation leading to registration errors of around 1 mm. Even with potential errors, the analysis in our study still suggested that HYPR could improve the visualization of ablation zones. Our results could be the baseline to further study on using different registration methods with the HYPR algorithm. Secondly, we only performed pathology-radiology correlation analysis and similarity measurements on the data from the last time frame as this was the closest point to when gross pathology was obtained. While we cannot confirm similar correlation for all time points, the temporal trends of ablation growth we observed were monotonically increasing during each procedure. The same increase is expected regardless of the treatment time and power delivery[199]–[202].

In conclusion, we performed HYPR processing on time-series CECT volume during ablation procedure. The results showed that HYPR processing could improve the image quality and enhance visualization of ablation zone, leading to more consistently manual segmentation by observers. The segmented HYPR ablation lesion was more similar to gross pathology, suggesting that HYPR image could display more accurate information about ablation lesion. Future studies

will focus on analyzing the amount of radiation dose reduction that HYPR algorithm could tolerate to improve ablation zone visualization. Another direction of future studies will be potentially application for evaluating efficacy of ablation treatment.

Chapter 5 Auto-segmentation of Ablation Zone on Periodic CECT images

5.1 Introduction

Evaluation of the treatment zone relative to the initial tumor is a crucial step in thermal ablation. Without this step, we will be unable to determine whether the treatment is successful. The most common way to evaluate the efficacy of thermal ablation is the information of ablation lesion such as size or geometry. To have a successful treatment and avoid tumor recurrence, the ablation zone must encompass the entire tumor, and extend into a peripheral margin around the tumor of at least 5-10mm depending on the tumor type and index size. Since any errors in evaluation could influence the treatment outcome, a reliable method of ablation lesion segmentation in CECT image is desired to assist radiologists in post-ablation treatment analysis.

Currently, the most common method to segment ablation zones is to manually delineate the high contrast region surrounding the applicator in CECT. However, manually delineation is not feasible during a real-time monitoring protocol. In addition, manually delineation highly depends on observers' experience, leading to inconsistent results of ablation volume estimation. Therefore, an automatic segmentation method for ablation zone is needed to immediately discern the ablation zone in real-time serial CECT.

Rempp et al. attempted to detect ablation lesion by temperature thresholding. In their method, MR-thermometry was performed during radiofrequency ablation, and the temperature mapping was thresholded by 60^{o}C based on the previous experimental results. The region with temperature higher than 60^{o}C was considered as ablation zone [203], [204]. While CT temperature mapping is feasible based on temperature-dependent changes in attenuation [144], [205], [206], the ability to segment the ablation zone based solely on temperature-induced changes has been inconsistent, which may mislead the evaluation of treatment. Passera et al. attempted to apply live-wire method on ablation zone segmentation [207], but the requirement of pre-selecting the target region

hindered it from using in real time CECT scan. Lazebnik et al. tried to automatically segment the ablation zone base on pre-designed model [208]. However, the training data was collected from manual segmentation, which may create a bias on the results. Therefore, methods to automatically segment the ablation lesion based on the information from immediate CECT scan is still needed to facilitate real-time ablation monitoring.

Fuzzy C-mean clustering (FCM) is widely used in object segmentation. Recently, several research groups attempt to segment lesion or tumor on medical image combined with texture analysis and FCM. Kakar et al. used Gabor filter to extract texture feature and then applied FCM to segment lung lesion from CT scan [209]. Bhide et al utilized FCM to cluster pixels with same grayscale value in order to detect brain tumor region on MRI scan [210]. Other research groups applied FCM or its improved version directly on liver CT scan to segment lesion or tumor [211], [212]. In this study, we will perform similar methods to automatically segment the ablation zone in time series CECT images without any user's interactive behavior.

5.2 Materials and methods

5.2.1 *In-vivo* Ablation procedure

Microwave ablations were created in the livers of six swine using a 2.45 GHz microwave generator (Certus 140 ; NeuWave Medical Inc., Madison, WI) and triaxial antenna (LK 15; NeuWave Medical Inc., Madison, WI). Three different protocols of power, duration and contrast material delivery were used for each animal: (A) 100W ablation for 10 minutes with intra-procedural contrast agent delivery, (B) 100W ablation for 5 minutes with intra-procedural contrast agent delivery, and (C) 100W ablation for 5 minutes without contrast agent delivery. For contrast agent delivery, a 40 ml bolus of iodinated contrast (300 mg/ml iohexol; GE Healthcare, Waukesha, WI) was injected 1 min before ablation and then contrast was infused continuously at 0.3 ml/s to

maintain a similar level of enhancement in the perfused liver during the procedure. All the intra-procedural CT scans, whether with contrast material delivery or not, were performed using a low-dose protocol (for 10 min ablation: 1.25 mm thickness, 80 kVp, 100 mA; GE 750 HDCT; for 5 min ablation: 0.625 mm thickness, 80 kVp, 80 mA; GE 750 HDCT). The swine were euthanized after ablation and their livers were removed. Each ablation was sliced along the antenna axis to display the largest ablation zone and then photographed for gross pathology to provide a "ground truth" pathological assessment. Ten CT scans were collected in each CT image series. A total of 12 ablations, eight with CECT scanning and four with CT scanning, were performed.

5.2.2 Pre-processing and feature extraction

All CT volumes in each series were co-registered to the initial volume by rotating according to the insertion angle of the applicator under rigid assumptions in order to ensure slices were perpendicular to applicator [177]. Metal artifacts in each volume were reduced slice by slice by forward projecting each image, replacing the metal attenuation data in the sinogram using sparse interpolation, and then back projecting the result [178]–[180]. HYPR processing was then applied slice by slice according to procedures outlined previously [193]. Each slice in the processed CT volume was cropped as 64 to 64 pixels over the central ablation. First-order and second-order radial attenuation gradients were calculated to highlight regions with large variations and rates of attenuation change, which was hypothesized to comprise the edge of the ablation zone **(Figure 5.1)**,

$$D_r(i,j) = \left(\frac{x}{r}\right) D_x(i,j) + \left(\frac{y}{r}\right) D_y(i,j) \tag{5.1}$$

$$D_r^2(i,j) = D_r(D_r(i,j)) \tag{5.2}$$

where D_x and D_y was approximated by the central difference of statistics along with horizontal and vertical direction mentioned in previous chapters.

The local mean and local standard deviation of each pixels on HYPRed CT image, first-order and second order radial attenuation gradient image by the following formula [213],

$$\mu_{local}(i,j) = \frac{\sum_{k=-N}^{N}\sum_{l=-N}^{N} I(i-k,j-l)}{(2N+1)^2} \tag{5.3}$$

$$\sigma_{local}(i,j) = \sqrt{\frac{\sum_{k=-N}^{N}\sum_{l=-N}^{N}(I(i-k,j-l)-\mu_{local}(x,y))^2}{(2N+1)^2}} \tag{5.4}$$

Where *N* is the window size of neighbor pixels included in the square ROI. Besides first-order statistic feature, normalized fractional brownian feature (NBF) was performed on HYPR-processed CT images by the method outlined previously since it has ability to discriminate low-intensity from high-intensity background [214]. Each feature was performed with various sizes of ROI **(Table 5.1)**. To enhance the feature on the pixels near the ablation boundary, all the features were averaged along with window sizes.

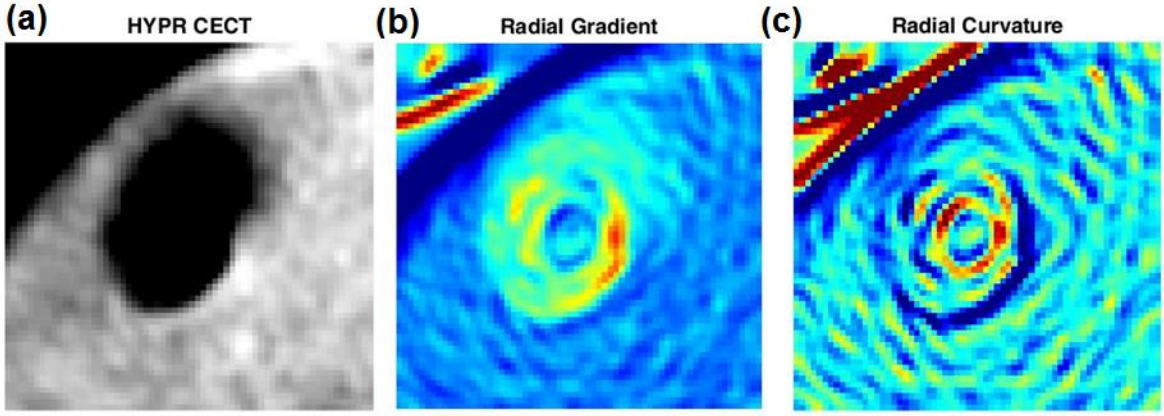

Figure 5.1 Example of HYPR and gradiant image : (a) HYPR image (b) Radial Gradient (First-order Radial gradient) and (c) Radial Curvature (Second-order Radial gradient)

Table 5.1 Window Size for image features on each image

	Window Size (HYPR image)	Window Size (First-order radial gradient)	Window Size (Second-order radial gradient)
Local Mean	3x3 ~ 15x15	3x3 ~ 15x15	3x3 ~ 11x11
Local STD	3x3 ~ 11x11	3x3 ~ 11x11	3x3 ~ 11x11
NBF	11	X	X

5.2.3 Liver and Ablation zone Segmentation

Since the ablation zone is located in liver tissue, the liver region was first segmented by a region-growing method mentioned previously [215]. In brief, the seed pixel inside the region was selected. At each iteration, the region was grown from all pixels including seed inside current segmented region by adding neighbor pixels which satisfy the requirement of similarity,

$$|I(i,j) - \bar{I}| < T \tag{5.5}$$

Where $I(i,j)$ is intensity of neighbor pixel, $\bar{I}$ is average intensity of current segmented region and T is the threshold to examine the similarity. In this study, T was set as 300 HU and the seed pixel was selected automatically as the center of the cropped volume. For each slice, only the pixels inside the liver region were used in the ablation zone segmentation. The intensities of all image features were assigned to corresponding pixels. These pixels were then clustered by the fuzzy C-mean clustering method (FCM) [216]. The basic idea of FCM is to assign "membership" to each pixel with respect to each cluster centroid based on the distance between that pixel and cluster centroid. The whole question could be formed as optimization problem,

$$\hat{\boldsymbol{c}}=\underset{\boldsymbol{c}}{\operatorname{argmin}} J_m(\boldsymbol{c}) \tag{5.6}$$

$$J_m(\boldsymbol{c}) = \sum_{i=1}^{D}\sum_{j=1}^{N} {\mu_{ij}}^m \left\|x_i - c_j\right\| \tag{5.7}$$

Where c_j is the centroid of j-th cluster. x_i is i-th pixel inside the region, and μ_{ij} is the membership level of i-th pixel belonging to j-th cluster. At each location, c_j and μ_{ij} were updated by the following formula until convergence.

$$c_j = \frac{\sum_{i=1}^{D} {\mu_{ij}}^m x_i}{\sum_{i=1}^{D} {\mu_{ij}}^m} \tag{5.8}$$

$$\mu_{ij} = \frac{1}{\sum_{k=1}^{N}\left(\frac{\left\|x_i - c_j\right\|}{\left\|x_i - c_k\right\|}\right)^{\frac{2}{m-1}}} \tag{5.9}$$

The cluster i-th pixel belonging to could be acquired by,

$$\hat{j} = \max_{j} \mu_{ij} \tag{5.10}$$

In this study, the total number of clusters was set as 3, which was meant that there were three clusters for gas region, transition region and untreated region. To segment the ablation zone, the cluster with highest attenuation was removed.

5.2.4 Ablation Volume Refinement

Even used FCM in segmentation and selected regions by examining the attenuation of each cluster, there were few pixels with incorrect segmentation. To remove those pixels, some refinement was required. First of all, the whole ablation volume mask was given cyclic morphological opening [217]. In brief, the cyclic morphological processing is to perform classic morphological processing with rectangular structure on log-polar coordinate since the rectangular structure in log-polar coordinate is equal the fan structure on Cartesian coordinate, which is beneficial to deal with large objects close to the periphery **(Figure 5.2, 5.3)**.

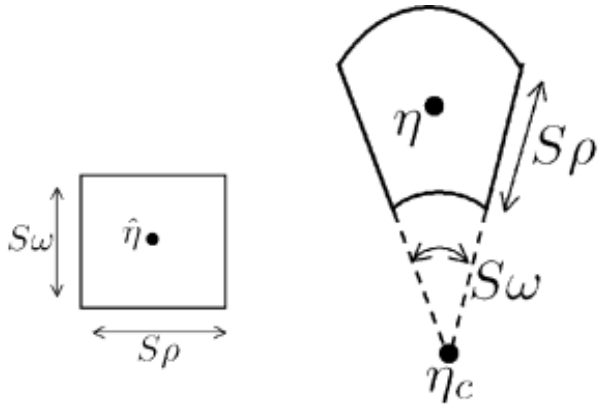

Figure 5.2 Conversion of rectangular structure between log-polar (left) and Cartesian coordinate (right)

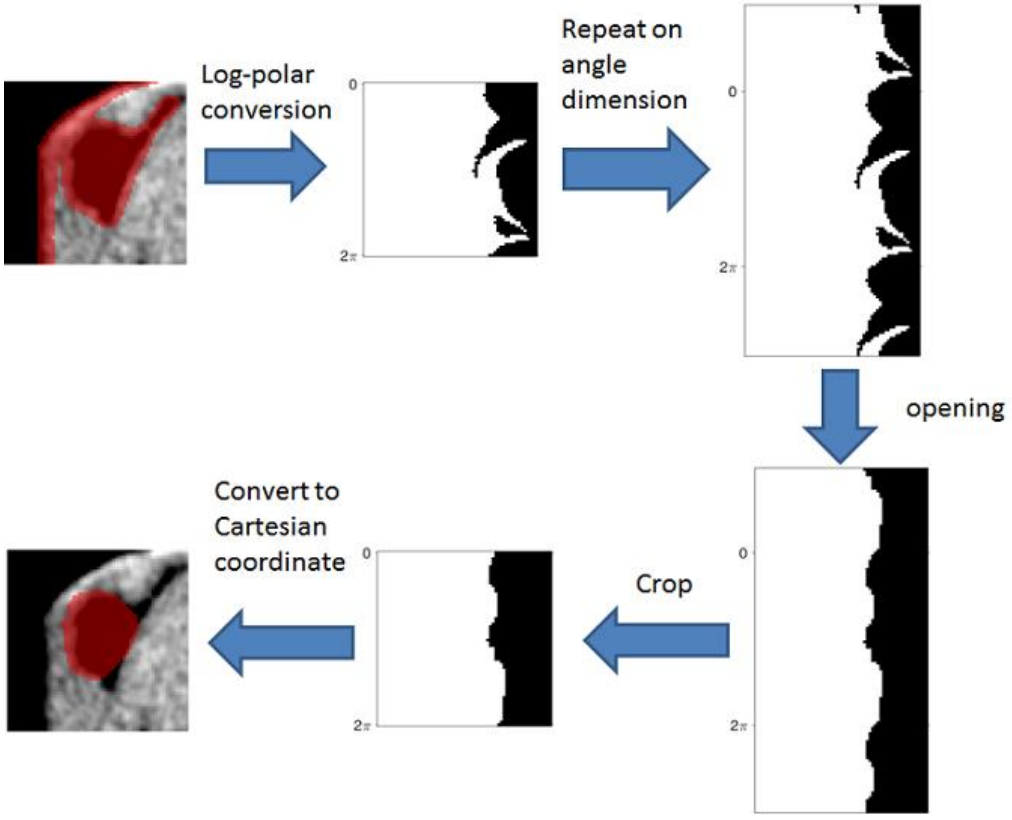

Figure 5.3 Schematic of cyclic morphological opening

In this study, we used 3D square morphological opening instead to strengthen the relationship between slices. After 3D cyclic opening, the pixels far away from the slice center were removed.

After converting the volume bank to Cartesian coordinate, 2D opening with a small structure was performed along with x and y direction to remove residual errors.

5.2.5 Ablation Volume Analysis

Each CT ablation data was created by virtually slicing the volume along the antenna mentioned in chapter 4 [195]. Gross pathology was co-registered and rescaled to the radiological virtual slice from the last time point according to the location and length of the antenna and a metallic fiducial visible on each sample image. Three independent observers (3-5 years research experience in thermal ablation each) manually segmented the ablation zone on the CT virtual slices and gross pathology by delineating along the sharp transition of color or attenuation using ImageJ (National Institutes of Health). Dice's coefficient was used to quantify similarity among ablation zone automatically and manually segmented from CT images and gross pathology, and to examine similarity between observers [196]

$$DICE = \frac{2J}{1+J} \tag{5.11}$$

where J is a Jaccard index. For similarity comparison,

$$J_{path-rad} = \frac{A_{abl1} \cap A_{abl2}}{A_{abl1} \cup A_{abl2}} \tag{5.12}$$

where A_{abl1} and A_{abl2} were the ablation zones from different source, either from automatic segmentation on radiological image or from manual segmentation performed by a given observer on radiological or pathological images. Similarity of ablation zone between each segmentation method and pathology were then evaluated from the mean and standard deviation of the Dice coefficients from all observers. To evaluate intra-observer agreement,

$$J_{intra} = \frac{A_1 \cap A_2 \cap A_3}{A_1 \cup A_2 \cup A_3} \tag{5.13}$$

where A_n was the segmentation mask generated by the n-th observer for radiological and pathological images. Agreement between observers was characterized by the mean and standard deviation of this Dice coefficient. To compare the performance of automatic segmentation between CECT and CT data, the similarity measurement was performed on both data separately as well.

Long and short dimensions of automatically segmented, manually segmented and pathological ablation zone were delineated by straight lines passing through the ablation center on each kind of ablation mask. The correlation between measurements made at ablation zone on each segmentation method and gross pathology were quantified by Pearson's coefficient. The absolute difference (A.D.) and relative difference (R.D.) of measurements among automatic segmented and manual segmented radiological ablation zone and pathological ablation zone were used to quantify the shape difference of ablation zone by the following formula:

$$A.D. = \left|M_{rad} - M_{path}\right| \tag{5.14}$$

$$R.D. = \frac{A.D.}{M_{path}} \tag{4.10}$$

Where M_{path} and M_{rad} are the pathological and radiological measurements.

5.3 Results

5.3.1 Ablation Zone Similarity analysis

Since the proposed method performs ablation zone segmentation without any prior information about the ablation procedure such as attenuation of the ablation zone or applicator location, the ablation volume at each time point during the ablation procedure could be extracted from each CT volume **(Figure 5.4)**. Automatic segmented radiological ablation zones were quite similar to pathological ablation zone and achieved similar performance compared to manual segmentation (Dice similarity: Manu.-Path = 0.81 ± 0.04, Auto.-Path = 0.83 ± 0.02; **Table 5.2**). In CECT data,

the performance of automatic and manual segmentation was similar since the more distinguishable ablation zone caused by brightening background tissue resulted in consistent manual segmentation similar to automatic segmentation (similarity for CECT: Manu.-Path. = 0.83 ± 0.03; Auto.-Path. = 0.83 ± 0.02; Manu-Auto.= 0.81 ± 0.04; intra-observer similarity for CECT = 0.75 ± 0.10; **Table 5.3; Figure 5.5)**. However, the ablation zone was not clearly visible on conventional CT image, resulting in inconsistency on manual segmentation between observers (intra-observer similarity for CT = 0.59 ± 0.05; **Table 5.3; Figure 5.5)**. Therefore, the performance of manual segmentation was poorer than its of automatic segmentation, which demonstrating the robust performance of our proposed performance segmentation (similarity for CT: Manu.-Path. = 0.76 ± 0.03; Auto.-Path.= 0.84 ± 0.02; **Table 5.3**).

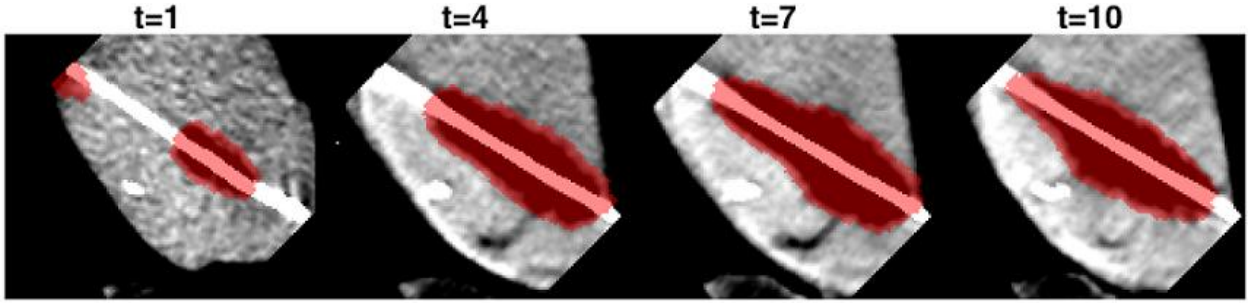

Figure 5.4 Example of segmentation on time serial CECT images

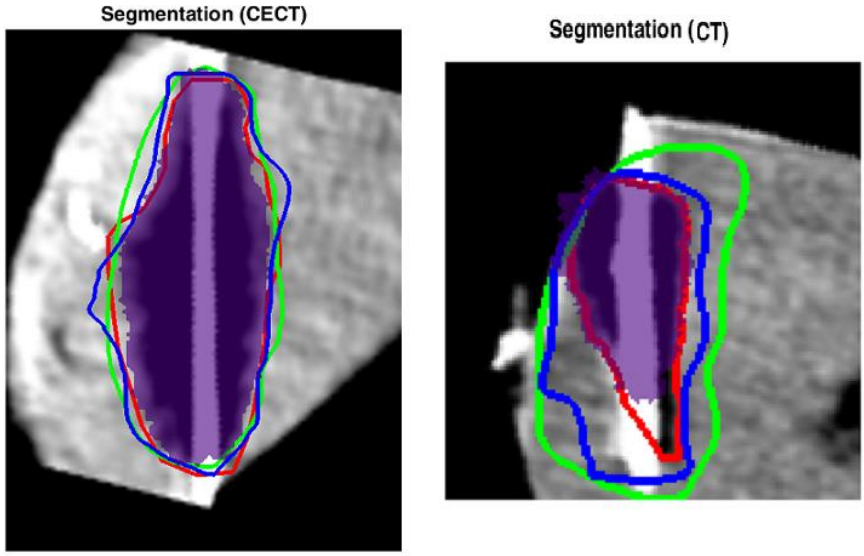

Figure 5.5 Example of segmentation on CECT and CT. Red, green and blue lines are ablation zone contour manually segmented by observer. The region with indigo color is automatically segmented ablation zone

Table 5.2 Similarity of ablation zone between automatic segmentation, manual segmentation on radiological image and gross pathology. Data provided as mean±standard deviation. Manu.=Manual segmented radiological ablation zone; Path=Pathological ablation zone; Auto=Automatic segmented radiological ablation zone.

	Path. v.s Rad.				*Intra-observer*		
	Mean DICE coefficient	*Minimum DICE coefficient*	*Maximum DICE coefficient*		*Mean DICE coefficient*	*Minimum DICE coefficient*	*Maximum DICE coefficient*
Manu-Path	0.81±0.04	0.58	0.93	Path.	0.85±0.06	0.79	0.93
Auto-Path	0.83±0.02	0.52	0.92	Manu.-Rad	0.70±0.12	0.53	0.90
Auto-Manu	0.78±0.05	0.54	0.93				

Table 5.3 Similarity of ablation zone among different source with CECT and CT separately. Data provided as mean±standard deviation. Manu.=Manual segmented radiological ablation zone; Path=Pathological ablation zone; Auto=Automatic segmented radiological ablation zone.

	Path. v.s Rad.						*Intra-observer*	
	Manu v.s Path (CECT)	*Auto v.s Path* (CECT)	*Auto v.s Manu* (CECT)	*Manu v.s Path* (CT)	*Auto v.s Path* (CT)	*Auto v.s Manu* (CT)	*Manu-Rad* (CECT)	*Manu-Rad* (CT)
Mean	0.83±0.03	0.82±0.02	0.81±0.04	0.76±0.03	0.84±0.02	0.73±0.02	0.75±0.10	0.59±0.05
Min.	0.72	0.52	0.65	0.58	0.67	0.54	0.59	0.53
Max.	0.93	0.92	0.93	0.89	0.92	0.93	0.90	0.66

5.3.2 Measurement Variability Analysis

The mean relative area difference between automatic segmentation and pathological ablation zone was lower than its between manual segmentation and pathological ablation zone. (Manu-Path = 32.9 ± 16.8%, Auto-Path = 17.9 ± 3.2%; **Table 5.4**). A similar trend was noted in diameter measurements with smaller differences overall (long axis: Manu-Path = 13.0 ± 9.8%, Auto-Path = 11.1 ± 3.2%; short axis: Manu-Path = 21.8 ± 5.8 %, Auto-Path = 16.2 ± 3.4%; **Table 5.4**). These results suggest that automatic segmentation provided more reliable detection of the ablation zone

dimensions compared to manual segmentation. Comparing the improvement of relative area difference between CECT and CT data, the improvement in CT was larger than in CECT (for CECT: Manu-Path = 23.9 ± 11.2%, Auto-Path = 20.5 ± 3.3%; for CT: Manu-Path = 50.9 ± 16.6%, Auto-Path = 12.6 ± 3.4%; **Table 5.4**). The relative difference of dimensions also demonstrated the same trend as relative area difference (long axis (CECT): Manu-Path = 12.5 ± 11.3%, Auto-Path = 10.7 ± 2.9%; long axis (CT): Manu-Path = 14.0 ± 7.4%, Auto-Path = 11.9 ± 3.9%; short axis (CECT): Manu-Path = 19.2 ± 5.8 %, Auto-Path = 20.3 ± 2.9%; short axis (CT): Manu-Path = 26.8 ± 1.6 %, Auto-Path = 7.9 ± 4.6%; **Table 5.4**). The results above indicated the ability of proposed method to segment ablation zone in low-contrast image.

Table 5.4 Measurement of difference between ablation zone automatically and manually segmented on CECT and CT data and pathological ablation zone. Data provided as mean±standard deviation. Manu.=Manual segmented radiological ablation zone; Path=Pathological ablation zone; Auto=Automatic segmented radiological ablation zone.

		Absolute Difference (cm or cm^2)			*Relative Difference (%)*		
		Mean	*Maximum*	*Minimum*	*Mean*	*Maximum*	*Minimum*
Manu-Path (Whole)	Area	3.15±1.07	16.15	0.01	32.9±16.8	121.3	0.2
	LA	0.55±0.27	2.34	$<10^{-3}$	13.0±9.8	80.8	<0.01
	SA	0.55±0.14	1.89	0	21.8±5.8	53.7	0
Auto-Path (Whole)	Area	2.74±1.03	25.38	0.12	17.9±3.2	63.7	1.9
	LA	0.55±0.16	2.79	<0.01	11.1±3.2	29.1	0.1
	SA	0.47±0.17	3.02	<0.01	16.2±3.4	63.9	0.2
Auto-Manu (Whole)	Area	3.45±1.72	14.43	0.05	30.0±10.0	68.2	0.9
	LA	0.73±0.28	1.89	0	15.5±4.9	41.3	0
	SA	0.65±0.22	1.68	0	24.1±7.0	88.9	0
Manu-Path (CECT)	Area	3.13±0.94	16.15	0.01	23.9±11.2	77.1	0.2
	LA	0.56±0.29	2.34	$<10^{-3}$	12.5±11.3	80.8	<0.01
	SA	0.56±0.17	1.89	0	19.2±5.8	53.7	0
Auto-Path (CECT)	Area	3.70±1.20	25.38	0.13	20.5±3.3	63.7	3.8
	LA	0.60±0.16	2.79	<0.01	10.7±2.9	29.1	0.1

Auto-Manu (CECT)	SA	0.63±0.18	3.02	<0.01	20.3±2.9	63.9	0.2
	Area	3.34±1.83	14.43	0.12	28.2±10.2	68.2	1.5
	LA	0.64±0.30	1.89	0	13.0±4.4	36.2	<0.01
Manu-Path (CT)	SA	0.68±0.22	1.62	<0.01	24.5±7.8	88.9	0.1
	Area	3.19±1.07	8.33	<0.01	50.9±16.6	121.3	1.1
	LA	0.53±0.25	1.47	<0.01	14.0±7.4	35.5	0.1
Auto-Path (CT)	SA	0.51±0.06	0.98	0.07	26.8±1.6	52.5	4.9
	Area	0.80±0.63	3.33	0.12	12.6±3.4	27.4	1.9
	LA	0.45±0.16	0.93	0.04	11.9±3.9	23.9	0.8
Auto-Manu (CT)	SA	0.17±0.16	0.77	0.01	7.9±4.6	26.2	0.7
	Area	3.66±1.30	10.08	0.05	33.6±4.5	60.3	0.9
	LA	0.92±0.07	1.85	0.13	20.5±3.5	41.3	3
	SA	0.60±0.24	1.68	0	23.3±5.9	43.6	0

5.3.3 Dimension and Area Correlation Analysis

Automatically segmented ablation zones were highly correlated to gross pathology, but manually segmented ablation zones provided a greater correlation between imaging and pathology in terms of ablation area **(Table 5.5, Figure 5.6(a)).** While the pathological-radiological correlation of long axis length from both types of segmentation were high **(Figure 5.6(b))**, the correlation coefficient of the short axis length was lower on automatically segmented ablation zones than manually segmented ablation zones. The correlation coefficient of the short axis length was lowest on both types of segmentation **(Table 5.5; Figure 5.6(b))**, suggesting that both manual and automatic segmentation may mis-estimate the width of the ablation zone, but automatic segmentation has greater errors on it.

Correlation coefficients of all measurements in both manual and automatic segmentation methods were higher on CT data than CECT data. **(Table 5.6, 5.7; Figure 5.7(b))**. Among all measurements, the correlation coefficient of short axis length has largest difference between automatic and manual segmentation, which also negatively influenced the correlation coefficient of area **(Table 5.6, 5.7).**

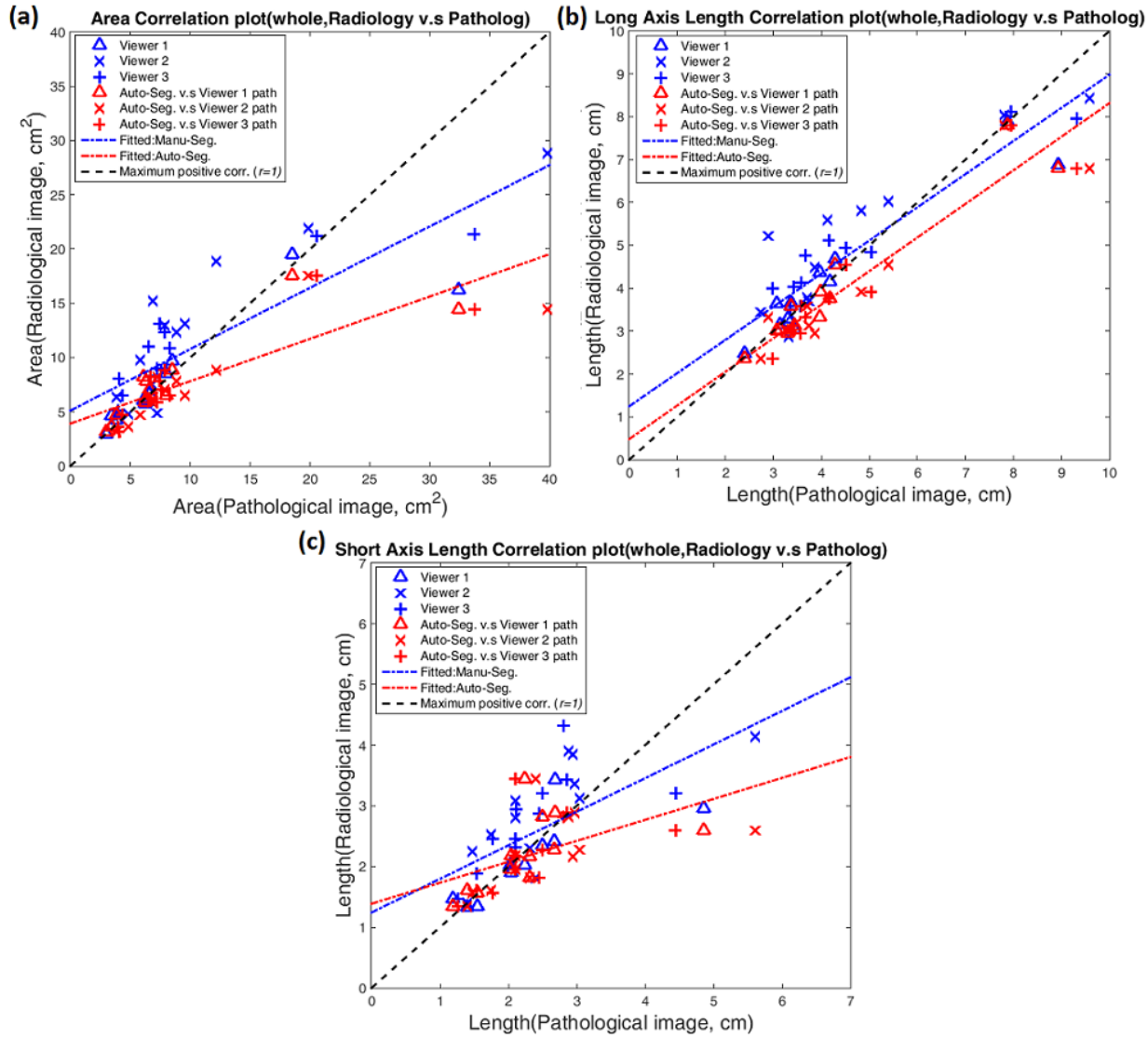

Figure 5.6 Path-rad correlation of (a) area, (b) long axis and (c) short axis for automatic and manual segmentation. Fit and correlation metrics are noted in Table 5.4.

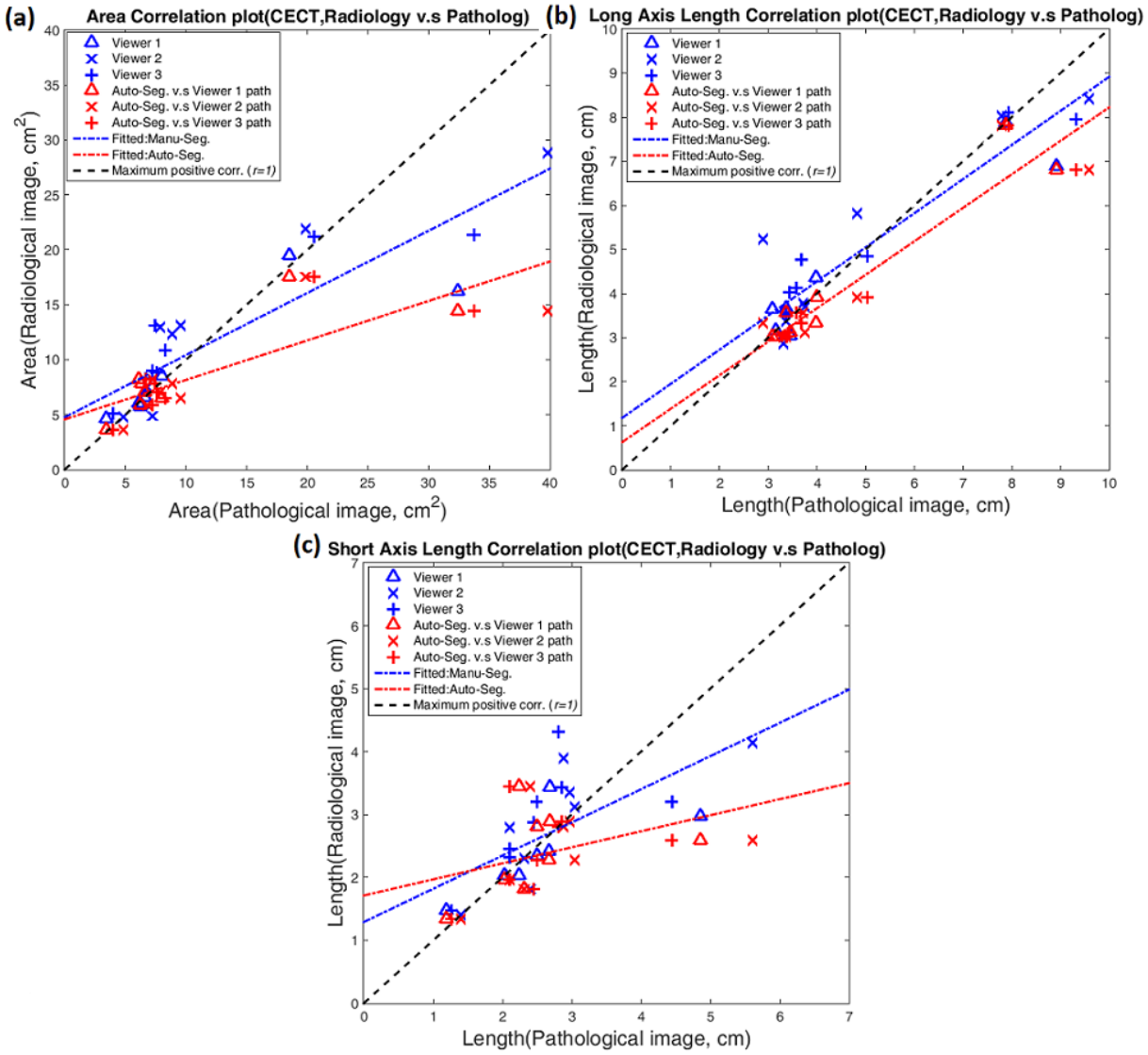

Figure 5.7 Path-rad correlation of CECT :(a) area, (b) long axis and (c) short axis for automatic and manual segmentation in CECT data only. Fit and correlation metrics are noted in Table 5.5.

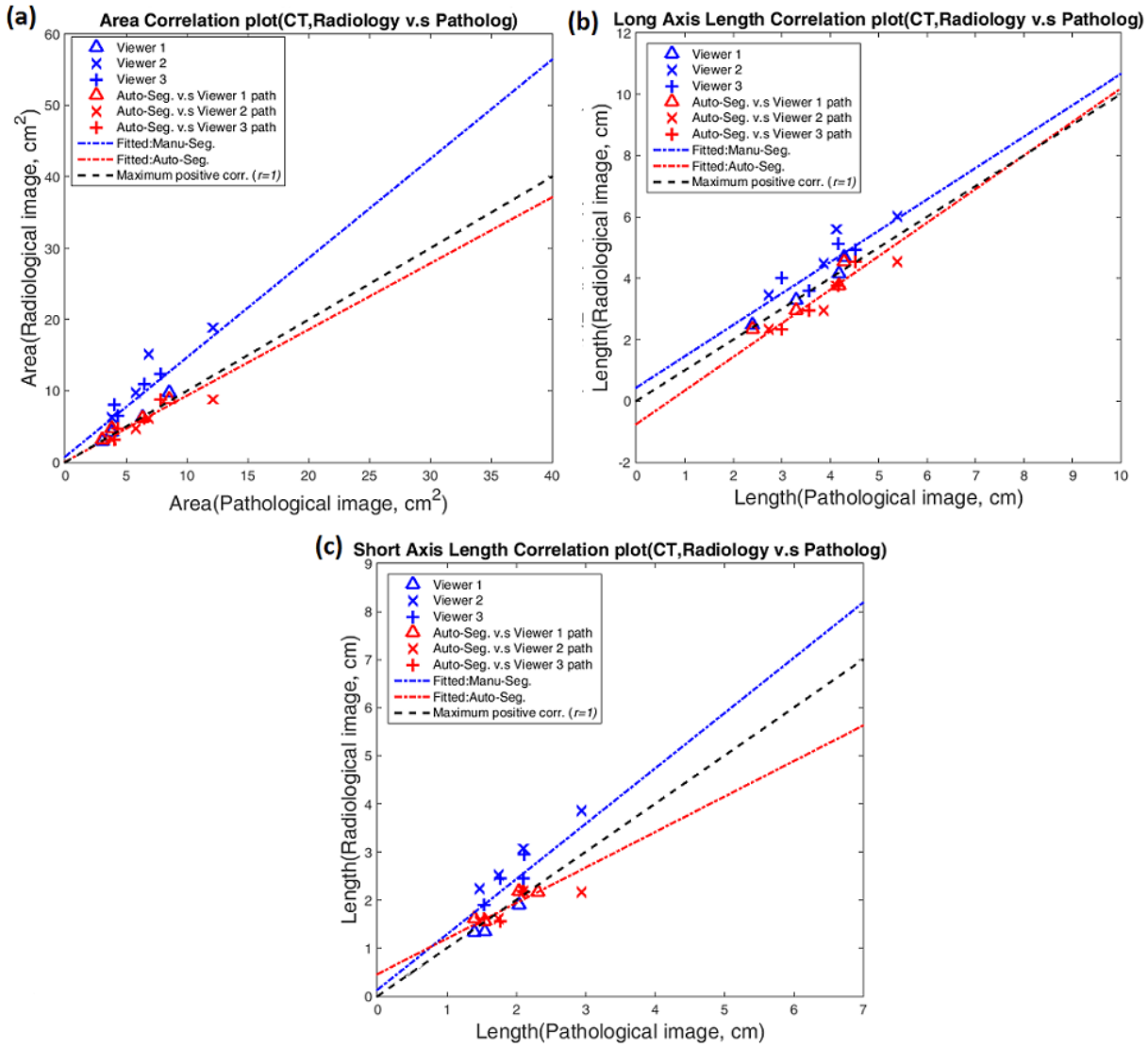

Figure 5.8 Path-rad correlation of CT (a) area, (b) long axis and (c) short axis for automatic and manual segmentation in CECT data only. Fit and correlation metrics are noted in Table 5.6.

Table 5.5 Correlation coefficients which comparing each segmented ablation zone. LA=Long Axis, SA=Short Axis. Manu.=Manual segmented radiological ablation zone; Path=Pathological ablation zone; Auto=Automatic segmented radiological ablation zone

	Manu.-Seg v.s Path			*Auto-Seg v.s Path*			*Manu-Seg v.s Auto-Seg*		
	Area	*LA*	*SA*	*Area*	*LA*	*SA*	*Area*	*LA*	*SA*
Coefficient	0.9	0.96	0.78	0.83	0.95	0.53	0.93	0.97	0.6
R^2	0.82	0.91	0.61	0.69	0.91	0.28	0.86	0.94	0.36
P	$< 10^{-4}$	$< 10^{-5}$	<0.01	$< 10^{-3}$	$< 10^{-5}$	0.08	$< 10^{-4}$	$< 10^{-6}$	0.04

Table 5.6 Correlation coefficients which comparing each segmented ablation zone in CECT data. LA=Long Axis, SA=Short Axis. Manu.=Manual segmented radiological ablation zone; Path=Pathological ablation zone; Auto=Automatic segmented radiological ablation zone

	Manu.-Seg v.s Path (CECT)			*Auto-Seg v.s Path (CECT)*		
	Area	*LA*	*SA*	*Area*	*LA*	*SA*
Coefficient	0.92	0.96	0.75	0.81	0.95	0.4
R^2	0.84	0.92	0.56	0.65	0.9	0.16
P	<0.01	$< 10^{-3}$	0.03	0.02	$< 10^{-4}$	0.18

Table 5.7 Correlation coefficients which comparing each segmented ablation zone in CT data. LA=Long Axis, SA=Short Axis. Manu.=Manual segmented radiological ablation zone; Path=Pathological ablation zone; Auto=Automatic segmented radiological ablation zone

	Manu.-Seg v.s Path (CT)			*Auto-Seg v.s Path (CT)*		
	Area	*LA*	*SA*	*Area*	*LA*	*SA*
Coefficient	0.99	0.96	~0.99	~0.99	0.98	0.93
R^2	0.97	0.93	~0.99	~0.99	0.97	0.86
P	0.01	0.04	<0.01	<0.01	0.03	0.11

5.4 Discussion

In this study, we developed an automatic segmentation method to extract the ablation volume from CT scans. Similarity and measurement variability analysis suggested that our proposed method could have similar or even better results of ablation zone detection compared to manual segmentation, which is the traditional ablation zone assessment technique **(Table 5.2)**. Correlation analyses suggested that the dimension and shape of ablation zones extracted by automatic segmentation method were highly correlated with gross pathology **(Figure 5.6; Table 5.5)**. Since there was not any prior ablation-related information used in segmentation, the above results demonstrated the feasibility of ablation zone segmentation and assessment during a procedure with serial CECT for monitoring.

Many image segmentation techniques have been developed over the years. Several have already been applied on post-ablation zone segmentation. For example, a region-growing method has been successfully used in post-ablation imaging for assessing radiofrequency ablation [218]. Region-growing methods operate by thresholding the feature difference between neighboring pixels and the whole segmented region and then gather the similar pixels. When there are uniform and high-gradient image features such the ablation zone in a high-dose post-ablation CECT, the performance of region-growing methods can be excellent. However, the ablation zone on intra-procedural CT or CECT imaging is composited with the growing gas and thermal damage regions, which generates a large variation of attenuation in the treatment region. Therefore, the performance of region-growing will be degraded significantly since it is very difficult to set a fixed threshold to measure the pixel similarity inside ablation zone. Other methods such as active contour or Otsu's method may also be feasible [219], [220]. However, huge variations of attenuation inside the ablation zone again makes these two methods fail in segmentation. Our proposed method extracted several image features to avoid the negative influence of large attenuation variations, and fuzzy C-mean clustering could automatically segregate multi-dimensional image features to gas, transition and normal tissue clusters without any prior information. Therefore, the ablation zone could be extracted without any assumption of ablation zone with our technique.

Correlation coefficients of all basic ablation morphology metrics, especially the short axis length, was low between automatically segmented ablation zone and gross pathology images. One explanation for this observation was the conservative ablation zone segmentation in our proposed method when the transition region was not clearly visible on the radiological image. In this case, only the gas region was segmented, which corresponded to the inner charred region but not the more peripheral region of tissue necrosis on gross pathology images **(Figure 5.9)**. Another reason

for measurement errors was that the air region outside the liver was included in the liver segmentation and then was misjudged as ablation zone **(Figure 5.10)**. Each case occurred once in our series of data. When removing these two outliers from our segmentation results, the correlation coefficient between automatic segmentation and gross pathology was significantly improved, which indicated the automatic segmented ablation zone correlated well with gross pathology once segmenting correctly **(Figure 5.11; Table 5.8)**. Further work will be needed to prevent such errors from occurring in subsequent studies. The presence of air on imaging can be reduced by performing the ablations in a percutaneous, rather than open surgical setting. Similarly, a percutaneous approach may also increase the volume of CT data that can be collected to reduce misregistration errors that may lead to misclassification of tissue necrosis or viability.

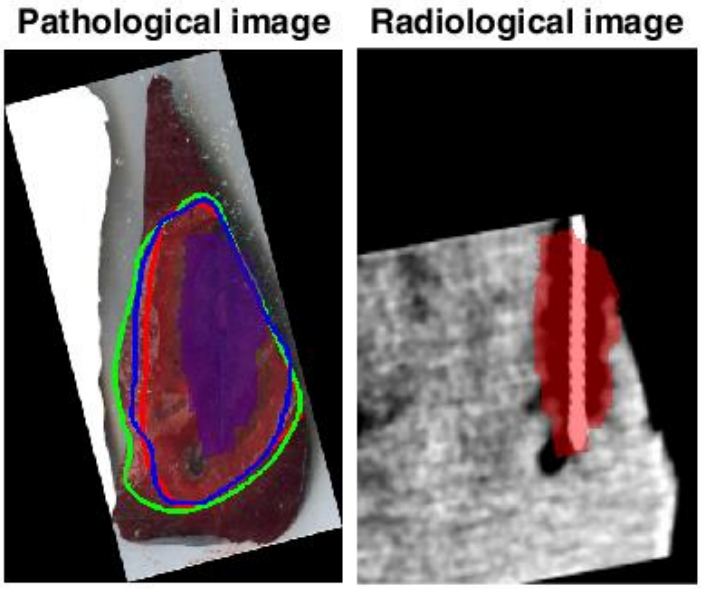

Figure 5.9 Example of Outlier-1 : the proposed method had too conservative segmentation due to unclear transition region

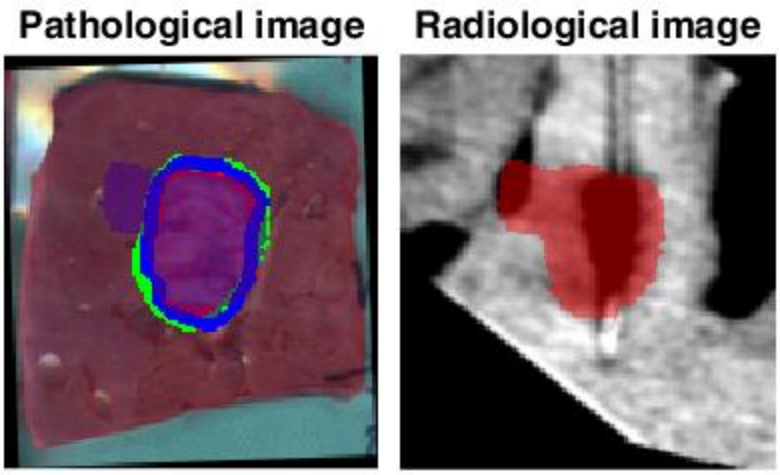

Figure 5.10 Example of Outlier-2 caused by the wrong liver segmentation and resulted in wrong detection on air region outside liver

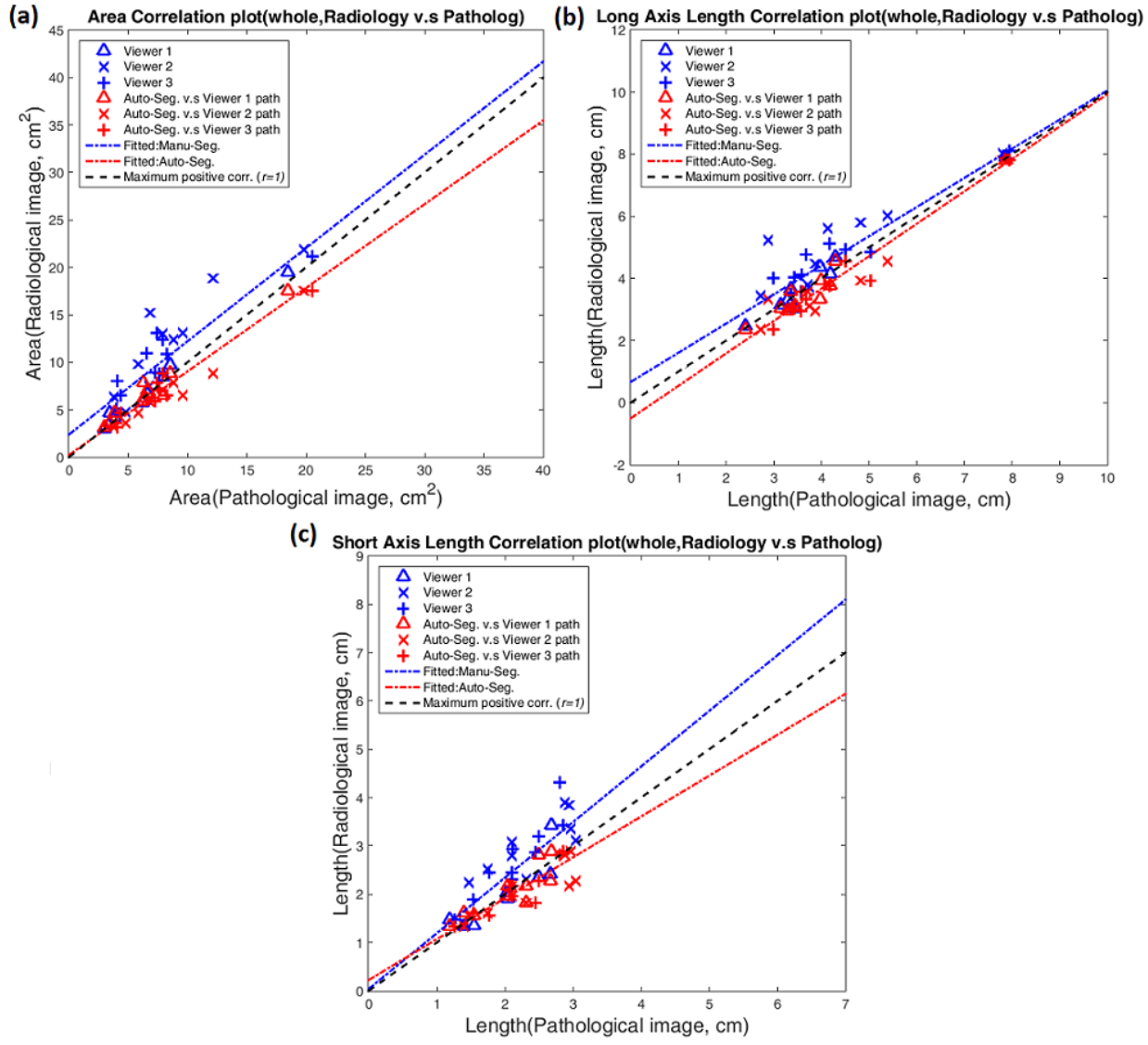

Figure 5.11 Path-rad correlation after removing outlier (a) area, (b) long axis and (c) short axis for automatic and manual segmentation when removing outlier. Fit and correlation metrics are noted in Table 5.8.

Table 5.8 Correlation coefficients which comparing each segmented ablation zone after removing outlier. LA=Long Axis, SA=Short Axis. Manu.=Manual segmented radiological ablation zone; Path=Pathological ablation zone; Auto=Automatic segmented radiological ablation zone

	Manu.-Seg v.s Path			*Auto-Seg v.s Path*		
	Area	*LA*	*SA*	*Area*	*LA*	*SA*
Coefficient	0.96	0.96	0.95	0.99	0.99	0.90
R^2	0.93	0.93	0.89	0.98	0.98	0.81
P	$<10^{-5}$	$< 10^{-5}$	$< 10^{-4}$	$< 10^{-7}$	$< 10^{-7}$	$< 10^{-3}$

Several weaknesses and limitations in the proposed method exist. First, the processing time for segmenting a single CT volume was about 11.77 minutes by using MATLAB 2015a on a computer with Intel Core i7 2.80 GHz CPU and 8 GB memory. Liver segmentation and feature extraction accounted for most of the processing time (8.13 min for liver segmentation and 3.44 min for feature extraction). However, the processing time may decrease much when using a low-level programing language such as C++. Further optimizations to the time-intensive segmentation and extraction code may also help to reduce computational time. Secondly, the proposed method failed to segment ablation zones when the treatment region connected to air regions since the image features of gas outside the organ and inside ablation zone were very similar. Further investigation of image features which could discriminate the gas in these two regions is needed in the future work.

In conclusion, we developed an ablation zone segmentation method combined with texture analysis and unsupervised clustering method. The results showed that the segmented ablation zone from the proposed method on either CT or CECT was more similar to gross pathology, demonstrating its ability to detect ablation zone robustly. Future studies will focus on reducing the

processing time to make it feasible in real-time ablation monitoring. Another direction of future studies will be investigating the performance of the proposed method on ablation on other organs or other ablation techniques.

Chapter 6 Modeling the growth rate of ablation volume from periodic CT scanning

6.1 Introduction

As described in chapter 5, a large enough ablation zone to cover the target tumor and a margin of seemingly normal tissue is the requirement of a successful ablation treatment. While real-time ablation monitoring may assist radiologists in ablation lesion surveillance and help to correct any mistakes that might happen during a procedure, the inability to predict ablation zone growth is still a problem. Incorrect treatment parameters (e.g. power, treatment time, applicator position, etc.) may cause treatment errors that serve to reduce overall treatment efficacy or safety. Therefore, a robust model used in describing the growth of ablation zone and predicting the ablation zone is necessary to improve efficacy and ensure safe treatments.

Currently, temperature is the most common way to predict the ablation zone size [203], [204], [221], [222]. The temperature is simulated before treatment and then converted to predict ablation zone morphology based on models of thermal dose and cell death. However, the theoretical model used to simulate temperatures is not 100% accurate or robust to all changes that occur in the target region, making such predictive models of limited clinical value to date. In addition, other crucial factors such as perfusion and number of blood vessels may influence on ablation zone size. Ignoring these factors may lead to major errors in the ablation zone prediction. Therefore, a model directly related to the treatment time is required to predict the ablation volume.

Patterson et al. discussed the relationship among time, number of central vessels and lesion size through linear regression in 1998 [175]. However, they only discussed the relationship between ablation lesion depth, which was the diameter of ablation zone measured on the plane sliced along with applicator, and treatment time. Brace et al. and Hines-Peralta et al. both discussed the relationship between lesion diameter and treatment time by using different equation for nonlinear regression [199], [223]. Both of them revealed the trend of ablation lesion growth: the

ablation diameter rapidly increases in the beginning of procedure and then slows the rate of increase at the end of procedure. Despite discovering a clue for ablation lesion growth, the model of volume estimation based on an assumption of perfectly elliptical or spherical ablation shape may not be applicable in all situations (e.g. ablation close to the boundary). In addition, the data for the above models was collected by manually measuring the length of long axis and short axis on the post-ablation pathological images with different treatment times. Since power delivered for the complete treatment and during the treatment are different, diameter measured on post-ablation scans with different treatment times may be different to the actual diameter in during procedure. While Brace et al. collected the data by manually measuring the diameter on intra-procedural CT scans and built a new model for microwave ablation, this model may still have large deviation due to the bias on manual measurements.

Our present study utilized the segmented ablation volume from periodic CT scan to build a new model for the ablation zone growth with time.

6.2 Methods

6.2.1 *In-vivo* Ablation Procedure

For model training, total 15 Microwave ablations were created in the livers of six swine using a 2.45 GHz microwave generator (Certus 140 ; NeuWave Medical Inc., Madison, WI) and triaxial antenna (LK 15; NeuWave Medical Inc., Madison, WI) with different setting of power and duration (6 for 100W 10 min and 9 for 100W 5 min. Each ablation was performed low-dose CT or CECT scan with total ten volumes acquired (1.25/0.625 mm thickness, 80 kVp, 80 mA; GE 750 HDCT). In CECT scan, a 40 ml bolus of iodinated contrast (300 mg/ml iohexol; GE Healthcare, Waukesha, WI) was injected 1 min before ablation and then contrast was infused continuously at 0.3 ml/s to maintain a similar level of enhancement in the perfused liver during the procedure.

For model testing, a total of six microwave ablations were created in the livers of three swine using a 2.45 GHz microwave generator, with three at 100W for 10min and another three at 95W for 4 min 30 sec. For 100W and 10 min ablations, low-dose CECT scans (1.25 mm thickness, 80 kVp, 80 mA; GE 750 HDCT) were performed at 1 min intervals. For 95W and 4 min 30 sec ablations, high-dose conventional CT scan (1.25 mm thickness, 120 kVp, 250 mA; GE 750 HDCT) at 1 min intervals.

Each swine was euthanized after the procedure and their livers were removed. Each ablation was sliced along the antenna axis to display the largest ablation zone and then photographed for gross pathology to provide a "ground truth" pathological assessment.

6.2.2 Preprocessing and ablation volume segmentation

All the low-dose intra-procedural CT scan was processed using HYPR to enhance the visualization of ablation zones via the procedure mentioned in previous chapters. Each CT volume was rescaled to ensure the pixels were isotropic (1mm x 1mm x 1mm). Each slice was cropped as 25mm to 25mm centered at the applicator. Ablation volumes at each time point during each procedure were then created by manually delineating the ablation zone along with a high contrast boundary on the liver region slice by slice on the cropped volume.

6.2.3 Modeling and examining the growth of ablation volumes

All manually segmented ablation volumes were converted to cylindrical coordinates with respect to the ablation volume center. The vertical distances between the center point and points on the surface of the ablation volume were then calculated to represent the long axis diameter. The radius and the vertical distance were decomposed by spherical harmonics [224]–[227].

Spherical harmonics (SH) are a set of orthogonal functions over a unit sphere which can be used to describe complicated 3D surfaces. Any real valued function can be decomposed into a set

of spherical harmonics. Suppose there is a real function $F(\theta, \varphi)$. This real function could be decomposed by the following formula,

$$F(\theta, \varphi)=\sum_{l=0}^{\infty} \sum_{m=-l}^{l} r_{lm} Y_{lm}(\theta, \varphi) \quad (6.1)$$

Where the basis $Y_{lm}(\theta, \varphi)$ is,

$$Y_{lm}(\theta, \varphi) = \sqrt{\frac{2l+1}{4\pi} \frac{(l-m)!}{(l+m)!}} P_l^m(cos\theta) e^{im\varphi} \quad (6.2)$$

Where $P_l^m(cos\theta)$ is associated Legendre polynomial function. The coefficient $\mathrm{r_{lm}}$ could be an acquired inner product with its corresponding basis. The function could also be reconstructed by a linear combination of spherical harmonic bases. In this study, the radius $R(\theta, \varphi)$ and vertical distance $Z(\theta, \varphi)$ were used in SH decomposition. The 0-level coefficient r_{00} was extracted after decomposition since it is highly related to the average value of the function [226], [227]. The increasing ratio of radius and vertical distance were acquired via dividing the 0-level coefficient of both radius and vertical distance by the first coefficient **(Figure 6.1)**. Both r and z- increasing was fit to the following non-linear formula [223],

$$ratio = 1 + At + B\sqrt{t} \quad (6.3)$$

CT data acquired during both ablation protocols were used to train the model of r- and z- growth over time. Growth was expressed as a ratio to the value at the first time point. To examine the performance of models, the predicted ablation volume at each time point was generated by applying the model on the initial manual segmented ablation volume and comparing to the observed test ablation volume. The post-ablation volumes of observed test data were also estimated by calculating ellipsoid volume with manually measured lengths of the long and short axis length through gross pathology.

$$V_{post-abl} = \frac{1}{6}\pi b^2 a \quad (6.4)$$

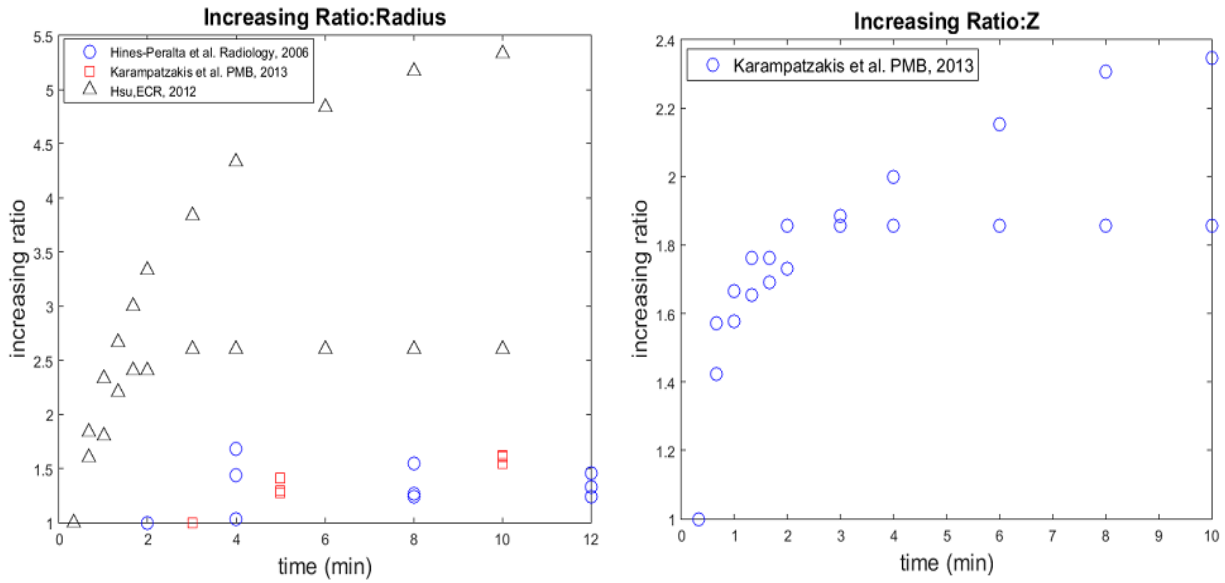

Figure 6.1 the increasing ratio of r and z calculated directly from other published data [199], [228], [229]

6.3 Results

6.3.1Extraction of diameter growth ration – Simulation Example

The ellipsoid with growing long and short axis was used to demonstrate the performance of the proposed method by the following temporal relationship between long/short axis and time **(Figure 6.2)**,

$$\begin{cases} x = 5t^{0.45} \\ y = 5t^{0.45} \\ z = 5t^{0.75} \end{cases} \tag{6.4}$$

The estimated growth ratio slightly overestimated the real growth ratio for radius, and slightly underestimated for length **(Figure 6.3)**. However, the error between real and estimated growth ratios was within three pixels, which is 3 mm in this study. The small error between estimated and

true growth ratios demonstrated that the parameters extracted by our method were sufficient to build a model.

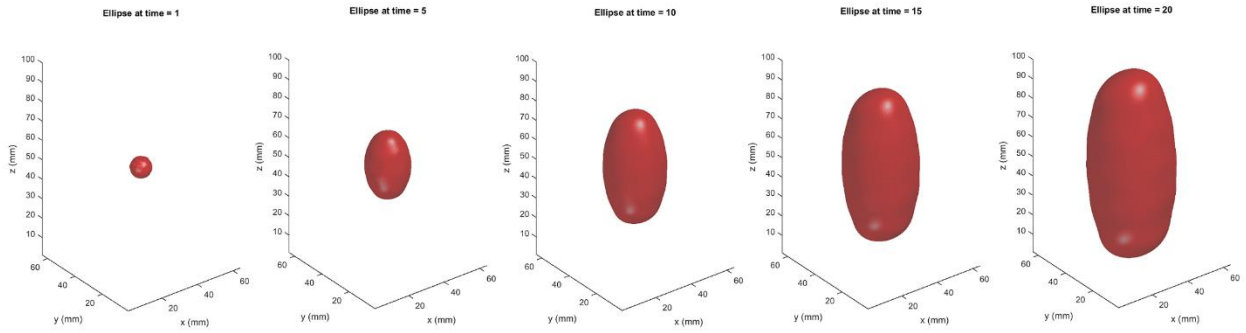

Figure 6.2 the ellipsoid with growing long and short axis

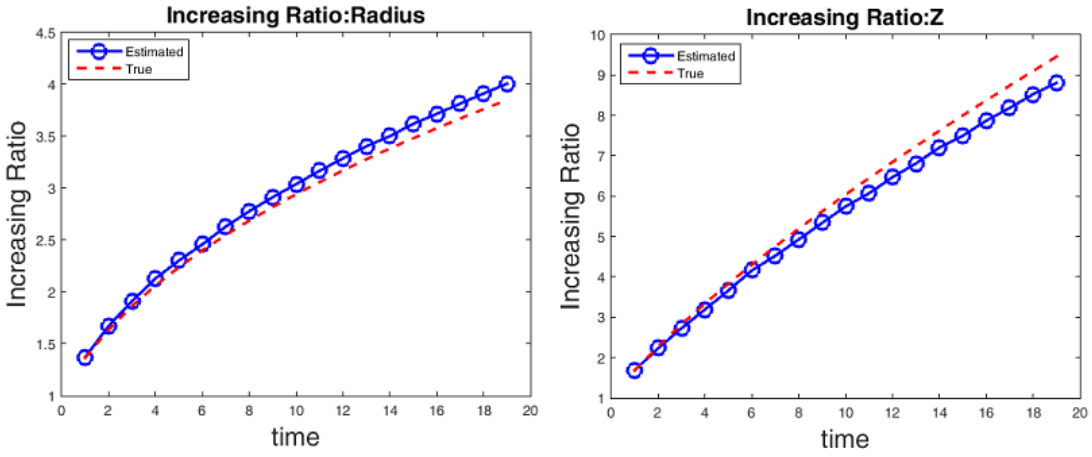

Figure 6.3 Estimated increasing ratio of radius and vertical distance for growing ellipsoid

6.3.2 Increasing ratio Modeling and Examination

The final parameters of 5 min 100W ablation model after nonlinear regression of the object function were **(Figure 6.4)**:

$$R\_ratio_{5min} = 1 + -0.10763\mathrm{t} + 0.54469\sqrt{t} \tag{6.5}$$

$$Z\_ratio_{5min} = 1 + -0.16426\mathrm{t} + 1.3031\sqrt{t} \tag{6.6}$$

The final parameters of 10 min 100W ablation model after nonlinear regression of the object function were **(Figure 6.5)**:

$$R\_ratio_{10min} = 1 + -0.030845\mathrm{t} + 0.24144\sqrt{t} \quad (6.7)$$

$$Z\_ratio_{10min} = 1 + -0.050896\mathrm{t} + 0.64236\sqrt{t} \quad (6.8)$$

The R^2 for increasing ratios of 100W, 5min ablation were 0.736 and 0.56 for radius and vertical distance, and were 0.218 and 0.208 for 100W, 10min ablation. The model simulated ablation volume on both 5 min and 10 min were over-estimated so that the simulated ablation volume was higher than the observed ablation volume **(Figure 6.6)**. Both under-estimation and over-estimation happened when using out model to estimate post-ablation volumes.

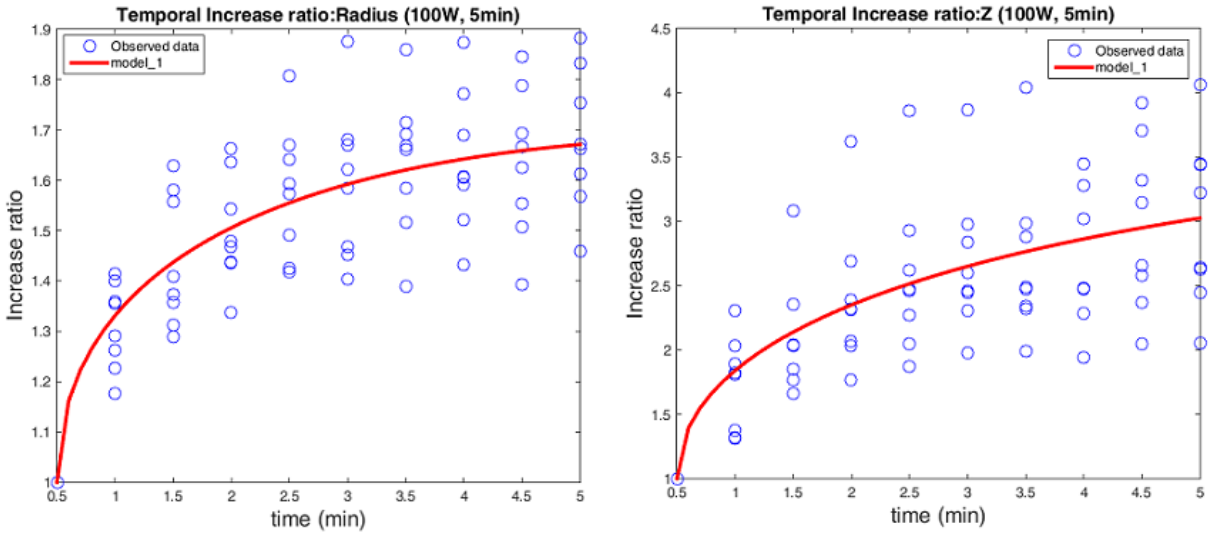

Figure 6.4 Model for 100W 5 min microwave ablation

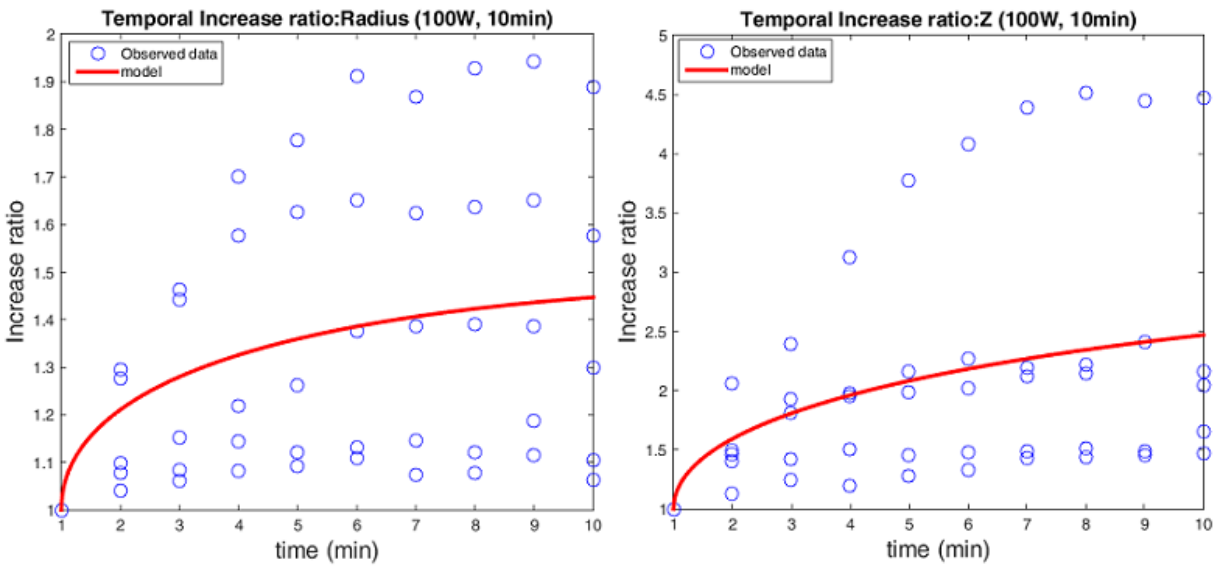

Figure 6.5 Model for 100W 5 min microwave ablation

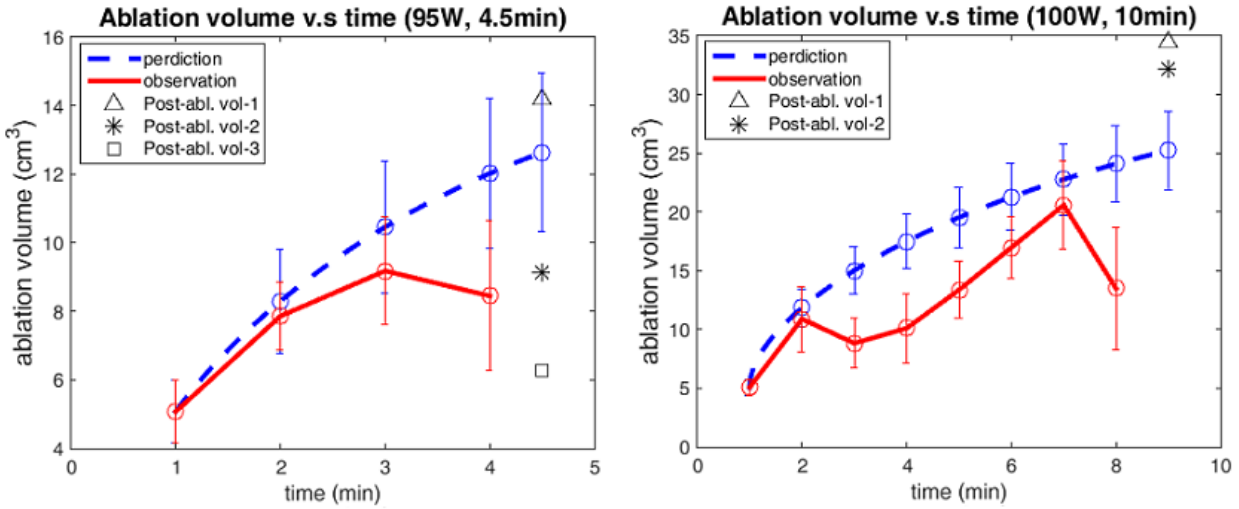

Figure 6.6 Validation of model for 100W 5 min and 10 min ablation

6.4 Discussion

In this study, we investigated the feasibility of modeling the temporal growth of both the long and short axes of microwave ablations. Spherical harmonics were used to describe the radius and vertical distance with respect to the ablation center, and the 0-level coefficient was used to represent the growth ratio. Despite having some error between predicted and observed ablation

volumes, this modeling method demonstrated a similar trend of ablation volume growth, which indicated its potential to describe the real volume change rate during procedures.

There were several possible explanations for the gap between predicted and observed intra-procedural data. The power and treatment duration are two important factors to ablation volume size. The rate of change in the ablation zone short axis and long axis diameters may be relatively low at the end of procedure, with diminishing volume change after 4-5 min of heating. In addition, the volume of 95W ablations is expected to be slightly smaller those at 100W. Therefore, the error between predicted and observed data became large, especially after 4 min. Training data could also be another possible reason for this phenomenon. We gathered the data under different *in-vivo* environment (eg. vessel near ablation region, high blood perfusion etc.), which may highly influence the ablation volume and then influence the model of ablation volume growth. Other possible reason may be the mis-estimation on both training data and observed data since the ablation volume highly depends on personal experience by manual segmentation. A reliable automatically segmentation could be helpful to provide more consistent and accurate ablation volume for modeling. Also, collecting more data to train the model could be an alternative solution to improve the accuracy.

Despite having certain error between predicted and observed data, the trend at first few time point matched pretty well, which indicated that our method could still have potential to describe the temporal growth of ablation volume during procedure once overcome the above challenges.

Chapter 7 Summary and future study

7.1 Summary

Imaging feedback is crucial to thermal ablation since the minimally invasive nature of the procedure makes it more difficult to inspect, observe and monitor the whole treatment compared to conventional surgery. Although there are many medical imaging modalities utilized during thermal ablation, all of them have disadvantages for real-time ablation monitoring. Moreover, the lack of intra-procedural computer-aided diagnosis system and a model for describing the growth of ablation volume makes it difficult to both plans the procedure on any given patient, and to evaluate the efficacy of the procedure once started.

This dissertation examined the feasibility of serial CECT for real-time monitoring. First, we analyzed contrast agent behavior indirectly via attenuation analysis, and developed a method to enhance visualization of the ablation zone on low-dose periodic CECT to solve the dose problem during serial CECT. We developed an automatic ablation zone segmentation method to assist users in detecting and measuring ablation volume, then built a basic model directly related to the growth observed ablations to help predict ablation growth during procedures based on early imaging features. The contribution of the work is as follows:

- This study provided an indirect method to analyze the behavior of contrast material with traditional CECT scan. This method could be beneficial to estimate blood perfusion or be used in other application to help physicians and researchers to study complex diseases.
- This study provided better understanding of contrast agent behavior during thermal ablation. According to our analysis, iodinated contrast agent was brought into the normally perfused tissue by blood flow and trapped inside the region, increasing x-ray attenuation and highlighting this region. This result could contributing to providing a knowledge about the effects on contrast agent behavior from physiology and biomechanism of ablation and

its influence on display of ablation zone on image, a reference for using any contrast agent highlighting ablation zone or any material increasing efficacy of treatment during ablation.

- This study examined the feasibility of CECT in real-time ablation monitoring. While the attenuation of ablation zones increased due to trapped iodinated contrast agent, the visibility of ablation zones were still improved compared to non-contrast imaging. Therefore, CECT is feasible to monitor thermal ablations intra-procedurally.
- The study addressed challenges in dosing for intra-procedural CT imaging. Both statistical and ablation analysis of our HYPR processing method indicated that the visualization of ablation zone was significantly improved when using low-dose CECT following the regulation of radiation dose. Therefore, physicians and researchers can utilize low-dose scanning while still retaining sufficient image quality to observe ablation dynamics during a procedure.
- This study provided a robust, automatic technique to assist radiologists in ablation zone detection and ablation volume estimation. According to our result, the proposed method could segment ablation zones accurately even using traditional CT scanning. Since our method did not need any prior information (e.g., seed placement) to achieve ablation zone segmentation, it could contribute to not only the post ablation volume detection but also intra-procedural detection of ablation volumes for automated scanning or even real-time control of the ablation parameters.
- This study provided a preliminary model describing the temporal growth of the long and short axes of the ablation zone. This model could contribute to treatment planning and monitoring by comparing the observed volume and simulated volume.

7.2 Future study

The dissertation provided a solid foundation for real-time ablation monitoring and treatment predicting by examining the feasibility of CECT in real-time ablation monitoring, providing potential solution for does challenge, developing robust, automatic segmentation method for ablation volume and designing modeling for description of ablation dimension growth. Based on this research, the future studies could be in the following aspect.

The present study used a serial low-dose CECT scanning protocol in which the accumulated dose was near a conventional high-dose abdominal CECT exam. While dose regulation may not be as relevant in adult cancer patients, the level of radiation dose is relevant to younger patients and to medical staff assisting with the procedure during CT scanning. To ensure that serial low-dose CECT scanning can be applied to any patient with any age under any situation, examining the tolerance of dose reduction for our HYPR processing method is necessary.

The present study only segmented ablation zones which were performed on normal liver tissue. However, the ablation volume may be changed when performing microwave ablation on different kinds of liver tumors or tumor in other anatomic locations. In addition, the hypodensity of some liver tumors can be similar that created by water expansion and thermal damage, presenting a challenge to discriminating an ablation zones from residual tumor. Since our method will eventually be applied in clinics, additional evaluation in tumor models and patients is needed. Texture analysis and feature extraction techniques have matured recently. Several advanced image features which could help to discriminate the region with high and low intensity variance might also be beneficial in discriminate ablation zone and tumor region.

The present study only built a model of ablation growth for one power setting and two different durations. Since the size ablation volume highly depends on the power and duration, our model, therefore, become unavailable for ablation with other setting. More models with different settings are needed to acquire better predicted results. In addition, analyzing and comparing models between different power and duration setting could be beneficial to find out general relationship among growth rate, power and duration, which could contribute to understanding the biomechanism of ablation and provide a sufficient model for treatment planning.

Bibliography

[1] R. Siegel, D. Naishadham, and A. Jemal, “Cancer Statistics , 2017,” *CA Cancer J Clin*, vol. 67, no. 1, pp. 7–30, 2017.

[2] media centre WHO, “cancer fact sheet 2017,” *world Heal. Organ.*, 2017.

[3] L. A. Torre, F. Bray, R. L. Siegel, J. Ferlay, J. Lortet-tieulent, and A. Jemal, “Global Cancer Statistics, 2012,” *CA a cancer J. Clin.*, vol. 65, no. 2, pp. 87–108, 2015.

[4] IARC and I. A. for R. on Cancer, “World Cancer Report 2014,” 2014.

[5] H. Kuper, H.-O. Adami, and P. Boffetta, “Tobacco use, cancer causation and public health impact.,” *J. Intern. Med.*, vol. 251, no. 6, pp. 455–66, Jun. 2002.

[6] A. J. Sasco, M. B. Secretan, and K. Straif, “Tobacco smoking and cancer: a brief review of recent epidemiological evidence,” *Lung Cancer*, vol. 45, pp. S3–S9, Aug. 2004.

[7] M. J. Thun *et al.*, “Lung cancer occurrence in never-smokers: An analysis of 13 cohorts and 22 cancer registry studies,” *PLoS Med.*, vol. 5, no. 9, pp. 1357–1371, Sep. 2008.

[8] P. Anand *et al.*, “Cancer is a preventable disease that requires major lifestyle changes,” *Pharmaceutical Research*, vol. 25, no. 9. Springer, pp. 2097–2116, Sep-2008.

[9] W. T. LONDON and K. A. MCGLYNN, “Liver Cancer,” in *Cancer Epidemiology and Prevention*, Oxford University Press, 2006, pp. 763–786.

[10] F. Averhoff, “Centers for Disease Control and Prevention: Hepatitis B,” in *CDC Yellow Book*, 2016.

[11] S. F. Altekruse, K. A. McGlynn, and M. E. Reichman, “Hepatocellular Carcinoma Incidence, Mortality, and Survival Trends in the United States From 1975 to 2005,” *J. Clin. Oncol.*, vol. 27, no. 9, pp. 1485–1491, Mar. 2009.

[12] S. Mittal and H. B. El-Serag, “Epidemiology of Hepatocellular Carcinoma,” *J. Clin. Gastroenterol.*, vol. 47, pp. S2–S6, Jul. 2013.

[13] “Cancer Facts and Figures 2017,” *Am. Cancer Soc.*, 2017.

[14] V. Kumar, A. K. Abbas, J. C. Aster, and J. A. Perkins, *Robbins and Cotran pathologic basis of disease*. .

[15] A. M. Di Bisceglie, “Hepatitis B and hepatocellular carcinoma,” *Hepatology*, vol. 49, no. SUPPL. 5, pp. S56-60, May 2009.

[16] N. Goossens and Y. Hoshida, “Hepatitis C virus-induced hepatocellular carcinoma.,” *Clin. Mol. Hepatol.*, vol. 21, no. 2, pp. 105–114, 2015.

[17] A. G. Singal, A. Pillai, and J. Tiro, “Early Detection, Curative Treatment, and Survival Rates for Hepatocellular Carcinoma Surveillance in Patients with Cirrhosis: A Meta-analysis,” *PLoS Med.*, vol. 11, no. 4, p. e1001624, Apr. 2014.

[18] H. B. El-Serag, “Hepatocellular carcinoma,” *N. Engl. J. Med.*, vol. 365, no. 12, pp. 1118–27, Sep. 2011.

[19] H. B. El-Serag, “Epidemiology of viral hepatitis and hepatocellular carcinoma,” *Gastroenterology*, vol. 142, no. 6. NIH Public Access, p. 1264–1273.e1, May-2012.

[20] M. Delhaye *et al.*, “Relationship between hepatocyte proliferative activity and liver functional reserve in human cirrhosis,” *Hepatology*, vol. 23, no. 5, pp. 1003–1011, May 1996.

[21] F. Caillot *et al.*, “Transient and etiology-related transcription regulation in cirrhosis prior to hepatocellular carcinoma occurrence,” *World J. Gastroenterol.*, vol. 15, no. 3, pp. 300–309, Jan. 2009.

[22] A. J. Sanyal, S. K. Yoon, and R. Lencioni, “The etiology of hepatocellular carcinoma and

consequences for treatment.," *Oncologist*, vol. 15 Suppl 4, no. suppl 4, pp. 14–22, 2010.

[23] A. Teufel *et al.*, "Hepatocellular carcinoma in patients with autoimmune hepatitis," *World J. Gastroenterol.*, vol. 15, no. 5, pp. 578–582, Feb. 2009.

[24] M. S. Ascha, I. A. Hanouneh, R. Lopez, T. A.-R. Tamimi, A. F. Feldstein, and N. N. Zein, "The incidence and risk factors of hepatocellular carcinoma in patients with nonalcoholic steatohepatitis.," *Hepatology*, vol. 51, no. 6, pp. 1972–1978, Jun. 2010.

[25] H. O. Adami *et al.*, "Alcoholism and liver cirrhosis in the etiology of primary liver cancer," *Int. J. Cancer*, vol. 51, no. 6, pp. 898–902, Jul. 1992.

[26] H. Kuper *et al.*, "The risk of liver and bile duct cancer in patients with chronic viral hepatitis, alcoholism, or cirrhosis.," *Hepatology*, vol. 34, no. 4 Pt 1, pp. 714–718, Oct. 2001.

[27] H. T. Sørensen *et al.*, "Risk of liver and other types of cancer in patients with cirrhosis: A nationwide cohort study in Denmark," *Hepatology*, vol. 28, no. 4 I, pp. 921–925, Oct. 1998.

[28] M. A. Serra, A. Escudero, F. Rodríguez, J. A. del Olmo, and J. M. Rodrigo, "Effect of Hepatitis C Virus Infection and Abstinence From Alcohol on Survival in Patients With Alcoholic Cirrhosis," *J. Clin. Gastroenterol.*, vol. 36, no. 2, pp. 170–174, Feb. 2003.

[29] H. Miyakawa, N. Izumi, F. Marumo, and C. Sato, "Roles of alcohol, hepatitis virus infection, and gender in the development of hepatocellular carcinoma in patients with liver cirrhosis," *Alcohol. Exp. Res.*, vol. 20, no. 1, pp. A91--A94, Feb. 1996.

[30] S. Uetake, M. Yamauchi, S. Itoh, O. Kawashima, K. Takeda, and M. Ohata, "Analysis of risk factors for hepatocellular carcinoma in patients with HBs antigen- and anti-HCV antibody-negative alcoholic cirrhosis: clinical significance of prior hepatitis B virus infection.," *Alcohol. Clin. Exp. Res.*, vol. 27, no. 8 Suppl, p. 47S–51S, Aug. 2003.

[31] G. Fattovich, T. Stroffolini, I. Zagni, and F. Donato, "Hepatocellular carcinoma in cirrhosis:

Incidence and risk factors," *Gastroenterology*, vol. 127, no. 5, pp. S35–S50, 2004.

[32] IARC, "Overall evaluations of carcinogenicity: an updating of IARC Monographs Volumes 1 to 42," *IARC Monogr. Eval. Carcinog. Risk Chem. Hum.*, vol. 1–42, no. Supplement 7, p. 64, 1987.

[33] E. C. Miller and J. A. Miller, "Liver Microsomal Metabolism of Aflatoxin B 1to a Reactive Derivative Toxic to Salmonella typhimurium TA 15301," *Cancer Res.*, vol. 32, no. 10, pp. 2058–2066, Oct. 1972.

[34] F. X. Bosch, J. Ribes, M. D??az, and R. Cl??ries, "Primary liver cancer: Worldwide incidence and trends," in *Gastroenterology*, 2004, vol. 127, no. SUPPL., pp. S5–S16.

[35] A. Ananthakrishnan, V. Gogineni, and K. Saeian, "Epidemiology of Primary and Secondary Liver Cancers," *Semin. Intervent. Radiol.*, vol. 23, no. 1, pp. 47–63, Mar. 2006.

[36] Steven H. Itzkowitz and Jonathan Potack, *Sleisenger and Fordtran's gastrointestinal and liver disease pathophysiology, diagnosis, management.* Saunders/Elsevier, 2010.

[37] Y. Fong, L. H. Blumgart, and A. M. Cohen, "Surgical treatment of colorectal metastases to the liver," *CA. Cancer J. Clin.*, vol. 45, no. 1, pp. 50–62, Jan. 1995.

[38] J. P. Ayoub, K. R. Hess, M. C. Abbruzzese, R. Lenzi, M. N. Raber, and J. L. Abbruzzese, "Unknown primary tumors metastatic to liver.," *J. Clin. Oncol.*, vol. 16, no. 6, pp. 2105–2112, Jun. 1998.

[39] A. L. Hoe, G. T. Royle, and I. Taylor, "Breast liver metastases--incidence, diagnosis and outcome.," *J. R. Soc. Med.*, vol. 84, no. 12, pp. 714–6, Dec. 1991.

[40] S. H. Teh *et al.*, "Risk Factors for Mortality After Surgery in Patients With Cirrhosis," *Gastroenterology*, vol. 132, no. 4, pp. 1261–1269, 2007.

[41] L. S. Friedman, "The risk of surgery in patients with liver disease.," *Hepatology*, vol. 29,

no. 6, pp. 1617–1623, 1999.

[42] T. Patel, “Surgery in the Patient With Liver Disease,” *Mayo Clin. Proc.*, vol. 74, no. 6, pp. 593–599, 1999.

[43] S. Wilhelm *et al.*, “Discovery and development of sorafenib: a multikinase inhibitor for treating cancer.,” *Nat. Rev. Drug Discov.*, vol. 5, no. 10, pp. 835–844, 2006.

[44] D. H. Palmer, “Sorafenib in advanced hepatocellular carcinoma.,” *N. Engl. J. Med.*, vol. 359, no. 23, p. 2498; author reply 2498-2499, 2008.

[45] S. N. Goldberg, “Radiofrequency tumor ablation: Principles and techniques,” *European Journal of Ultrasound*, vol. 13, no. 2. pp. 129–147, 2001.

[46] C. J. Simon, D. E. Dupuy, and W. W. Mayo-Smith, “Microwave ablation: principles and applications.,” *Radiographics*, vol. 25 Suppl 1, pp. S69-83, 2005.

[47] C. Brace, “Thermal tumor ablation in clinical use,” *Pulse, IEEE*, no. OCTOBER, 2011.

[48] S. Rossi *et al.*, “Percutaneous RF interstitial thermal ablation in the treatment of hepatic cancer.,” *AJR. Am. J. Roentgenol.*, vol. 167, no. 3, pp. 759–768, 1996.

[49] D. Haemmerich, “Biophysics of radiofrequency ablation.,” *Crit. Rev. Biomed. Eng.*, vol. 38, no. 1, pp. 53–63, 2010.

[50] C. L. Brace, “Microwave tissue ablation: biophysics, technology, and applications.,” *Crit. Rev. Biomed. Eng.*, vol. 38, no. 1, pp. 65–78, Jan. 2010.

[51] C. L. Brace, “Radiofrequency and Microwave Ablation of the Liver, Lung, Kidney, and Bone: What Are the Differences?,” *Curr. Probl. Diagn. Radiol.*, vol. 38, no. 3, pp. 135–143, 2009.

[52] S. Goldberg, “Thermal ablation therapy for focal malignancy: a unified approach to underlying principles, techniques, and diagnostic imaging guidance,” *Am. J. ...*, no.

February, pp. 323–331, 2000.

[53] C. Rieder *et al.*, “Automatic Alignment of Pre- and Post-Interventional Liver CT Images for Assessment of Radiofrequency Ablation,” p. 83163E–83163E–8, Feb. 2012.

[54] D. E. Dupuy and S. N. Goldberg, “Image-guided Radiofrequency Tumor Ablation: Challenges and Opportunities—Part II,” *J. Vasc. Interv. Radiol.*, vol. 12, no. 10, pp. 1135–1148, 2001.

[55] M.-D. Lu *et al.*, “Percutaneous microwave and radiofrequency ablation for hepatocellular carcinoma: a retrospective comparative study.,” *J. Gastroenterol.*, vol. 40, no. 11, pp. 1054–60, Nov. 2005.

[56] G. Abbas, A. Pennathur, R. J. Landreneau, and J. D. Luketich, “Radiofrequency and microwave ablation of lung tumors,” *Journal of Surgical Oncology*, vol. 100, no. 8. pp. 645–650, 15-Dec-2009.

[57] K. Hong and C. Georgiades, “Radiofrequency ablation: Mechanism of action and devices,” *Journal of Vascular and Interventional Radiology*, vol. 21, no. SUPPL. 8. pp. S179–S186, Aug-2010.

[58] M. H. Seegenschmiedt, L. W. Brady, and R. Sauer, “Interstitial thermoradiotherapy: review on technical and clinical aspects.,” *Am. J. Clin. Oncol.*, vol. 13, no. 4, pp. 352–63, Aug. 1990.

[59] T. R. Larson, D. G. Bostwick, and A. Corica, “Temperature-correlated histopathologic changes following microwave thermoablation of obstructive tissue in patients with benign prostatic hyperplasia,” *Urology*, vol. 47, no. 4, pp. 463–469, Apr. 1996.

[60] E. M. Knavel and C. L. Brace, “Tumor ablation: common modalities and general practices.,” *Tech. Vasc. Interv. Radiol.*, vol. 16, no. 4, pp. 192–200, Dec. 2013.

[61] J. L. Hinshaw, M. G. Lubner, T. J. Ziemlewicz, F. T. Lee, and C. L. Brace, “Percutaneous Tumor Ablation Tools: Microwave, Radiofrequency, or Cryoablation—What Should You Use and Why?,” *RadioGraphics*, vol. 34, no. 5, pp. 1344–1362, Sep. 2014.

[62] S. N. Goldberg, G. S. Gazelle, L. Solbiati, W. J. Rittman, and P. R. Mueller, “Radiofrequency tissue ablation: increased lesion diameter with a perfusion electrode.,” *Acad. Radiol.*, vol. 3, no. 8, pp. 636–44, Aug. 1996.

[63] S. N. Goldberg *et al.*, “Large-volume tissue ablation with radio frequency by using a clustered, internally cooled electrode technique: laboratory and clinical experience in liver metastases.,” *Radiology*, vol. 209, no. 2, pp. 371–379, Nov. 1998.

[64] C. L. Brace, P. F. Laeseke, L. A. Sampson, T. M. Frey, R. Mukherjee, and F. T. Lee, “Radiofrequency ablation with a high-power generator: device efficacy in an in vivo porcine liver model.,” *Int. J. Hyperthermia*, vol. 23, no. June, pp. 387–394, Jan. 2007.

[65] M. G. Lubner, C. L. Brace, L. J. Hinshaw, and F. T. J. Lee, “Microwave Tumor Ablation: Mechanism of Action, Clinical Results and Devices,” *J. Vasc. Interv. Radiol.*, vol. 21, pp. S192–S203, 2011.

[66] M. Ahmed, C. L. Brace, F. T. Lee, and S. N. Goldberg, “Principles of and Advances in Percutaneous Ablation,” *Radiology*, vol. 258, no. 2, pp. 351–369, 2011.

[67] L. S. Poulou, E. Botsa, I. Thanou, P. D. Ziakas, and L. Thanos, “Percutaneous microwave ablation vs radiofrequency ablation in the treatment of hepatocellular carcinoma,” *World Journal of Hepatology*, vol. 7, no. 8. Baishideng Publishing Group Inc, pp. 1054–1063, 18-May-2015.

[68] K. F. Chu and D. E. Dupuy, “Thermal ablation of tumours: biological mechanisms and advances in therapy.,” *Nat. Rev. Cancer*, vol. 14, no. 3, pp. 199–208, 2014.

[69] S. Yılmaz *et al.*, “Use of cryoablation beyond the prostate.,” *Insights Imaging*, vol. 7, no. 2, pp. 223–32, Apr. 2016.

[70] K. D. Song, “Percutaneous cryoablation for hepatocellular carcinoma.,” *Clin. Mol. Hepatol.*, vol. 22, no. 4, pp. 509–515, Dec. 2016.

[71] >Gail ter Haar and C. Coussios, “High intensity focused ultrasound: Physical principles and devices,” *Int. J. Hyperth.*, vol. 23, no. 2, pp. 89–104, Mar. 2007.

[72] T. A. Leslie and J. E. Kennedy, “High-intensity focused ultrasound principles, current uses, and potential for the future.,” *Ultrasound Q.*, vol. 22, no. 4, pp. 263–272, Dec. 2006.

[73] N. M. Hijnen, a Elevelt, and H. Grull, “Stability and trapping of magnetic resonance imaging contrast agents during high-intensity focused ultrasound ablation therapy,” *Invest. Radiol.*, vol. 48, no. 7, pp. 517–524, 2013.

[74] A. Tezel and S. Mitragotri, “Interactions of inertial cavitation bubbles with stratum corneum lipid bilayers during low-frequency sonophoresis.,” *Biophys. J.*, vol. 85, no. 6, pp. 3502–3512, 2003.

[75] E. M. Knavel and C. L. Brace, “Tumor ablation: Common modalities and general practices,” *Techniques in Vascular and Interventional Radiology*, vol. 16, no. 4. NIH Public Access, pp. 192–200, Dec-2013.

[76] J.-J. Li *et al.*, “Complications of high intensity focused ultrasound in patients with recurrent and metastatic abdominal tumors.,” *World J. Gastroenterol.*, vol. 13, no. 19, pp. 2747–2751, May 2007.

[77] Y. Kim, H. Rhim, M. J. Choi, H. K. Lim, and D. Choi, “High-intensity focused ultrasound therapy: an overview for radiologists.,” *Korean J. Radiol.*, vol. 9, no. 4, pp. 291–302, 2008.

[78] R. Stollberger, P. W. Ascher, D. Huber, W. Renhart, H. Radner, and F. Ebner, “Temperature

monitoring of interstitial thermal tissue coagulation using MR phase images," *J. Magn. Reson. Imaging*, vol. 8, no. 1, pp. 188–196, 1998.

[79] R. Puls *et al.*, "Laser Ablation of Liver Metastases from Colorectal Cancer with MR Thermometry: 5-Year Survival," *J. Vasc. Interv. Radiol.*, vol. 20, no. 2, pp. 225–234, 2009.

[80] M. G. Skinner, M. N. Iizuka, M. C. Kolios, and M. D. Sherar, "A theoretical comparison of energy sources - microwave, ultrasound and laser - for interstitial thermal therapy," *Phys. Med. Biol.*, vol. 43, no. 12, pp. 3535–3547, Dec. 1998.

[81] A. C. Steger, W. R. Lees, P. Shorvon, K. Walmsley, and S. G. Bown, "Multiple fibre low power interstitial laser hyperthermia: studies in the normal liver," *Br. J. Surg.*, vol. 79, no. 2, pp. 139–145, 1992.

[82] L. M. Veenendaal, A. de Jager, G. Stapper, I. H. M. Borel Rinkes, and R. van Hillegersberg, "Multiple fiber laser-induced thermotherapy for ablation of large intrahepatic tumors.," *Photomed. Laser Surg.*, vol. 24, no. 1, pp. 3–9, Feb. 2006.

[83] M. R. Oliva and S. Saini, "Liver cancer imaging: Role of CT, MRI, US and PET," *Cancer Imaging*, vol. 4, no. Spec No A, pp. S42–S46, Apr. 2004.

[84] J. T. De Sanctis, S. N. Goldberg, and P. R. Mueller, "Percutaneous treatment of hepatic neoplasms: A review of current techniques.," *Cardiovasc. Intervent. Radiol.*, vol. 21, no. 4, pp. 273–296, 1998.

[85] C. H. Cha *et al.*, "CT versus sonography for monitoring radiofrequency ablation in a porcine liver.," *AJR. Am. J. Roentgenol.*, vol. 175, no. 3, pp. 705–11, Sep. 2000.

[86] H. Wu, L. R. Wilkins, N. P. Ziats, J. R. Haaga, and A. A. Exner, "Real-time monitoring of radiofrequency ablation and postablation assessment: accuracy of contrast-enhanced US in experimental rat liver model.," *Radiology*, vol. 270, no. 1, pp. 107–16, Jan. 2014.

[87] M. Lepetit-Coiff?? *et al.*, “Real-time monitoring of radiofrequency ablation of rabbit liver by respiratory-gated quantitative temperature MRI,” *J. Magn. Reson. Imaging*, vol. 24, no. 1, pp. 152–159, Jul. 2006.

[88] B. Quesson *et al.*, “Real-time volumetric MRI thermometry of focused ultrasound ablation in vivo: A feasibility study in pig liver and kidney,” *NMR Biomed.*, vol. 24, no. 2, pp. 145–153, Feb. 2011.

[89] A. B. Holbrook, J. M. Santos, E. Kaye, V. Rieke, and K. B. Pauly, “Real-time MR thermometry for monitoring HIFU ablations of the liver,” *Magn. Reson. Med.*, vol. 63, no. 2, pp. 365–373, Feb. 2010.

[90] M. Lepetit-Coiffé *et al.*, “Real-time monitoring of radiofrequency ablation of liver tumors using thermal-dose calculation by MR temperature imaging: initial results in nine patients, including follow-up.,” *Eur. Radiol.*, vol. 20, no. 1, pp. 193–201, Jan. 2010.

[91] P. F. Hahn, G. S. Gazelle, D. Y. Jiang, C. C. Compton, S. N. Goldberg, and P. R. Mueller, “Liver tumor ablation: real-time monitoring with dynamic CT.,” *Acad. Radiol.*, vol. 4, no. 9, pp. 634–638, 1997.

[92] Z.-W. Peng *et al.*, “Risk factors of survival after percutaneous radiofrequency ablation of hepatocellular carcinoma.,” *Surg. Oncol.*, vol. 17, no. 1, pp. 23–31, Jul. 2008.

[93] T. M. Robinson, “BASIC PRINCIPLES OF ULTRASOUND,” in *Vascular Imaging of the Central Nervous System*, vol. 240, Oxford, UK: John Wiley & Sons, Ltd, 2007, pp. 101–110.

[94] E. Spaeth, A. Melzer, and M. O. Schurr, “Principles of ultrasound imaging,” *Endosc. Surg. Allied Technol.*, vol. 2, no. 2, pp. 161–163, Apr. 1994.

[95] “University of Manitoba - Information Services and Technology - Ultrasound Imaging

Overview.” [Online]. Available: http://umanitoba.ca/faculties/health_sciences/medicine/units/cacs/sam/8478.html. [Accessed: 05-May-2017].

[96] U. M. Hamper, S. Sheth, F. M. Abbas, N. B. Rosenshein, D. Aronson, and R. J. Kurman, “Transvaginal color Doppler sonography of adnexal masses: differences in blood flow impedance in benign and malignant lesions.,” *AJR. Am. J. Roentgenol.*, vol. 160, no. 6, pp. 1225–1228, Jun. 1993.

[97] S. Tanaka, T. Kitamura, M. Fujita, K. Nakanishi, and S. Okuda, “Color Doppler flow imaging of liver tumors.,” *AJR. Am. J. Roentgenol.*, vol. 154, no. 3, pp. 509–14, Mar. 1990.

[98] D. Choi *et al.*, “Hepatocellular carcinoma treated with percutaneous radio-frequency ablation: usefulness of power Doppler US with a microbubble contrast agent in evaluating therapeutic response-preliminary results.,” *Radiology*, vol. 217, no. 2, pp. 558–63, Nov. 2000.

[99] O. Rouvière *et al.*, “Evaluation of Color Doppler in Guiding Prostate Biopsy after HIFU Ablation,” *Eur. Urol.*, vol. 50, no. 3, pp. 490–497, 2006.

[100] M. F. Meloni *et al.*, “Hepatocellular carcinoma treated with radiofrequency ablation: Comparison of pulse inversion contrast-enhanced harmonic sonography, contrast-enhanced power Doppler sonography, and helical CT,” *Am. J. Roentgenol.*, vol. 177, no. 2, pp. 375–380, Aug. 2001.

[101] S. Rossi *et al.*, “Contrast-enhanced versus conventional and color doppler sonography for the detection of thrombosis of the portal and hepatic venous systems,” *Am. J. Roentgenol.*, vol. 186, no. 3, pp. 763–773, Mar. 2006.

[102] R. J. Dewall, T. Varghese, and C. L. Brace, “Visualizing ex vivo radiofrequency and

microwave ablation zones using electrode vibration elastography.," *Med. Phys.*, vol. 39, no. 11, pp. 6692–700, Nov. 2012.

[103] B. Arnal, W.-N. Lee, M. Pernot, M. Fink, and M. Tanter, "Monitoring the lesion formation during histotripsy treatment using shear wave imaging," *12Th Int. Symp. Ther. Ultrasound*, vol. 129, no. 2012, pp. 129–134, 2012.

[104] K. Sugimoto, H. Oshiro, S. Ogawa, M. Honjo, T. Hara, and F. Moriyasu, "Radiologic-pathologic correlation of three-dimensional shear-wave elastographic findings in assessing the liver ablation volume after radiofrequency ablation," *World J. Gastroenterol.*, vol. 20, no. 33, pp. 11850–11855, Sep. 2014.

[105] a. Mariani *et al.*, "Real time shear waves elastography monitoring of thermal ablation: In vivo evaluation in pig livers," *J. Surg. Res.*, vol. 188, no. 1, pp. 37–43, 2014.

[106] R. J. Dewall, T. Varghese, and E. L. Madsen, "Shear wave velocity imaging using transient electrode perturbation: Phantom and ex vivo validation," *IEEE Trans. Med. Imaging*, vol. 30, no. 3, pp. 666–678, Mar. 2011.

[107] R. J. DeWall and T. Varghese, "Improving thermal ablation delineation with electrode vibration elastography using a bidirectional wave propagation assumption," in *IEEE International Ultrasonics Symposium, IUS*, 2011, vol. 59, no. 1, pp. 2412–2415.

[108] P.-H. Tsui, C.-Y. Wang, Z. Zhou, and Y.-L. Wan, "Monitoring Radiofrequency Ablation Using Ultrasound Envelope Statistics and Shear Wave Elastography in the Periablation Period: An In Vitro Feasibility Study," *PLoS One*, vol. 11, no. 9, p. e0162488, 2016.

[109] J. L. Gennisson, T. Deffieux, M. Fink, and M. Tanter, "Ultrasound elastography: Principles and techniques," *Diagn. Interv. Imaging*, vol. 94, no. 5, pp. 487–495, 2013.

[110] Z. Zhou, S. Wu, C.-Y. Wang, H.-Y. Ma, C.-C. Lin, and P.-H. Tsui, "Monitoring

Radiofrequency Ablation Using Real-Time Ultrasound Nakagami Imaging Combined with Frequency and Temporal Compounding Techniques," *PLoS One*, vol. 10, no. 2, p. e0118030, 2015.

[111] M. L. Li, D. W. Li, H. L. Liu, and M. S. Lin, "Ultrasonic Nakagami visualization of HIFU-induced thermal lesions," in *Proceedings - IEEE Ultrasonics Symposium*, 2010, pp. 2251–2253.

[112] S. Zhang, C. Li, F. Zhou, M. Wan, and S. Wang, "Enhanced Lesion-to-Bubble Ratio on Ultrasonic Nakagami Imaging for Monitoring of High-Intensity Focused Ultrasound," *J. Ultrasound Med.*, vol. 33, no. 6, pp. 959–970, Jun. 2014.

[113] P. Rangraz, H. Behnam, and J. Tavakkoli, "Nakagami imaging for detecting thermal lesions induced by high-intensity focused ultrasound in tissue.," *Proc. Inst. Mech. Eng. H.*, vol. 228, no. 1, pp. 19–26, Jan. 2014.

[114] S. Zhang *et al.*, "Feasibility of using Nakagami distribution in evaluating the formation of ultrasound-induced thermal lesions," *J. Acoust. Soc. Am.*, vol. 131, no. 6, pp. 4836–4844, Jun. 2012.

[115] P. Mohana Shankar, "A general statistical model for ultrasonic backscattering from tissues.," *IEEE Trans. Ultrason. Ferroelectr. Freq. Control*, vol. 47, no. 3, pp. 727–736, May 2000.

[116] P. H. Tsui and C. C. Chang, "Imaging Local Scatterer Concentrations by the Nakagami Statistical Model," *Ultrasound Med. Biol.*, vol. 33, no. 4, pp. 608–619, 2007.

[117] M. A. Lewis, R. M. Strauch, and R. Chopra, "Thermometry and Ablation Monitoring with Ultrasound," *Int. J. Hyperth.*, vol. 31, no. 2, pp. 229–262, 2015.

[118] T. Varghese *et al.*, "Ultrasound monitoring of temperature change during radiofrequency ablation: Preliminary in-vivo results," *Ultrasound Med. Biol.*, vol. 28, no. 3, pp. 321–329,

2002.

[119] G. Mauri *et al.*, “Intraprocedural contrast-enhanced ultrasound (CEUS) in liver percutaneous radiofrequency ablation: Clinical impact and health technology assessment,” *Insights Imaging*, vol. 5, no. 2, pp. 209–216, Apr. 2014.

[120] L. Solbiati, T. Ierace, M. Tonolini, and L. Cova, “Guidance and monitoring of radiofrequency liver tumor ablation with contrast-enhanced ultrasound,” *European Journal of Radiology*, vol. 51, no. SUPPL. pp. S19–S23, 2004.

[121] T. K. Kim, K. Khalili, and H.-J. Jang, “Local ablation therapy with contrast-enhanced ultrasonography for hepatocellular carcinoma: a practical review.,” *Ultrason. (Seoul, Korea)*, vol. 34, no. 4, pp. 235–245, Jun. 2015.

[122] J. Y. Wu *et al.*, “Role of contrast enhanced ultrasound in radiofrequency ablation of metastatic liver carcinoma,” *Chinese J. Cancer Res.*, vol. 24, no. 1, pp. 44–51, Mar. 2012.

[123] M. Lu *et al.*, “Comparison of contrast enhanced ultrasound and contrast enhanced CT or MRI in monitoring percutaneous thermal ablation procedure in patients with hepatocellular carcinoma: a multi-center study in China.,” *Ultrasound Med. Biol.*, vol. 33, no. 11, pp. 1736–49, Nov. 2007.

[124] A. C. A. C. Kak and M. Slaney, “Principles of computerized tomographic imaging,” *Engineering*, 1988.

[125] Sigurdur Helgason, “Radon Transform Second Edition,” p. 190, 1999.

[126] S. Deans, *The Radon Transform and Some of Its Applications*. Krieger Pub. Co, 1983.

[127] P. Limanond, P. Zimmerman, S. S. Raman, B. M. Kadell, and D. S. K. Lu, “Interpretation of CT and MRI after Radiofrequency Ablation of Hepatic Malignancies,” *Am. J. Roentgenol.*, vol. 181, no. 6, pp. 1635–1640, Dec. 2003.

[128] F. Agnello *et al.*, “Imaging appearance of treated hepatocellular carcinoma,” *World J. Hepatol.*, vol. 5, no. 8, pp. 417–424, Aug. 2013.

[129] W. Liu, U. Techavipoo, T. Varghese, J. A. Zagzebski, Q. Chen, and F. T. Lee, “Elastographic versus x-ray CT imaging of radio frequency ablation coagulations: an in vitro study.,” *Med Phys*, vol. 31, no. 6, pp. 1322–1332, May 2004.

[130] T. Jiang, A. X. Zhu, and D. V. Sahani, “Established and novel imaging biomarkers for assessing response to therapy in hepatocellular carcinoma,” *Journal of Hepatology*, vol. 58, no. 1. pp. 169–177, 2013.

[131] N. I. Sainani, D. A. Gervais, P. R. Mueller, and R. S. Arellano, “Imaging after percutaneous radiofrequency ablation of hepatic tumors: Part 1, normal findings,” *American Journal of Roentgenology*, vol. 200, no. 1. American Roentgen Ray Society, pp. 184–193, Jan-2013.

[132] C. Schraml *et al.*, “Diagnostic performance of contrast-enhanced computed tomography in the immediate assessment of radiofrequency ablation success in colorectal liver metastases,” *Abdom. Imaging*, vol. 33, no. 6, pp. 643–651, 2008.

[133] M. A. Farrell *et al.*, “Imaging-Guided Radiofrequency Ablation of Solid Renal Tumors,” *Am. J. Roentgenol.*, vol. 180, no. 6, pp. 1509–1513, Jun. 2003.

[134] K. Hegenscheid *et al.*, “Assessing early vascular changes and treatment response after laser-induced thermotherapy of pulmonary metastases with perfusion CT: Initial experience,” *Am. J. Roentgenol.*, vol. 194, no. 4, pp. 1116–1123, Apr. 2010.

[135] D. Ippolito, P. A. Bonaffini, C. Capraro, D. Leni, R. Corso, and S. Sironi, “Viable residual tumor tissue after radiofrequency ablation treatment in hepatocellular carcinoma: Evaluation with CT perfusion,” *Abdom. Imaging*, vol. 38, no. 3, pp. 502–510, Jun. 2013.

[136] H. Wu, A. A. Exner, T. M. Krupka, B. D. Weinberg, R. Patel, and J. R. Haaga,

"Radiofrequency Ablation. Post-ablation Assessment Using CT Perfusion with Pharmacological Modulation in a Rat Subcutaneous Tumor Model," *Acad. Radiol.*, vol. 16, no. 3, pp. 321–331, 2009.

[137] M. R. Meijerink *et al.*, "Early Detection of Local RFA Site Recurrence Using Total Liver Volume Perfusion CT. Initial Experience," *Acad. Radiol.*, vol. 16, no. 10, pp. 1215–1222, 2009.

[138] Y. Li, G. Shi, S. Wang, S. Wang, and R. Wu, "Iodine quantification with dual-energy CT: Phantom study and preliminary experience with VX2 residual tumour in rabbits after radiofrequency ablation," *Br. J. Radiol.*, vol. 86, no. 1029, p. 20130143, Sep. 2013.

[139] S. H. Lee *et al.*, "Dual-energy computed tomography to assess tumor response to hepatic radiofrequency ablation: potential diagnostic value of virtual noncontrast images and iodine maps.," *Invest. Radiol.*, vol. 46, no. 2, pp. 77–84, Feb. 2011.

[140] S. Y. Park, C. K. Kim, and B. K. Park, "Dual-energy CT in assessing therapeutic response to radiofrequency ablation of renal cell carcinomas," *Eur. J. Radiol.*, vol. 83, no. 2, pp. e73–e79, 2014.

[141] G. D. Pandeya, M. J. W. Greuter, B. Schmidt, T. Flohr, and M. Oudkerk, "Assessment of thermal sensitivity of CT during heating of liver: An ex vivo study," *Br. J. Radiol.*, vol. 85, no. 1017, pp. 661–665, 2012.

[142] E. Schena *et al.*, "Monitoring of temperature increase and tissue vaporization during laser interstitial thermotherapy of ex vivo swine liver by computed tomography," pp. 378–381, 2013.

[143] E. Schena *et al.*, "Experimental assessment of CT-based thermometry during laser ablation of porcine pancreas.," *Phys. Med. Biol.*, vol. 58, pp. 5705–16, 2013.

[144] P. Bruners *et al.*, “CT-based temperature monitoring during hepatic RF ablation: Feasibility in an animal model,” *Int. J. Hyperth.*, vol. 28, no. 1, pp. 55–61, 2012.

[145] Y.-C. N. Cheng and E. M. Haacke, *Magnetic Resonance Imaging*, vol. 53, no. 9. Chichester, UK: John Wiley & Sons Ltd, 2014.

[146] N. Lee and T. Hyeon, “Designed synthesis of uniformly sized iron oxide nanoparticles for efficient magnetic resonance imaging contrast agents,” *Chem. Soc. Rev.*, vol. 41, no. 7, pp. 2575–2589, 2012.

[147] N. Wakui *et al.*, “A case of poorly differentiated hepatocellular carcinoma with intriguing ultrasonography findings,” *Oncol. Lett.*, vol. 4, no. 3, pp. 393–397, 2012.

[148] G. C. Stewart C. Bushong, “Magnetic Resonance Imaging: Physical and Biological Principles,” 2013.

[149] N. J. McDannold and F. A. Jolesz, “Magnetic resonance image-guided thermal ablations.,” *Top. Magn. Reson. imaging*, vol. 11, no. 3, pp. 191–202, 2000.

[150] R. Lencioni, D. Cioni, and C. Bartolozzi, “Percutaneous radiofrequency thermal ablation of liver malignancies: Techniques, indications, imaging findings, and clinical results,” *Abdominal Imaging*, vol. 26, no. 4. Springer-Verlag, pp. 345–360, Jul-2001.

[151] C. F. G. C. Geraldes and S. Laurent, “Classification and basic properties of contrast agents for magnetic resonance imaging.,” *Contrast Media Mol. Imaging*, vol. 4, no. 1, pp. 1–23, Jan. 2009.

[152] B. D. Senneville, C. Mougenot, B. Quesson, I. Dragonu, N. Grenier, and C. T. W. Moonen, “MR thermometry for monitoring tumor ablation,” *Eur. Radiol.*, vol. 17, no. 9, pp. 2401–2410, 2007.

[153] V. Rieke *et al.*, “Referenceless MR thermometry for monitoring thermal ablation in the

prostate," *IEEE Trans. Med. Imaging*, vol. 26, no. 6, pp. 813–821, Jun. 2007.

[154] V. Rieke and K. B. Pauly, "MR thermometry," *Journal of Magnetic Resonance Imaging*, vol. 27, no. 2. Wiley Subscription Services, Inc., A Wiley Company, pp. 376–390, Feb-2008.

[155] L. Winter *et al.*, "Magnetic resonance thermometry: Methodology, pitfalls and practical solutions.," *Int. J. Hyperth.*, vol. 6736, no. January, pp. 1–13, 2015.

[156] C. Weidensteiner *et al.*, "Real-time MR temperature mapping of rabbit liver in vivo during thermal ablation.," *Magn. Reson. Med.*, vol. 50, no. 2, pp. 322–30, Aug. 2003.

[157] K. K. Vigen, J. Jarrard, V. Rieke, J. Frisoli, B. L. Daniel, and K. B. Pauly, "In vivo porcine liver radiofrequency ablation with simultaneous MR temperature imaging," *J. Magn. Reson. Imaging*, vol. 23, no. 4, pp. 578–584, Apr. 2006.

[158] S. I. Ziegler, "Positron emission tomography: Principles, technology, and recent developments," *Nuclear Physics A*, vol. 752, no. 1–4 SPEC. ISS. pp. 679–687, Apr-2005.

[159] A. Berger, "How does it work? Positron emission tomography.," *BMJ*, vol. 326, no. 7404, p. 1449, Jun. 2003.

[160] F. G. Abtin, J. Eradat, A. J. Gutierrez, C. Lee, M. C. Fishbein, and R. D. Suh, "Radiofrequency Ablation of Lung Tumors: Imaging Features of the Postablation Zone," *Radiographics*, vol. 32, no. 4, pp. 947–969, Jul. 2012.

[161] N. I. Sainani, P. B. Shyn, S. Tatli, P. R. Morrison, K. Tuncali, and S. G. Silverman, "PET/CT-guided radiofrequency and cryoablation: Is tumor fluorine-18 fluorodeoxyglucose activity dissipated by thermal ablation?," *J. Vasc. Interv. Radiol.*, vol. 22, no. 3, pp. 354–360, 2011.

[162] D. A. Sahin, O. Agcaoglu, C. Chretien, A. Siperstein, and E. Berber, "The utility of PET/CT

in the management of patients with colorectal liver metastases undergoing laparascopic radiofrequency thermal ablation," *Ann. Surg. Oncol.*, vol. 19, no. 3, pp. 850–855, Mar. 2012.

[163] T. Okuma *et al.*, "18F-FDG small-animal PET for monitoring the therapeutic effect of CT-guided radiofrequency ablation on implanted VX2 lung tumors in rabbits.," *J. Nucl. Med.*, vol. 47, no. 8, pp. 1351–8, Aug. 2006.

[164] H. Kuehl *et al.*, "Comparison of FDG-PET, PET/CT and MRI for follow-up of colorectal liver metastases treated with radiofrequency ablation: Initial results," *Eur. J. Radiol.*, vol. 67, no. 2, pp. 362–371, 2008.

[165] T. Okuma *et al.*, "Fluorine-18-fluorodeoxyglucose positron emission tomography for assessment of patients with unresectable recurrent or metastatic lung cancers after CT-guided radiofrequency ablation: Preliminary results," *Ann. Nucl. Med.*, vol. 20, no. 2, pp. 115–121, Feb. 2006.

[166] J. M. Schmitt, "Optical Coherence Tomography (OCT): a review," *IEEE J. Sel. Top. Quantum Electron.*, vol. 5, no. 4, pp. 1205–1215, 1999.

[167] A. F. Fercher, W. Drexler, C. K. Hitzenberger, and T. Lasser, "Optical coherence tomography - principles and applications," *Reports Prog. Phys.*, vol. 66, no. 2, pp. 239–303, Feb. 2003.

[168] S. A. Boppart, J. M. Herrmann, C. Pitris, D. L. Stamper, M. E. Brezinski, and J. G. Fujimoto, "Real-time optical coherence tomography for minimally invasive imaging of prostate ablation," *Comput. Aided Surg.*, vol. 6, no. 2, pp. 94–103, 2001.

[169] S. A. Boppart, J. Herrmann, C. Pitris, D. L. Stamper, M. E. Brezinski, and J. G. Fujimoto, "High-Resolution Optical Coherence Tomography-Guided Laser Ablation of Surgical Tissue," *J. Surg. Res.*, vol. 82, no. 2, pp. 275–284, Apr. 1999.

[170] E. J. Hall and D. J. Brenner, “Cancer risks from diagnostic radiology,” *Br. J. Radiol.*, vol. 81, no. 965, pp. 362–378, 2008.

[171] M. Tepel, M. van der Giet, C. Schwarzfeld, U. Laufer, D. Liermann, and W. Zidek, “Prevention of radiographic-contrast-agent-induced reductions in renal function by acetylcysteine.,” *N. Engl. J. Med.*, vol. 343, no. 3, pp. 180–184, 2000.

[172] M. Andreucci, R. Solomon, and A. Tasanarong, “Side effects of radiographic contrast media: Pathogenesis, risk factors, and prevention,” *Biomed Res. Int.*, vol. 2014, 2014.

[173] M. Ahmed, C. Brace, F. L. Jr, and S. Goldberg, “Principles of and advances in percutaneous ablation,” *Radiology*, vol. 258, no. 2, pp. 351–369, 2011.

[174] A. Wright, L. Sampson, and T. Warner, “Radiofrequency versus Microwave Ablation in a Hepatic Porcine Model 1,” *Radiology*, no. 4, 2005.

[175] E. Patterson and C. Scudamore, “Radiofrequency ablation of porcine liver in vivo: effects of blood flow and treatment time on lesion size.,” *Ann. ...*, vol. 227, no. 4, pp. 559–565, 1998.

[176] T. Shibata, T. Niinobu, and N. Ogata, “Comparison of the effects of in-vivo thermal ablation of pig liver by microwave and radiofrequency coagulation,” *J. Hepatobiliary. Pancreat. Surg.*, vol. 7, no. 6, pp. 592–598, Dec. 2000.

[177] N. C. T. June, X. Cui, S. Li, H.-I. Kim, and K.-S. Kwack, “Fast and Accurate Rigid Registration of 3D CT Images by Combining Feature and Intensity,” *J. Comput. Sci. Eng.*, vol. 6, no. 1, pp. 1–11, Mar. 2012.

[178] W. J. H. Veldkamp, R. M. S. Joemai, A. J. van der Molen, and J. Geleijns, “Development and validation of segmentation and interpolation techniques in sinograms for metal artifact suppression in CT,” *Med. Phys.*, vol. 37, no. 2, p. 620, 2010.

[179] D. Garcia, “Robust smoothing of gridded data in one and higher dimensions with missing values,” *Comput. Stat. Data Anal.*, vol. 54, no. 4, pp. 1167–1178, Apr. 2010.

[180] F. E. Boas and D. Fleischmann, “CT artifacts: causes and reduction techniques,” *Imaging Med.*, vol. 4, no. 2, pp. 229–240, 2012.

[181] H. V. Nghiem *et al.*, “Computed tomography appearances of hypervascular hepatic tumors after percutaneous radiofrequency ablation therapy,” *Curr. Probl. Diagn. Radiol.*, vol. 31, no. 3, pp. 105–111, 2002.

[182] C. W. Hong, L. Chow, E. B. Turkbey, R. Lencioni, S. K. Libutti, and B. J. Wood, “Imaging Features of Radiofrequency Ablation with Heat-Deployed Liposomal Doxorubicin in Hepatic Tumors,” *Cardiovasc. Intervent. Radiol.*, 2015.

[183] T. Boskamp, D. Rinck, F. Link, B. Kümmerlen, G. Stamm, and P. Mildenberger, “New vessel analysis tool for morphometric quantification and visualization of vessels in CT and MR imaging data sets.,” *Radiographics*, vol. 24, pp. 287–297, 2004.

[184] S. Rajagopalan and A. R. Richard, “Image-based Metrology of Porous Tissue Engineering Scaffolds,” *Proc. SPIE Med. Imaging*, 2006.

[185] R. M. Rangayyan and S. G. Elkadiki, “Algorithm for the computation of region-based image edge profile acutance,” *J. Electron. Imaging*, vol. 4, no. 1, pp. 62–70, 1995.

[186] C. Feichtenhofer, H. Fassold, and P. Schallauer, “A perceptual image sharpness metric based on local edge gradient analysis,” *IEEE Signal Process. Lett.*, vol. 20, no. 4, pp. 379–382, 2013.

[187] R. Alvarez and E. Seppi, “A Comparison of Noise and Dose in Conventional and Energy Selective Computed Tomography,” *IEEE Trans. Nucl. Sci.*, vol. 26, no. 2, pp. 2853–2856, 1979.

[188] S. N. Goldberg *et al.*, "Percutaneous Radiofrequency Tissue Ablation: Does Perfusion-mediated Tissue Cooling Limit Coagulation Necrosis?," *J. Vasc. Interv. Radiol.*, vol. 9, no. 1, pp. 101–111, Jan. 1998.

[189] I. a Chang and U. D. Nguyen, "Thermal modeling of lesion growth with radiofrequency ablation devices.," *Biomed. Eng. Online*, vol. 3, no. 1, p. 27, 2004.

[190] P. Vaupel, F. Kallinowski, and P. Okunieff, "Blood flow, oxygen and nutrient supply, and metabolic microenvironment of human tumors: a review," *Cancer Res.*, pp. 6449–6465, 1989.

[191] H. Lu, I. Hsiao, and X. Li, "Noise properties of low-dose CT projections and noise treatment by scale transformations," *2001 IEEE Nucl. Sci. Symp. Conf. Rec. (Cat. No.01CH37310)*, vol. 3, pp. 1662–1666, 2002.

[192] C. a Mistretta *et al.*, "Highly constrained backprojection for time-resolved MRI.," *Magn. Reson. Med.*, vol. 55, no. 1, pp. 30–40, Jan. 2006.

[193] K. M. Johnson, J. Velikina, Y. Wu, S. Kecskemeti, O. Wieben, and C. a Mistretta, "Improved waveform fidelity using local HYPR reconstruction (HYPR LR).," *Magn. Reson. Med.*, vol. 59, no. 3, pp. 456–62, Mar. 2008.

[194] C. L. Brace, C. a Mistretta, J. L. Hinshaw, and F. T. Lee, "Periodic contrast-enhanced computed tomography for thermal ablation monitoring: a feasibility study.," *Conf. Proc. IEEE Eng. Med. Biol. Soc.*, vol. 2009, pp. 4299–302, Jan. 2009.

[195] Z. Hu, "Extraction of Any Angle Virtual Slice on 3D CT Image," *2008 Second Int. Symp. Intell. Inf. Technol. Appl.*, pp. 356–360, Dec. 2008.

[196] a P. Zijdenbos, B. M. Dawant, R. a Margolin, and a C. Palmer, "Morphometric analysis of white matter lesions in MR images: method and validation.," *IEEE Trans. Med. Imaging*,

vol. 13, no. 4, pp. 716–724, 1994.

[197] B. G. Fallone, P. R. Moran, and E. B. Podgorsak, “Noninvasive thermometry with a clinical x-ray CT scanner.,” *Med. Phys.*, vol. 9, no. 1982, pp. 715–721, 1982.

[198] S. S. Raman, D. S. K. Lu, D. J. Vodopich, J. Sayre, and C. Lassman, “Creation of radiofrequency lesions in a porcine model: Correlation with sonography, CT, and histopathology,” *Am. J. Roentgenol.*, vol. 175, no. 5, pp. 1253–1258, 2000.

[199] A. U. Hines-Peralta *et al.*, “Microwave ablation: results with a 2.45-GHz applicator in ex vivo bovine and in vivo porcine liver.,” *Radiology*, vol. 239, no. 1, pp. 94–102, 2006.

[200] Y.-S. Kim, W. J. Lee, H. Rhim, H. K. Lim, D. Choi, and J. Y. Lee, “The minimal ablative margin of radiofrequency ablation of hepatocellular carcinoma (> 2 and < 5 cm) needed to prevent local tumor progression: 3D quantitative assessment using CT image fusion.,” *AJR. Am. J. Roentgenol.*, vol. 195, no. September, pp. 758–765, 2010.

[201] G. D. I. Dodd, M. S. Frank, M. Aribandi, S. Chopra, and K. N. Chintapalli, “Radiofrequency Thermal Ablation :computer analysis of the size of thermal injury created by overlaping ablations,” *AJR. Am. J. Roentgenol.*, vol. 177, no. October, pp. 777–782, 2001.

[202] C. H. Liu, R. S. Arellano, R. N. Uppot, A. E. Samir, D. A. Gervais, and P. R. Mueller, “Radiofrequency ablation of hepatic tumours: Effect of post-ablation margin on local tumour progression,” *Eur. Radiol.*, vol. 20, no. 4, pp. 877–885, 2010.

[203] H. Rempp, R. Hoffmann, and J. Roland, “Threshold-based prediction of the coagulation zone in sequential temperature mapping in MR-guided radiofrequency ablation of liver tumours,” *Eur. ...*, 2012.

[204] H. Rempp *et al.*, “Prediction of cell necrosis with sequential temperature mapping after radiofrequency ablation.,” *J. Magn. Reson. Imaging*, vol. 30, no. 3, pp. 631–9, Sep. 2009.

[205] G. D. Pandeya, M. J. W. Greuter, K. P. de Jong, B. Schmidt, T. Flohr, and M. Oudkerk, “Feasibility of noninvasive temperature assessment during radiofrequency liver ablation on computed tomography.,” *J. Comput. Assist. Tomogr.*, vol. 35, no. 3, pp. 356–360, 2011.

[206] P. Homolka, A. Gahleitner, and R. Nowotny, “Temperature dependence of HU values for various water equivalent phantom materials.,” *Phys. Med. Biol.*, vol. 47, no. 16, pp. 2917–2923, 2002.

[207] K. Passera and S. Selvaggi, “Radiofrequency ablation of liver tumors: quantitative assessment of tumor coverage through CT image processing.,” ... *Med. imaging*, 2013.

[208] R. S. Lazebnik, M. S. Breen, J. S. Lewin, and D. L. Wilson, “Automatic model-based evaluation of magnetic resonance-guided radio frequency ablation lesions with histological correlation.,” *J. Magn. Reson. Imaging*, vol. 19, no. 2, pp. 245–54, Feb. 2004.

[209] M. Kakar and D. R. Olsen, “Automatic segmentation and recognition of lungs and lesion from CT scans of thorax,” *Comput. Med. Imaging Graph.*, vol. 33, no. 1, pp. 72–82, 2009.

[210] A. B. Bhide, P. Patil, and S. Dhande, “Brain segmentation using {F}uzzy {C} means clustering to decto tumor region,” *Int. J. Adv. Res. Comput. Sci. Electron. Eng.*, vol. 1, no. 2, pp. 85–90, 2012.

[211] S. S. Kumar, R. S. Moni, and J. Rajeesh, “Automatic liver and lesion segmentation: A primary step in diagnosis of liver diseases,” *Signal, Image Video Process.*, vol. 7, no. 1, pp. 163–172, Jan. 2013.

[212] P. J. . d Yim *et al.*, “Volumetric analysis of liver metastases in computed tomography with the fuzzy C-means algorithm,” *J. Comput. Assist. Tomogr.*, vol. 30, no. 2, pp. 212–220, 2006.

[213] S. Selvarajah, S., & Kodituwakku, “Analysis and Comparison of Texture Features for

Content Based Image Retrieval .," *Int. J. Latest Trends Comput.*, pp. 108–113, 2011.

[214] E. L. Chen, P. C. Chung, C. L. Chen, H. M. Tsai, and C. I. Chang, "An automatic diagnostic system for CT liver image classification.," *IEEE Trans. Biomed. Eng.*, vol. 45, no. 6, pp. 783–94, Jun. 1998.

[215] R. Adams and L. Bischof, "Seeded region growing," *IEEE Trans. Pattern Anal. Mach. Intell.*, vol. 16, no. 6, pp. 641–647, Jun. 1994.

[216] J. C. Bezdek, *Pattern Recognition with Fuzzy Objective Function Algorithms*, vol. 25, no. 3. Boston, MA: Springer US, 1981.

[217] M. A. Luengo-Oroz and J. Angulo, "Cyclic mathematical morphology in polar-logarithmic representation," *IEEE Trans. Image Process.*, vol. 18, no. 5, pp. 1090–1096, 2009.

[218] J. Egger *et al.*, "RFA-cut: Semi-automatic segmentation of radiofrequency ablation zones with and without needles via optimal s-t-cuts," in *Proceedings of the Annual International Conference of the IEEE Engineering in Medicine and Biology Society, EMBS*, 2015, vol. 2015–Novem, pp. 2423–2429.

[219] K. Suzuki, R. Kohlbrenner, M. L. Epstein, A. M. Obajuluwa, J. Xu, and M. Hori, "Computer-aided measurement of liver volumes in CT by means of geodesic active contour segmentation coupled with level-set algorithms," *Med. Phys.*, vol. 37, no. 5, pp. 2159–2166, 2010.

[220] A. Pradesh, "An Efficient Medical Image Segmentation Using Conventional OTSU Method," vol. 38, pp. 67–74, 2012.

[221] S. N. Goldberg, M. C. Stein, G. S. Gazelle, R. G. Sheiman, J. B. Kruskal, and M. E. Clouse, "Percutaneous radiofrequency tissue ablation: optimization of pulsed-radiofrequency technique to increase coagulation necrosis.," *J. Vasc. Interv. Radiol.*, vol. 10, no. 7, pp. 907–

16, Jul. 1999.

[222] S. N. Goldberg, G. S. Gazelle, E. F. Halpern, W. J. Rittman, P. R. Mueller, and D. I. Rosenthal, “Radiofrequency tissue ablation: importance of local temperature along the electrode tip exposure in determining lesion shape and size.,” *Acad. Radiol.*, vol. 3, no. 3, pp. 212–218, 1996.

[223] C. L. Brace, P. F. Laeseke, D. W. Van Der Weide, and F. T. Lee, “Microwave ablation with a triaxial antenna: Results in ex vivo Bovine Liver,” *IEEE Trans. Microw. Theory Tech.*, vol. 53, no. 1, pp. 215–220, 2005.

[224] M. K. Chung, B. M. Nacewicz, S. Wang, K. M. Dalton, S. Pollak, and R. J. Davidson, “Amygdala surface modeling with weighted spherical harmonics,” *Lect. Notes Comput. Sci. (including Subser. Lect. Notes Artif. Intell. Lect. Notes Bioinformatics)*, vol. 5128 LNCS, pp. 177–184, 2008.

[225] M. K. Chung, K. M. Dalton, L. Shen, A. C. Evans, and R. J. Davidson, “Weighted Fourier series representation and its application to quantifying the amount of gray matter,” *IEEE Trans. Med. Imaging*, vol. 26, no. 4, pp. 566–581, 2007.

[226] A. Hobolth, “The spherical deformation model.,” *Biostatistics*, vol. 4, no. 4, pp. 583–95, 2003.

[227] D. Goldberg-Zimring, A. Achiron, C. R. G. Guttmann, and H. Azhari, “Three-dimensional analysis of the geometry of individual multiple sclerosis lesions: detection of shape changes over time using spherical harmonics.,” *J. Magn. Reson. Imaging*, vol. 18, no. 3, pp. 291–301, 2003.

[228] A. Karampatzakis, S. Kühn, G. Tsanidis, E. Neufeld, T. Samaras, and N. Kuster, “Antenna design and tissue parameters considerations for an improved modelling of microwave

ablation in the liver," *Phys. Med. Biol.*, vol. 58, no. 10, pp. 3191–3206, May 2013.

[229] H. Xin-Wei, "Microwave ablation:Results in ex vivo and in vivo porcine livers with 2,450-MHzcooled-shaft antenna," Jan. 2012.